Control of Molecular Orientation in Organic Thin Films and Application in Organic Optoelectronic Devices

金, 俊演

https://doi.org/10.15017/1441192

2014

Doctoral Thesis

Control of Molecular Orientation in Organic Thin Films and Application in Organic Optoelectronic Devices

Jun Yun Kim

Department of Chemistry and Biochemistry
Graduate School of Engineering
Kyushu University

Contents

Chapter 1

General Introduction

1-1. Introduction

Vacuum deposited organic amorphous films play an important role in the enhancement of organic devices, such as organic light-emitting diodes (OLEDs),[1] organic field-effect transistors (OFETs),[2] and organic solar cells (OSCs).[3] Amorphous films having smooth interfaces are essential in the manufacture of practical pinhole-free multilayer films using simplified vacuum deposition techniques. Also, they offer the advantages of nanometerscale surface smoothness, readily controlled thickness, flexibility in the choice of underlying layers, and a simple high-purity fabrication process. Recently, it has been found that organic molecules in vacuum-deposited amorphous films are not always randomly oriented.[4-6] Yokoyama et al. have investigated the molecular orientation, its mechanism, and its effect on the electrical properties in many kinds of organic amorphous films. It has been found that linear-shaped molecules are horizontally oriented on a variety of substrates and molecules with longer molecular length possess a larger optical anisotropy.[5,6] Figure 1-1 shows a schematic illustration of condensed structures for organic semiconducting materials depending on molecular orientation. Compared with random orientation in amorphous films, horizontal orientation leads to larger intermolecular charge-transfer integrals[7] and smaller energetic and positional disorders,[8] which should in turn improve the charge-transport characteristics of the materials. Therefore, the correlation between the optoelectronic properties and the molecular orientation in organic vacuum deposited amorphous films is of highly importance to understand and improve the electrical properties of organic electronic devices.

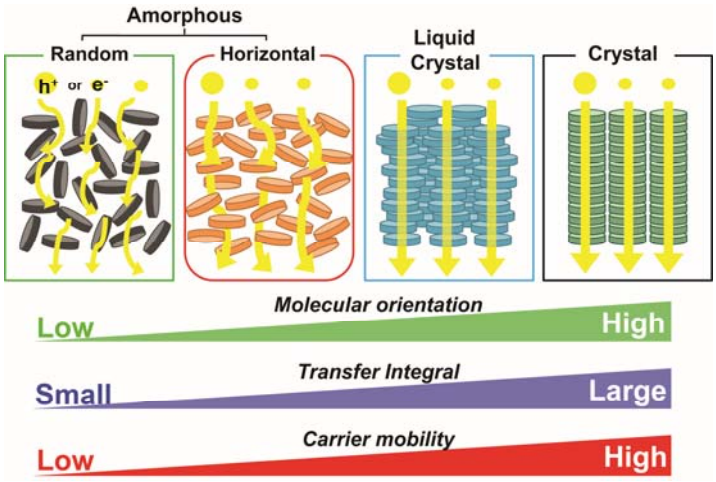

Figure 1-1. Schematic illustration of organic semiconducting materials with various molecular orientation.

1-2. Horizontal molecular orientation in amorphous films

For a long time, the molecular orientation in ‘‘amorphous’’ films has been thought to be completely random and isotropic because of difficulty detecting the molecular orientation in thin films. Since the amorphous materials used in organic devices have weak intermolecular interactions, which is the result of numerous molecular conformation structures and steric hindrance by bulky substituents, their films do not have a long-range ordered structure like crystalline films. This makes it difficult to investigate the molecular orientation and alignment by X-ray diffraction (XRD) measurement or other conventional methods. However, the optical anisotropy of films can be detected and analyzed to evaluate the molecular orientation in amorphous films. Anisotropic optical properties can be observed when there is a preferential orientation or alignment of molecules even in condensed organic system without long-range ordering. Variable angle spectroscopic ellipsometry (VASE) is one of the best methods to analyze the molecular orientation in amorphous organic films.[9,10] In addition, VASE provides a nondestructive approach to probe the optical properties of thin films.

1-2-1. Variable angle spectroscopic ellipsometry

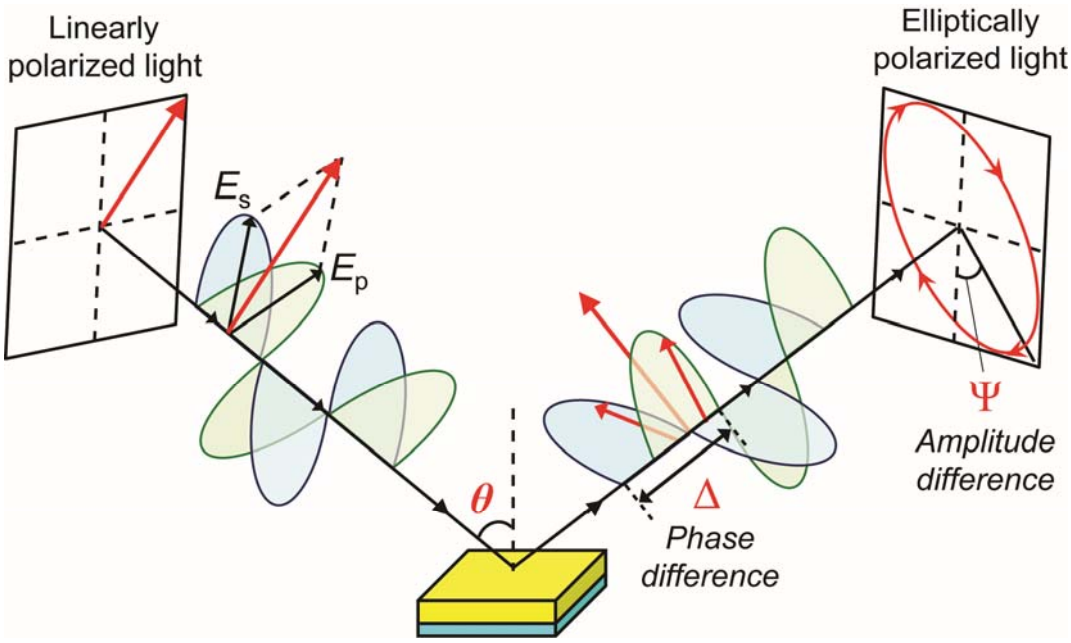

Figure 1-2. Schematic representation of variable angle spectroscopic ellipsometry.

Figure 1-2 illustrates the measurement principle of ellipsometry. In VASE, *p*- and *s*-polarized light waves are irradiated onto a sample at the Brewster angle, and the optical constants and

film thickness of the sample are determined from the change in the polarization state of reflected and transmitted by light. Linearly polarized light is incident with different incident angle of θ on to an organic film deposited on an Si substrate. The ellipsometry parameters, Ψ and Δ, which represent the ratio of the amplitudes of *s*- and *p*-polarized components of the incident light and the phase difference between them after reflection, respectively, are obtained for multiple incident angles and wavelengths. In this way, optical properties of the thin film are probed by the change in polarization state upon reflection.

In VASE analysis, thin films are initially treated as isotropic with the optical constants of real and imaginary parts (refractive index *n* and extinction coefficient *k*, respectively). The thickness of the films is first determined by assuming that *n* in the transparent region obeys the Cauchy equation and fitting the equation the experimental values of Ψ and Δ. With the determined thickness, *n* and *k* are then varied independently across the whole spectral region, including the transparent and absorptive regions, to fit the ellipsometric values at each wavelength (i.e., point-by-point fitting). However, in the case of anisotroic films, normal-incidence absorption spectra calculated using the thus obtained *k* show substantial mismatch with the ones measured by UV-Vis spectroscopy. In order to determine the optical constants of uniaxially anisotropic films, ellipsometric data obtained at several incident angles are necessary. The point-by-point fitting procedure described above does not require Kramers–Kronig consistency,[11] which is a required condition that *n* and *k* should necessarily satisfy. To meet this requirement, a Kramers–Kronig consistent model using a combination of one Cauchy background and several Gaussian oscillators for the ordinary and extraordinary optical constants can be constructed and thus used to fit the measured ellipsometric data.

This method of obtaining spectra under variable angles is called VASE and makes it possible to analyze the complicated optical properties of amorphous films. In particular, VASE is sensitive to the optical anisotropy in films because light propagating in an anisotropic film experiences different optical properties depending on the incident angle. The values of Ψ and Δ significantly depend on the anisotropy of the optical constants, and the optical anisotropies in films can be estimated from this dependence. Thus the anisotropies in *n* and *k* of films can be determined.

1-2-2. Relationship between the optical anisotropy and molecular orientation

As shown in Figure 1-3, when an anisotropic film has the same optical constants (n and k) in both horizontal directions (x and y) but a different property in the vertical direction (z), the film is said to have optical uniaxially anisotropy. In this case, the optical constants are different for horizontally and vertically polarized light (x=y≠z), yielding ordinary refractive indices and extinction coefficients (n_o and k_o) and extraordinary ones (n_e and k_e), respectively. This anisotropy in the optical constants of organic films is related to the anisotropy of the molecular orientation of the film. To make this relationship clear, the optical properties of the films must be correlated with the electronic properties of the molecules comprising the film.

The extinction coefficient of a film is directly related to the transition dipole moment of the molecule. The extinction coefficient is represented as

$$k = \left(\frac{\lambda}{4\pi}\right)\alpha$$

where α is the absorption coefficient of the film and λ is the wavelength of light. The extinction coefficient has the largest value in the direction of the transition dipole moment for the lowest energy excited state, which is almost parallel to the molecules. For example, the transition dipole moment of rod-like organic molecules is along the longest molecular axis, whereas a smaller transition dipole moment exists perpendicular to the longest molecular axis. Thus, the orientation of the transition dipole moments and, therefore, the molecular axes in the film can be interpreted through the anisotropy in the extinction coefficient of the film determined from the VASE measurement.

On the other hand, the refractive index of a film is not directly related to the anisotropy of the molecular orientation because each molecule itself has an anisotropy of molecular polarizability and the number density of the molecules in the film via the Lorentz–Lorenz equation.[12] In other words, films with higher molecular polarizability or number density possess a higher refractive index. The molecular polarizability is the relative tendency of a charge distribution, such as the electron cloud, to be distorted from its normal shape by an external electric field. Generally, the molecular polarizability in rod-like organic molecules has a larger value in the direction of the longest molecular axis than in the other directions (Fig. 1-3), because of the larger electron cloud within the area of molecule. Thus, the orientation of

molecules with an anisotropic shape can be deduced from the anisotropy in the refractive index of the film.

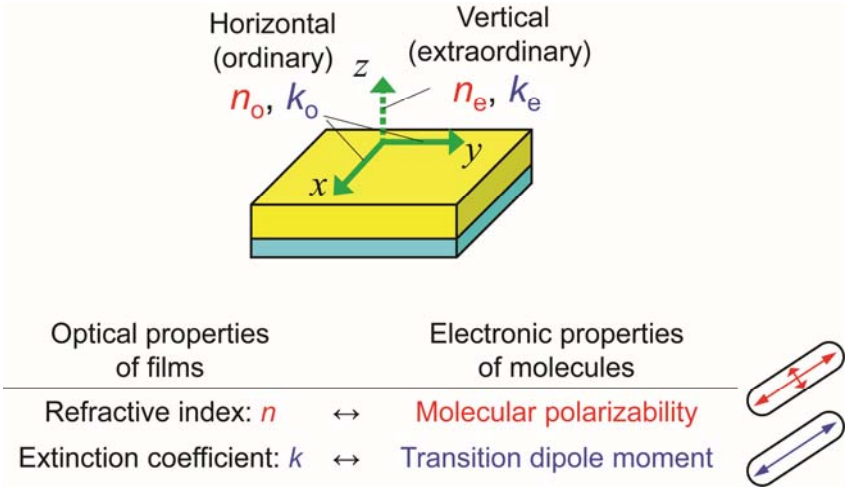

Figure 1-3. Optical anisotropy in vacuum-deposited amorphous organic films and relationship between the optical properties of films and electronic properties of molecules.

1-2-3. Structure of horizontal orientation in amorphous films

In the analysis of vacuum-deposited amorphous organic films by VASE, the in-plane rotation of the sample usually does not change the result of the analysis even when the film has large anisotropy. The van der Waals intermolecular interactions in amorphous materials are not as strong as the interactions in polycrystalline materials, leading to loose binding of molecules in the amorphous films with no ordered structure in plane (Fig. 1-4a). This molecular behavior in amorphous materials is quite different from that in polycrystalline materials, which often show a vertical orientation caused by strong intermolecular interactions. This means that the molecular orientation is random in the plane even when the properties of the molecular orientation are different between the horizontal and vertical directions, as shown in Figure 1-4b. After the formation of the horizontal orientation of the first molecular layer on the underlying layer, successive molecular orientation will occur due to the weak van der Waals interactions between the molecules without significant aggregation and crystallization. [13-15]

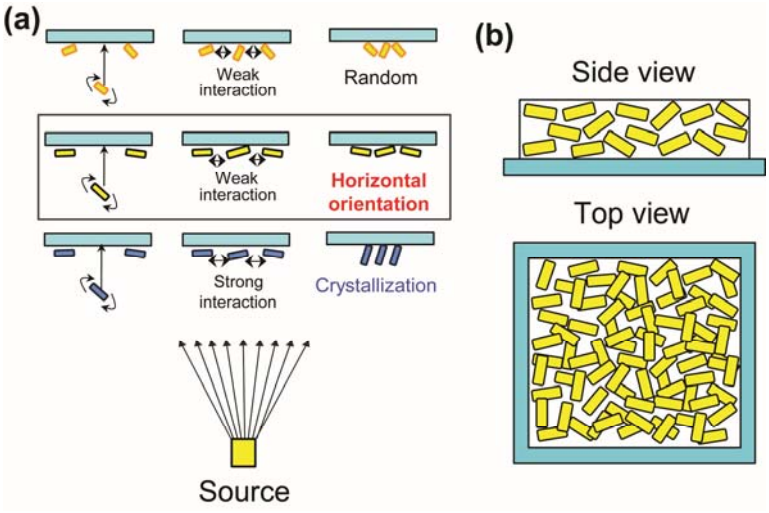

Figure 1-4. (a) Schematic illustration of crystalline aggregation of molecules having linear-shaped structure, horizontal orientation of molecules having linear-shaped structure. (b) Schematic of the horizontal orientation of linear-shaped molecules in amorphous films.

1-3. Organic light-emitting diodes (OLEDs)

Organic light-emitting diodes (OLEDs) have attracted much attention due to their potential application in flat panel displays. The basic OLED structure consists of a stack of thin organic layers between a transparent anode and a metallic cathode (Fig. 1-5). The thickness of each layer is in the range of several tens of nanometer. An OLED is a simple electronic device that converts electricity into light. Therefore, an OLED display needs no backlight units and can emit various colors without any color filters. Due to their self-emissive property and thin profiles, OLED displays have many advantages over other conventional display technologies: bright and high-contrast images, wide viewing angles, fast response, and lightweight. OLEDs can also be fabricated on plastic substrates that are thinner and lighter than glass. Therefore, OLEDs have the potential for realizing flexible displays. These features have led many to expect that OLEDs will form the basis for next-generation flat panel display devices.

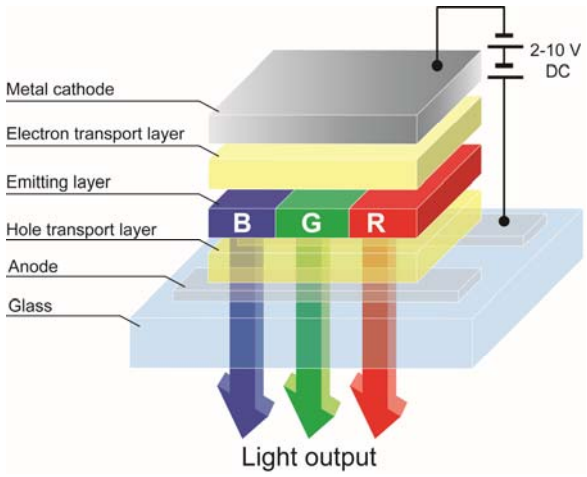

Figure 1-5. Schematic diagram of an OLED structure.

1-3-1. History of OLEDs

Electroluminescence (EL) from an organic material was first reported for anthracene single crystals-based devices in 1960s.[16,17] Blue emission was successfully observed form the devices, however, the conductivity σ of such materials was significantly, so low that the devices required very high driving voltages (V > 400 V). After this report, various attempts have been made to reduce the driving voltage of the devices by using vacuum deposition of small molecules and spin coating of polymers. In parallel, in the 1970s, the EL from polymer films was first observed by Roger Partridge at the National Physical Laboratory in the United Kingdom, and the first polymer LEDs (PLEDs), consisting of a film of poly(*N*-vinylcarbazole) (PVK) up to 2.2 μm

thick located between two charge injecting electrodes, was reported.[18,19] In particular, significant outcome was achieved in 1987 by Tang and Van Slyke.[20] They reported efficient and low-voltage OLED characteristics based on a *p-n* heterostructure using thin films of vapor-deposited small molecule organic materials. The device structure was simple vertical device, comprising thin layers of organic compounds, which were 1,1-bis-(4-bis(4-methylphenyl)-aminophenyl)-cyclohexane (TAPC) and tris(8-hydroxyquinolinato)aluminum (Alq_3), sandwiched between transparent indium-tin oxide (ITO) as an anode and a magnesium-silver alloy as a cathode (Fig. 1-6a). They successfully developed the first OLEDs with a luminance of over 1000 cd/m^2 at $V \sim 10$ V. In 1990, Burroughes et al. at the Cavendish Laboratory in Cambridge reported the first low-V PLEDs using 100-nm thick films of poly(*p*-phenylenevinylene) (PPV) (Fig. 1-6b).[21]

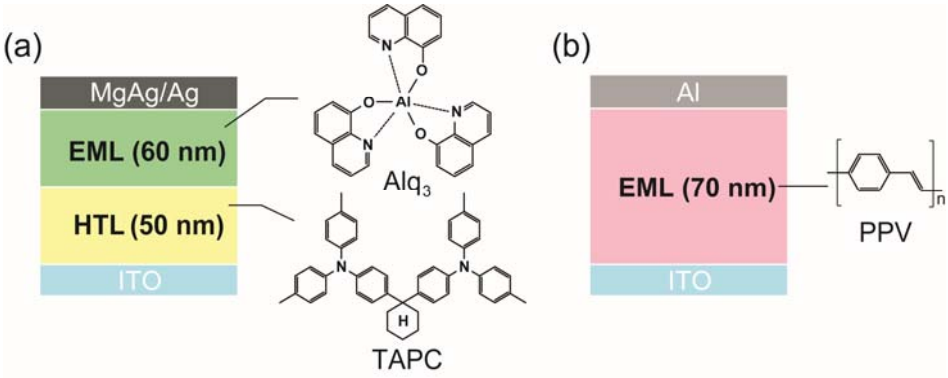

Figure 1-6. Schematic structure of OLEDs: (a) p-n heterostucture OLED composed of small molecular materials. (b) Single-layer OLED composed of conjugated polymer.

In the late 1990s and early 2000s, the groundbreaking work of S. R. Forrest, M. E. Thompson and their cowokers on phosphorescent OLEDs overcame the 25% limit on the internal quantum efficiency η_{int} of fluorescent OLEDs. It is well known that only the singlet excitons, which comprise 25% of the excited states, generate light in fluorescent organic materials. The other 75% of the excited states, which are triplet excitons, are almost entirely lost through nonradiative decay. However, the phosphorescent materials, which usually contain a heavy metal atom at the center of the molecule, for example iridium and platinum, generate light from both triplet and singlet excitons by the fast and efficient intersystem crossing (ISC), allowing η_{int} of such materials to reach nearly 100%. Thus phosphorescent OLEDs (PHOLEDs) with power efficiency over 100 lm/W have been realized so far.[22,23]

1-3-2. Structure of OLEDs

As mentioned, before the first small-molecule bilayer heterojunction OLEDs (SMOLEDs) contained two organic layers, the TAPC hole transport material and the Alq_3, emitting and electron transport material.[20] By inserting the separated hole transport layer, the quantum efficiency of the SMOLEDs was drastically improved, approximately ~100 fold, to ~ 1%, compared with thermally deposited anthracene electroluminescent devices.[20] After decades of fast developments in OLED technology, the structure of advanced OLEDs has become more and more complicated, especially in SMOLEDs fabricated by thermal vacuum evaporation. The multilayered OLEDs can consist of as many as seven different organic layers situated between two electrodes. The layers typically include a hole injection layer (HIL), hole transport layer (HTL), electron blocking layer (EBL), emitting layer (EML), hole blocking layer (HBL), electron transport layer (ETL), and electron injection layer (EIL) (Fig. 1-7). The organic materials are typically classified according to their functions. The HIL (EIL) is the buffer layer between the anode (cathode) and adjacent HTL (ETL), which reduces the hole (electron) injection barrier and facilitates charge injection.[24]

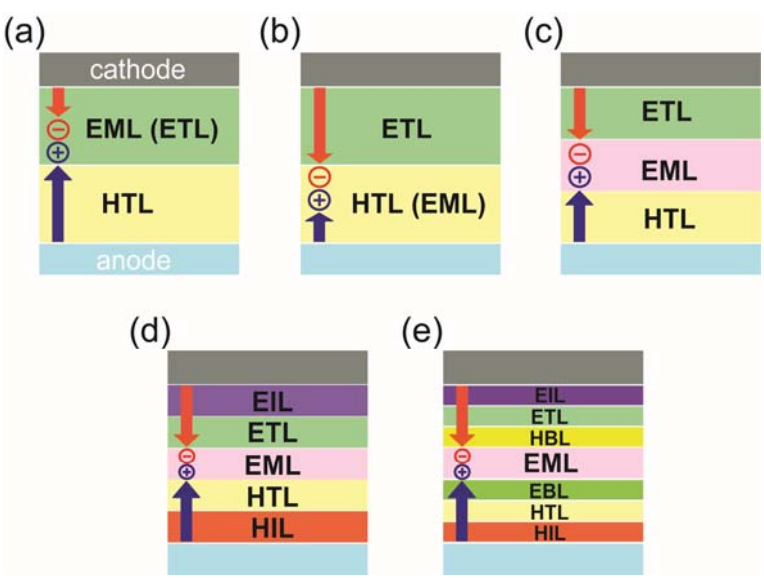

Figure 1-7. Schematic representation of single-heterostuctures (a, b) and multilayer structures (c, d, e) in OLEDs.

1-3-3. Operating principles of OLED

OLEDs are current-driven devices that utilize emissions form the electrically excited states of molecules. Figure 1-8 shows the basic principles of the emission mechanism in single-layer

OLED. When a voltage is applied between electrodes, charge are injected in the organic material, holes from the anode and electron form the cathode. The injected hole/electron carrier move inside the organic layer by hopping processes[25,26] and then holes and electrons recombine to generate electrically excited states of molecules. Finally, emissions from organic materials are obtained via transition from excited states to ground states. In case of multilayer, the HTL (ETL) rapidly transports the injected holes (electrons) to the recombination zone, which is located within the EML, so the hole transport materials (HTM) or electron transport materials (ETM) are designed to have high hole or electron mobility, μ_h and μ_e, respectively. Thus, the fundamental physical processes of OLED include carrier injection, transport, recombination, and radiative excition decay. Also, the color of the emission depends on the energy difference between the excited state and ground state of the emitter material.

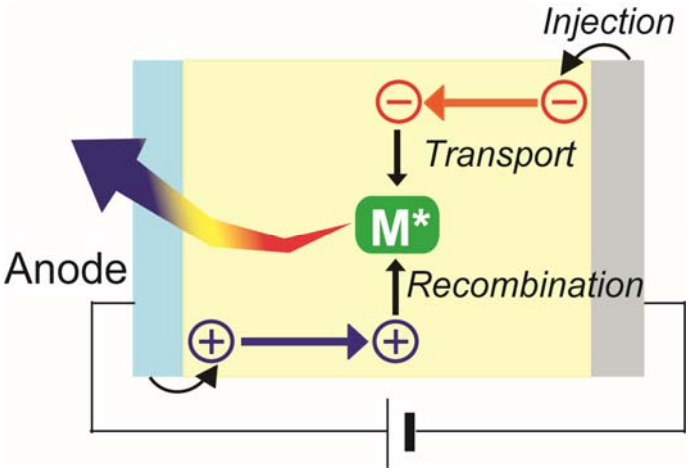

Figure 1-8. Schematic diagram of emission mechanism in OLED.

a. Carrier injection process

The process of carrier injection from electrodes to organic layer perform an important role in the optimization of the carrier balance in OLED. Figure 1-9 shows energy-level diagram of a multi-layer OLED. Shown are the highest occupied and lowest unoccupied molecular orbitals (HOMO and LUMO). Energy barriers for hole and electron injection (ΔE_h and ΔE_e) are also indicated. Under operational condition of layer, electron injection takes place from the Fermi level of the cathode into the LUMO level of the organic layer. At the same time, hole injection takes place from the Fermi level of the anode into the HOMO level of the organic layer. In the both process, energy barriers, ΔE_h and ΔE_e, have to be overcome. It is therefore important to reduce barrier heights for the carrier injections at the interface to realize low drive voltages,

which can lead to high OLED efficiency.

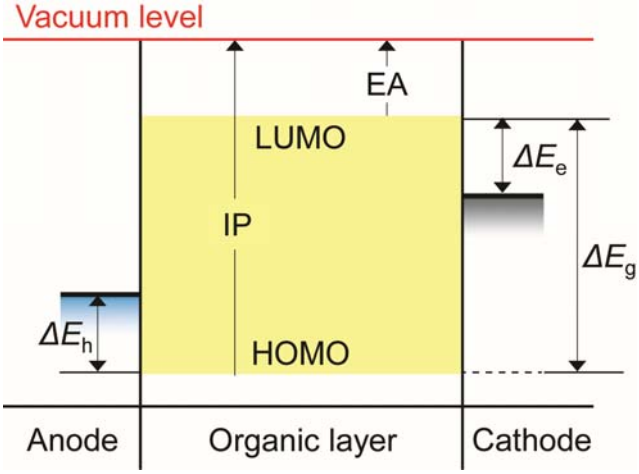

Figure 1-9. Energy-level diagram of Anode/Organic layer/Cathode interface.

Generally, indium-tin oxide (ITO) has been widely used as a transparent anode. For efficient hole injection from anode, ITO needs to be properly treated, such as ultra-violet ozone cleaning,[27] argon ion bombardment,[28] and oxygen plasma exposure.[29] In addition, hole injection layer with suitable energy level at organic/metal interface can be used to enhance hole injection efficiency. On the cathode side, a low injection barrier (ΔE_e) is requested for efficient electron injection. Low work function metals such as Ca and Mg are required but they are very sensitive to moisture and oxygen, and more stable cathodes have been introduced, such as Mg/Ag alloys or Al in combination with alkali metal compound.[30,31]

a-1. Fowler-Nordheim-Tunneling

An energy barrier with a height of Φ_{Bn} is formed if a metal and an insulator (the organic material in this case) are contacted and an electric field is applied. Thereby, the value of Φ_{Bn} results from the LUMO energy level relative to the Fermi energy of the contact. For high values of Φ_{Bn}, a triangular-shaped barrier is formed within the electric field in the absence of charge accumulation at the interface. Electrons can transfer from the metal into the organic layer by a tunneling process as illustrated in Figure 1-10a.

The tunneling distance and thus, the tunneling probability, strongly depends on the applied electric field (E). How the shape of the barrier changes with the field E is shown in the same figure qualitatively. The injected current density can be calculated from the tunneling probability according to by the following equation.[32,33]

$$J = \left(\frac{q^3 E^2 m_0}{8\pi h \Phi_{\mathrm{Bn}} m^*}\right) \exp\left(-\frac{8\pi\sqrt{2m^* \Phi_{\mathrm{Bn}}^3}}{3hqE}\right)$$

In this equation, m^* is the effective mass of the electrons in the organic material, h is the Planck constant and q the elementary charge. This process is called Fowler-Nordheim tunneling, in which further effects such as the image force and hot electron contribution to the current are neglected.

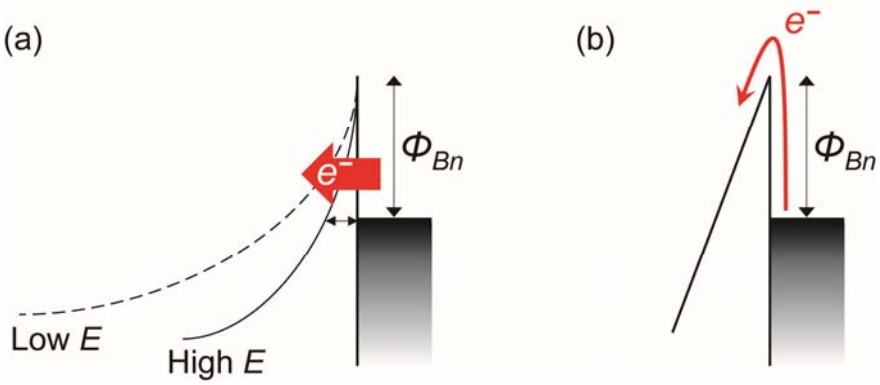

Figure 1-10. Energy barrier (a) Fowler-Nordheim-Tunneling through a triangular barrier Φ_{Bn} and (b) Schottky injection of organic/metal interface.

a-2. Thermionic Injection / Image Charge Potential

The image charge potential reduces the height of the triangular barrier which was described in the previous subsection.[32] An electron at a distance x from the metal can induce a positive (image) charge in the metal. The reduction of the barrier, the so-called Schottky-effect, δ is determined by

$$\delta = \sqrt{\frac{q^3 E}{4\pi\varepsilon\varepsilon_0}}$$

where ε is the relative dielectric constant and ε_0 the permittivity in vacuum. Due to this barrier reduction, the thermal energy can be sufficient to enable the transfer from the contact into the organic material (Fig. 1-10b). The current density which results from the thermal injection can be calculated by[34-36]

$$J = \frac{4\pi q k_{\mathrm{B}}^2 m^*}{h^3} T^2 \exp\left(-\frac{\Phi_{\mathrm{Bn}} - \sqrt{\delta}}{k_{\mathrm{B}} T}\right)$$

This model neglects tunneling through the barrier as well as inelastic backscattering.[37]

b. Carrier transport process

Injected charge carriers from the electrode into the organic layer are transported under an applied electric field towards the counter electrode. The carrier transport mechanism in disordered organic amorphous thin films are different from those for the bulk state of inorganic semiconductor materials. While inorganic semiconductors form energy band structures, valence band and conduction band, organic semiconductors are composed of molecules bound by weak intermolecular interactions such as van der Waals forces. Especially, the films of small-molecule organic semiconductors consist of units of small molecules, and each molecule has specific characteristics as a single molecule, such as geometric and electronic structures. Thus the dominant carrier transport mechanism is associated with charge hopping from one molecule to another. Hole and electron in organic semiconductors corresponds to the radical cation and radical anion of molecules. Holes are sequentially transferred from the radical cations to the neutral molecules through HOMO level for hole transport and electrons are sequentially transferred from the radical anions to the neutral molecules through LUMO level for electron transport.

Understanding of the carrier transport in disordered organic amorphous films is related to measure carrier mobility. Electronic transport is described by the (local) electric field-induced directional velocity component, $<v>$, of the mobile charge carriers (superimposed on their random thermal motion as a time and ensemble average of a fast sequence of acceleration and scattering events) which is associated with a current density j:[38]

$$j = e \cdot n \cdot < v >$$

where e is the electronic charge unit and n the local charge carrier density. The $<v>$ is proportional to the strength of the applied electrical field (F) and is expressed as follows:

$$< v > = \mu \cdot F$$

where, μ is the charge carrier mobility. It should be noted that μ is dependent on the electric field for organic disorder systems. The temperature and electric field dependence of carrier mobility in disordered amorphous films has been analyzed using formula based on such as Poole-Frenkel model[25] and Gaussian disorder model.[26] The electrical dependence of μ can be described by:

$$\mu = \mu_0 \exp\left(\beta\sqrt{F}\right)$$

where μ_o is the zero mobility and is the slope of the filed dependence of carrier mobility. For organic amorphous films, carriers are trapped in disordered structures and localized states. In the Poole-Frenkel model, a carrier mobility can be described as electric filed and temperature assisted detrapping process of a carrier from coulomb potential of a charged trap. The mobility is then given by

$$\mu(F,T) = \mu_0 \exp\left(-\frac{\Delta E - \beta\sqrt{F}}{k_B T_{\text{eff}}}\right), \qquad \frac{1}{T_{\text{eff}}} = \frac{1}{T} - \frac{1}{T_0}$$

where, ΔE, β, k_B, and T_0 are the activation energy in the absence of electric filed, the Poole-Frankel coefficient, the Boltzmann constant, and the temperature at which the extrapolated data of Arrhenius plots for various electric fields intersect with one another, respectively. The experimental results obtained for many organic disorder systems have been reported to fit this empirical equation well.

The Gaussian disorder model is based on the concept of carrier hopping in disordered amorphous films whose transport states have an energy distribution that can be described by a Gaussian. The Gaussian disorder model had been quite successful in explaining carrier transport in a wide variety of amorphous films.[39,40] In the hopping process, the carriers are subject to built-in energetic disorder (σ), and positional disorder (Σ). The σ can be understood as the width of the Gaussian distribution of energy states while the Σ can be understood as the spatial disorder arising from structural or chemical defects.[41,42] The essence of Gaussian disorder model can be embodied in the following equation for the carrier mobility,

$$\mu = \mu_0 \exp\left[-\left(\frac{2\sigma}{3k_B T}\right)^2\right] \exp\left\{C[\sigma^2 - \Sigma^2]\sqrt{F}\right\} \ (\Sigma > 1.5)$$

$$\mu = \mu_0 \exp\left[-\left(\frac{2\sigma}{3k_B T}\right)^2\right] \exp\left\{C[\sigma^2 - 2.25]\sqrt{F}\right\} \ (\Sigma < 1.5)$$

where μ_0 is the zero mobility, C is an empirical constant (3×10^{-4} $cm^{1/2}\cdot V^{-1/2}$) which reflects the hopping distance that a charge carrier has to overcome to be transferred from one site to another. The energetic disorder arises from the distribution of conjugation length, while the positional disorder arises from the fluctuations of intermolecular distances or morphological variations. Therefore, carrier mobility in organic disordered amorphous films is markedly dependent on the molecular structures and morphology.

c. Recombination process

c-1. Fluorescence emitter

Excitons formed by the recombination of the hole-electron pairs may either be in a singlet or triplet state, depending on how the spins of two particles combine. Statistically, 25% of the excitons are singlet excitons and 75% of them are triplet excitons.[23,43] Radiative decay of the excitons results in the production of light through spontaneous emission. In OLEDs using fluorescent organic emitters, there is almost no light generated from the decay of the triplet state, which decays through nonradiative channels. Hence, this places a theoretical limit on η_{int} (the ratio of the total number of photons generated within the OLEDs to the number of electrons injected) of 25% (Fig. 1-11a).[23,24]

c-2. Phosphorescence emitter

The phosphorescent organic emitters usually contain a heavy metal atom at the center of the molecule, for example platinum[22] and iridium,[24] of which the green emitting complex tris[2-(*p*-tolyl)pyridine]iridium(III) ($Ir(mppy)_3$) is one of the representative examples.[44] The large spin-orbit interaction experienced by the molecule due to this heavy metal atom facilitates ISC. This reduces the lifetime of the triplet state, so phosphorescence is readily observed.[23,45] The phosphorescent OLEDs generate light from both triplet and singlet excitons, allowing η_{int} of such devices to reach nearly 100% (Fig. 1-11b).[23]

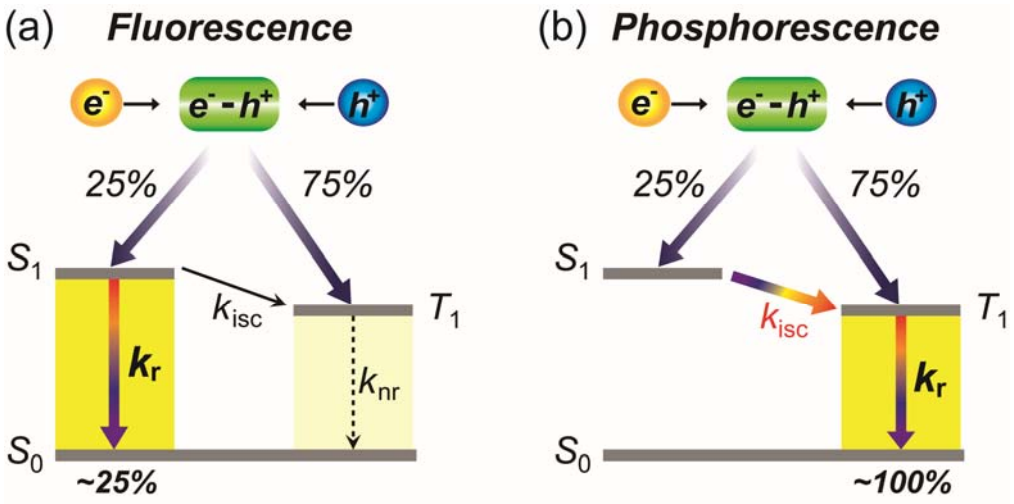

Figure 1-11. Emission mechanism of typical fluorescent (a) and phosphorescent (b) materials.

d. OLED efficiency

The internal and external quantum efficiencies are important factors to describe the performance of OLED. The internal quantum efficiency η_{int} is defined as the fraction of generated photons n_{ph} to injected electron hole pairs n_{eh}.[46]

$$\eta_{\mathrm{int}} = \frac{n_{\mathrm{ph}}}{n_{\mathrm{eh}}}$$

How many charge carriers are converted to photons depends on several factors and is given by the product of the probabilities of the different processes according to[47]

$$\eta_{\mathrm{int}} = \gamma \cdot \eta_r \cdot \eta_{\mathrm{PL}}$$

where, η_{PL} is the quantum efficiency of fluorescence which represents the number of excitons which recombine radiatively. η_r is the efficiency of formation of an emissive exciton from an electron hole pair, which is 25% only for fluorescent emitters and can be up to 100% for phosphorescent emitters according to spin statistics.[48] The γ denotes the carrier balance factor which describes the numerical ratio of injected electrons and holes and therefore reflects the charge carrier balance in the device. The carrier balance factor is unity ($\gamma = 1$) if all injected holes and electrons recombine in the device. If an imbalance of charge carriers exists in the organic layers, the majority type of charge carrier can reach the opposite electrode and eventually reduce the efficiency of the OLED.

The external quantum efficiency (EQE) is defined as the fraction of photons escaping the OLED to the number of injected charge carrier pairs. In other words, it differs from the internal quantum efficiency by taking the outcoupling efficiency η_{out} into account and thus is given by

$$\eta_{\mathrm{ext}} = \eta_{\mathrm{int}} \cdot \eta_{\mathrm{out}}$$

The typical outcoupling efficiency of OLED is about 20%. 80% of the generated photons are absorbed either in the organic layers, the electrode materials or the glass substrate. In addition to this, the spectrum and the outcoupling of an OLED is influenced by micro cavity effects. An optical micro cavity is a structure formed by reflecting faces on the two sides of a spacer layer. In the case of OLED, the spacer layer is formed by the organic materials, while the metal cathode as well as the transparent conductive oxide (TCO) on glass are the reflecting faces. The glass/ITO interface is not a mirror, of course, but partially reflects the generated light. More crucial is the metal cathode and its distance to the emissive layer.

Conventional bottom-emitting OLEDs, which have light out through the bottom substrate, consist of thin organic films (n_{org}, 1.6-1.8) sandwiched in between an ITO (n_{ITO} ~1.9) coated glass substrate (n_{sub} ~1.5) and a highly reflective cathode. According to classical ray optics, the emitted light suffers total internal reflection at the substrate/air and organic-ITO/substrate interfaces due to different refractive index of constituent layers (Fig. 1-12). As the result, the emitted light can be roughly classified into three modes as escaped, substrate, and ITO-organic modes. Based on the assumptions of homogeneous, isotropic emission and a perfectly refractive cathode, the fraction of light out-coupled through the surface can be estimated in a first approximation using classical ray optics, following $\eta_{out} = 1 - (1 - 1/n_{org}^2)^{1/2}$. With the refractive index of organic films around 1.7, the calculation indicates that no more than 20% of the light generated inside can be extracted from the device surface.[49,50]

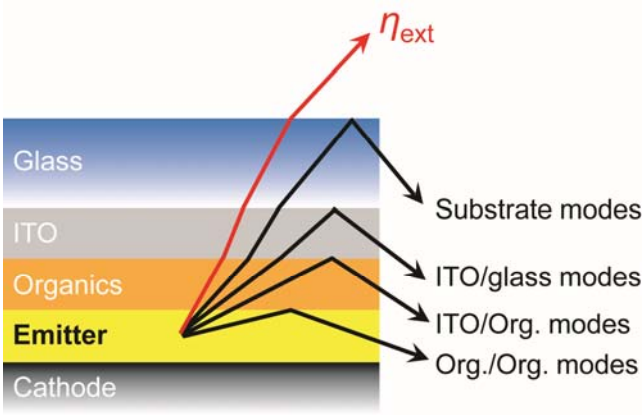

Figure 1-12. Different radiative modes in OLEDs. External modes available for the face detection (η_{ext}) constitutes only a fraction of light generated in the EML, the remainder being lost due to various wave guide modes.

1-4. Outline of this thesis

This thesis focuses mainly on the design and synthesis of new horizontally oriented amorphous materials for high performance OLEDs, with high carrier transport ability and efficient emission by considering relationship between molecular orientation and electrical properties.

In Chapter 2, two-dimensional disk-like molecules, diaminobenzene derivatives are designed and synthesized to induce horizontal molecular orientation on substrates. OLEDs based on these materials as a hole transport layer (HTL) are expected to have enhanced electrical performance because the molecular orientation affects the overlap of the wave functions at the interface.

In Chapter 3, the synthesis and design of derivatives utilizing *N,N,N′,N′*-tetraphenyl-*p*-phenylenediamine (PDA) or triphenylamine (TPA) core with triphenylethene (TPE) units are discussed. This TPE units are chosen because they can offer unique aggregation induced emission (AIE) characteristics. The characterization of these derivatives with both horizontal orientation and AIE phenomenon are investigated. Using films with different molecular orientation of the same molecules, the direct comparison of both the carrier mobilities in the films and the outcoupling efficiency in OLEDs, and discussion on the effect of molecular orientation are conducted.

Chapter 4 reports on polymorphism in 9,9-diarylfluorene-based organic semiconductors. The effects of rich phase behavior on the charge transport and photoluminescence properties of these semiconductors are investigated. Polymorph control is a rational way to tailor the optoelectronic functions of their films.

1-5. References

[1] C. W. Tang, S. A. Vanslyke, *Appl. Phys. Lett*., **1987**, 51, 913.

[2] G. Horowitz, *Adv. Mater*., **1998**, 10, 365.

[3] M. C. Scharber, D. Mühlbacher, M. Koppe, C. Waldauf, A. J. Heerger, C. J. Brabec, *Adv. Mater.,* **2006**, 18, 789.

[4] H. W. Lin, C. L. Lin, H. H. Chang, Y. T. Lin, C. C. Wu, Y. M. Chen, R. T. Chen, Y. Y. Chien, K. T. Wong, *J. Appl. Phys.*, **2004**, 95, 881.

[5] D. Yokoyama, A. Sakaguchi, M. Suzuki, C. Adachi*, Org. Electron.*, **2009**, 10, 127.

[6] D. Yokoyama, A. Sakaguchi, M. Suzuki, C. Adachi, *Appl. Phys. Lett.*, **2008**, 93, 173 302.

[7] R. A. Marcus, *J. Chem. Phys*., **1956**, 24, 966.

[8] H. Bässler, Phys. *Status Solidi B*, **1993**, 175, 15.

[9] J. A. Woollam, B. Johs, C. M. Herzinger, J. Hilfiker, R. Synowicki, C. L. Bungay, *Proc. SPIE*, **1999**, CR72, 3.

[10] B. Johs, J. A. Woollam, C. M. Herzinger, J. N. Hilfiker, R. Synowicki, C. L. Bungay, *Proc. SPIE*, **1999**, CR72, 29.

[11] H. Fujiwara, *Spectroscopic Ellipsometry: Principles and Applications*, Wiley, New York, **2007**.

[12] M. Born, E. Wolf, *Principles of Optics*, Cambridge Univ. Press, England, 7th edn, **1999**.

[13] B. Servet, S. Ries, M. Trotel, P. Alnot, G. Horowitz, F. Garnier, *Adv. Mater.*, **1993**, 5, 461.

[14] S. E. Fritz, S. M. Martin, C. D. Frisbie, M. D. Ward, M. F. Toney, *J. Am. Chem. Soc.*, **2004**, 126, 4084.

[15] H. Peisert, T. Schwieger, J. M. Auerhammer, M. Knupfer, M. S. Golden, J. Fink, P. R. Bressler, M. Mast, *J. Appl. Phys.*, **2001**, 90, 466.

[16] H. Kallmann, M. Pope, *J. Chem. Phys.*, **1960**, 32, 300.

[17] H. Kallmann, M. Pope, *Nature*, **1960**, 186, 4718.

[18] P. Mark, W. Helfrich, *J. Appl. Phys.*, **1962**, 33, 205.

[19] M. Pope, H. P. Kallmann, P. Magnante, *J. Chem. Phys.*, **1963**, 38, 2042.

[20] C. W. Tang, S. A. Vanslyke, *Appl. Phys. Lett.*, **1987**, 51, 913.

[21] J. H. Burroughes, D. D. C. Bradley, A. R. Brown, R. N. Marks, K. MacKay, R. H. Friend, P. L. Burns, A. B. Holmes, *Nature*, **1990**, 347, 539.

[22] M. A. Baldo, D. F. O'Brien, Y. You, A. Shoustikov, S. Sibley, M. E. Thompson, S. R. Forrest, *Nature*, **1998**, 395, 151.

[23] M. A. Baldo, S. Lamansky, P. E. Burrows, M. E. Thompson, S. R. Forrest, *Appl. Phys. Lett.*, **1999**, 75, 4.

[24] C. Adachi, M. A. Baldo, M. E. Thompson, S. R. Forrest, *J. Appl. Phys.*, **2001**, 90, 5048.

[25] J. Frenkel, *J. Chem. Phys.*, **1965**, 43, 2654.

[26] H. Bässler, *Phys. Status Solidi B*, **1981**, 107, 9

[27] C. C. Wu, C. I. Wu, J. C. Sturm, A. Kahn, *Appl. Phys. Lett.*, **1997**, 70, 1348.

[28] J. S. Kim, M. Granström, R. H. Friend, N. Johansson, W. R. Salaneck, R. Daik, W. J. Feast, F. Cacialli, *J. Appl. Phys.*, **1998**, 84, 6859.

[29] M. G. Mason, L. S. Hung, C. W. Tang, S. T. Lee, K. W. Wong, M. Wang, *J. Appl. Phys.*, **1999**, 86, 1688.

[30] J. Kido, T. Matsumoto, *Appl. Phys. Lett.*, **1998**, 73, 2866.

[31] T. Oyamada, C. Maeda, H. Sasabe, C. Adachi, *Jpn. J. Appl. Phys.*, **2003**, 42, L1535.

[32] V. I. Arkhipov, E. V. Emelianov, Y. H. Tak, H. Bässler, *J. Appl. Phys.*, **1998**, 84, 848.

[33] S. Barth, U. Wolf, H. Bässler, H. Riel, H. Vestweber, P.F. Seidler, W. Riess, *Phys. Rev. B*, **1999**, 60, 8791.

[34] A. J. Campbell, D.D.C. Bradley, D.G. Lidzey, *J. Appl. Phys.*, **1997**, 82, 6326.

[35] U. Wolf, V.I. Arkhipov, H. Bässler, *Phys. Rev. B*, **1999**, 59, 507.

[36] M. Matsumura, T. Akai, M. Saito, T. Kimura, *J. Appl. Phys.*, **1996**, 79, 264.

[37] J. Godlewski, J. Kalinowski, *Jpn. J. Appl. Phys.*, **1989**, 28, 24.

[38] N. Karl, *Synthetic Metals*, **2003**, 649, 133.

[39] M. Stolka, J. F. Yanus, D. M. Pai, *J. Phys. Chem.*, **1984**, 88, 4707

[40] E, Lebedev, T. Dittrich, V. Petrova-Koch, S. Karg, W. Brutting, *Appl. Phys. Lett.*, **1997**, 71, 2686.

[41] A. J. Campbell, D. C. C. Bradley, D. G. Lidzey, *J. Appl. Phys.*, **1997**, 82, 6326.

[42] T. Nagase. H. Naito, *J. Appl. Phys.*, **2000**, 88, 252.

[43] A. R. Brown, K. Pichler, N. C. Greenham, D. D. C. Bradley, R. H. Friend, A. B. Holmes, *Chem. Phys. Lett.*, **1993**, 210, 61.

[44] X. Yang, D. Neher, D. Hertel, T. Daubler, *Adv. Mater.*, **2004**, 16, 161.

[45] D. F. O'Brien, M. A. Baldo, M. E. Thompson, S. R. Forrest, *Appl. Phys. Lett.*, **1999**, 74, 442.

[46] A. Misra, P. Kumar, M. N. Kamalasanan, S. Chandra, *Semicond. Sci. Technol.*, **2006**, 21, 35.

[47] T. Tsutsui, *Organic multilayer-dye electroluminescent diodes - is there any difference with polymer LED?*, Springer, **1993**, 246, 123.

[48] H. Yersin, *Highly efficient OLEDs with phosphorescent materials*, Wiley-VCH, **2007.**

[49] J. S. Kim, P. K. H. Ho, N. C. Greenham, R. H. Friend, *J. Appl. Phys.*, **2000**, 88, 1073.

[50] L. H. Smith, J. A. E. Wasey, W. L. Barnes, *Appl. Phys. Lett.*, **2004**, 84, 2986.

Chapter 2

Horizontal Orientation of Disk-Like Hole Transport Molecules and Their Application to Organic Light-Emitting Diodes Requiring a Lower Driving Voltage

2-1. Introduction

A wide variety of improvements in organic light-emitting diodes (OLEDs) have been made using novel materials and device structures to achieve superior external electroluminescence efficiency (η_{EL}) at lower driving voltages.[1-5] Since OLEDs usually require formation of a very thin (typically 100-200 nm) film, organic layers with amorphous morphologies that provide pin-hole free thin films have been widely used. However, amorphous films are not the best morphology for maximizing electrical and optical characteristics. Although one of the best film morphologies for improved OLED performance is a polycrystalline texture, it always results in failure, such as shorting between the cathode and anode because of the presence of discontinuities like grain boundaries. Thus, to obtain a practical solution, advanced control of amorphous morphologies (for example via molecular orientation) is a potentially important tool to enhance OLED characteristics. Although one might assume that molecules in amorphous layers would have completely random orientations, our recent studies using wide-range variable angle spectroscopic ellipsometry (VASE)[6] showed that molecules with a long rod-like structure such as 4,4'-bis[(*N*-carbazole)styryl]biphenyl (BSB-Cz),[7] and a planar structure such as 1,3-bis[2-(2,2'-bipyridin-6-yl)-1,3,4-oxadiazo-5-yl]benzene (Bpy-OXD)[8,9] and *N,N,N′,N′*-tetrakis(biphenyl-4-yl)benzidine (TPD15) show horizontal orientation regardless of the underlying layers.[10–12] In fact, the higher carrier mobilities in these molecules are attributed to the enhancement of π-π interactions between adjacent molecules relative to the system where the molecules have completely random orientation.[12,13] In this study, novel disk-like molecules: N^1, N^1, N^4, N^4-tetra(biphenyl-4-yl)benzene-1,4-diamine (**B-DDP**)[14]; N^1,N^1,N^4,N^4-tetrakis(4-(thiophen-2-yl)phenyl)benzene-1,4-diamine (**T-DDP**); and N^1,N^1,N^4,N^4-tetrakis(4-(benzo[*b*]thiophen-2-yl)phenyl)benzene-1,4-diamine (**BT-DDP**) were proposed. The two-dimensional planar structures of these molecules should lead to enhanced horizontal orientation, enabling more intense π-π interaction between adjacent molecules, and thus leading to improved OLED characteristics. In particular, the relationship between driving voltage and molecular orientation of these molecules is investigated. It can be found that the horizontal molecular orientation at anode interfaces results in significant decrease in hole injection barriers.

2-2. Design and synthesis

Scheme 2-1 shows the synthetic route for DDP derivatives. The diaminobenzene core with its starburst shape and excellent electron donating ability has been widely used as a hole-transporting molecule in OLEDs.[15] Although most of benzidine backbones are twisted between the two central benzene rings, the DDP cores provides direct conjugation between the two amines. Therefore, the diaminobenzene cores provide a shallower HOMO level compared with that of benzidine cores.[16] This is related to the small conformational change accompanied by bond rotation.[17,18] With the increase in π-conjugation associated with the introduction of substituents into the diaminobenzene core, to give DDP derivatives, it can be expected molecular orientation due to the planar structure. In this study, **B-DDP**, **T-DDP** and **BT-DDP** having phenyl, thiophene, and benzothiophene substituents around a diaminobenzene core. DDP were synthesized derivatives were synthesized based on the Suzuki coupling reaction of *N*^{1},*N*^{1},*N*^{4},*N*^{4}-tetrakis(4-bromophenyl)benzene-1,4-diamine (DDP) with the corresponding boronic acids in the presence of tetrakis(triphenylphosphine)palladium(0) in tetrahydrofuran (THF). All materials were purified thoroughly by recrystallization from THF solution and vacuum train sublimation, and were identified by ^{1}H NMR spectroscopy and elemental analysis.

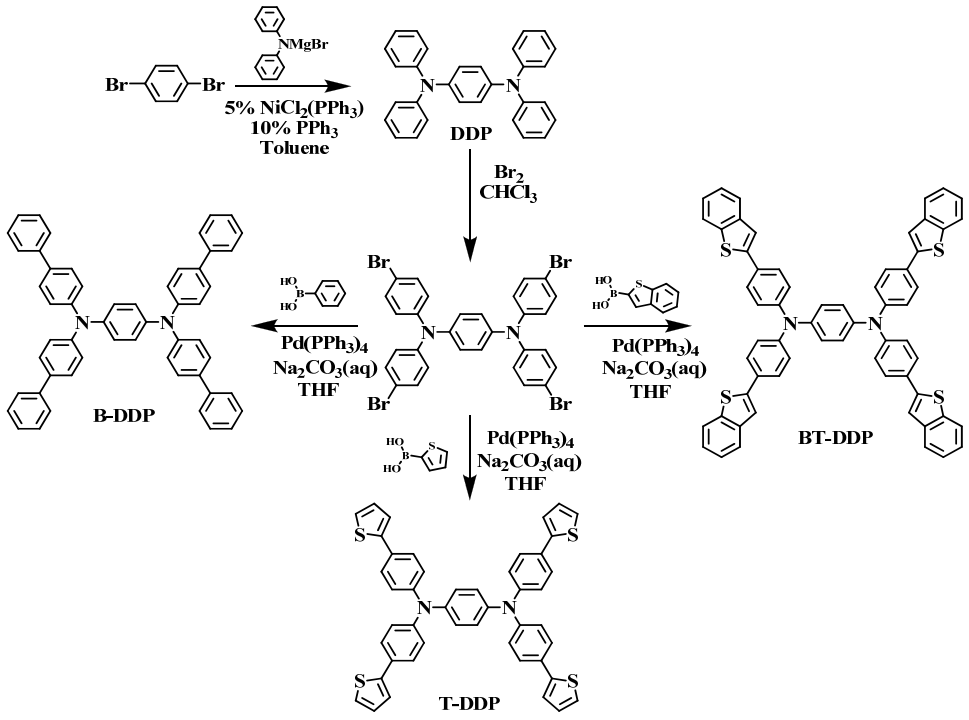

Scheme 2-1. Synthetic route of DDP derivatives.

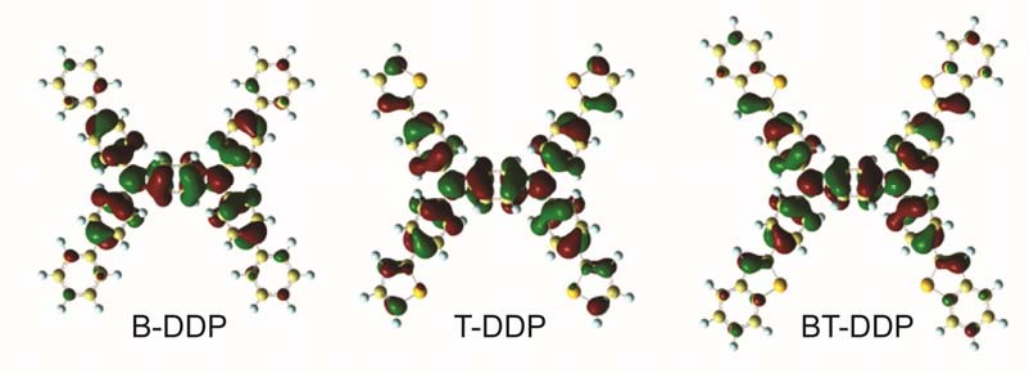

Figure 2-1. Stable conformers of **B-DDP, T-DDP** and **BT-DDP** and their HOMOs calculated by molecular mechanics and B3LYP/6-31G(d).

2-3. Experimental

2-3-1. Measurement of optical properties

The highest occupied molecular orbital (HOMO) levels of DDP derivatives were estimated from their ionization energies (I_p) in the film states. I_p values were measured by ultraviolet photoelectron spectroscopy (AC-2, Riken-keiki Co.). The lowest unoccupied molecular orbital levels were estimated by subtracting the optical energy gaps (E_g) from the HOMO energies. The E_g values were determined by the onset energies of absorption spectra of the films. The films (50 nm-thick) were formed on quartz substrates by thermal vacuum deposition. UV spectra were recorded with a spectrometer (UV-2550, Shimadzu).

2-3-2. Variable angle spectroscopic ellipsometry (VASE)

Thin films for ellipsometry measurement were deposited on silicon (100) substrates, which were pre-cleaned by detergent and organic solvents. All organic films were thermally evaporated onto the substrates under a vacuum of $<3\times10^{-4}$ Pa with an evaporation rate of ~0.1 nm/s. The thicknesses of all the samples were 100 nm. VASE was performed using a fast spectroscopic ellipsometer (M-2000U, J. A. Woollam Co. Inc.). Seven different angles of the incident light from 45° to 75° with steps of 5° were used. At each angle, the experimental ellipsometric parameters Ψ and Δ were obtained simultaneously in 1.6-nm step from 245 to 1000 nm. The VASE data was analyzed using a ‘‘WVASE32’’ (J. A. Woollam Co., Inc) software.

2-3-3. OLED device fabrication and measurements

Organic layers and metal electrodes were deposited by high-vacuum ($\sim1.0\times10^{-4}$ Pa) thermal evaporation onto ITO-coated glass substrates, which had been degreased with solvents and cleaned using detergent and organic solvents and subjected to a UV-ozone chamber for 15 min. Standard OLEDs are composed of a 50 nm-thick hole transport layer (HTL), and a 50 nm-thick Alq_3 layer as an emitting layer. To clarify injection and transport mechanism of DDP derivatives, OLEDs having x-nm-thick DDP derivative/ 50-x nm-thick α-NPD/ 50 nm-thick Alq_3 layer were examined. In all devices, a cathode (MgAg layer with the weight ratio of 10:1) and a 10-nm-thick Ag capping layer were deposited through a 1 mm-diameter opening in a shadow mask. The current density (J)-voltage (V)-external EL quantum efficiency characteristics of the

OLEDs were measured using a semiconductor parameter analyzer (Agilent E5273A) and an optical powermeter (Newport 1930-C).

2-3-4. Materials and syntheses

***N*^{1},*N*^{1},*N*^{4},*N*^{4}-tetraphenylbenzene-1,4-diamine (1).** Diphenylamine (2.97 g, 18 mmol) was dissolved in dry THF (30 mL) at room temperature in a 100 mL flask fitted with a dropping funnel and argon inlet. Ethyl magnesium bromide (2.42 g, 18 mmol) was then added dropwise slowly over 1 h and the mixture was stirred for 4 h. The solvent was removed under vacuum after deprotonation of diphenylamine, and then dry toluene, $NiCl_2$(dppp) (2.09 g, 0.4mmol), triphenylphosphine (2.02 g, 0.8 mmol) and 1,4-dibromobenzene (1.80 g, 7.6 mmol) were added. The mixture was stirred and refluxed overnight at 80 °C, and was then poured into a solution of HCl (20 mL) and water (100 mL) and stirred for 5 h. The solution was neutralized with sodium carbonate, followed by extraction with dichloromethane. The organic phase was washed with water and dried over anhydrous Na_2SO_4 before the solvent was evaporated. After removing the solvent, the crude product was recrystallized in acetone and THF to give a white solid *N*^{1},*N*^{1},*N*^{4},*N*^{4}-tetraphenylbenzene-1,4-diamine (1.88 g, 59.8% yield). ^{1}H NMR (400 MHz, $CDCl_3$): δ 7.24 (dd, 8H, J = 8.8, 7.3 Hz), 7.10 (d, 8H, J = 8.8 Hz), 6.98 (t, 4H, J = 7.3 Hz), 6.98 (s, 4H). MS (MALDI-TOF): *m/z* 411.98 [M+H]$^+$. Anal. calcd (%) for $C_{30}H_{24}N_2$: C 87.35, H 5.86, N 6.79; found: C 87.11, H 5.93, N 6.80.

***N*^{1},*N*^{1},*N*^{4},*N*^{4}-tetrakis(4-bromophenyl)benzene-1,4-diamine (2).** A solution of 3,4-ethylenedioxythiophene (6.00 g, 14 mmol) in dimethylformamide (DMF; 50 mL) was cooled to 0 °C, blanketed by argon. A solution of *N*-bromo succinimide (11.4 g, 64 mmol) in DMF (50 mL) was added dropwise and the temperature was maintained below 10 °C. After addition, the reaction mixture was brought to room temperature and stirred for another hour. The reaction mixture was then poured into ice water (1 L) and filtered, and the residue was washed with water. After crystallization from ethanol, pure product was obtained as a white crystalline material (9.7 g, 92% yield). ^{1}H NMR (400 MHz, $CDCl_3$): δ 7.35 (d, 8H, J = 8.8 Hz), 6.94 (d, 8H, J = 8.8 Hz), 6.95 (s, 4H). MS (MALDI-TOF): *m/z* 723.72 [M+H]$^+$. Anal. calcd (%) for $C_{30}H_{20}Br_4N_2$: C 49.49, H 2.77, N 3.85; found: C 49.67, H 2.70, N 3.79.

Synthesis of B-DDP. Based on the Suzuki-coupling reaction, a mixture of phenyl boronic

acid (5.00 g, 41 mmol), tetrakis(triphenylphosphine)palladium (0.47 g, 0.4 mmol), sodium carbonate (2 M, 20 mL), compound **2** (5.00 g, 6.9 mmol), and THF (50 mL) was added into a 100 mL flask and refluxed for 48 h under argon. The reaction mixture was then poured into ice water and extracted twice with CH_2Cl_2. The combined organic fractions were washed with water, dried (Na_2SO_4), filtered, and concentrated. The residue was purified by recrystallization from toluene to give pure B-DDP (3.30 g, 66% yield). m.p. 314 °C. ^{1}H NMR (400 MHz, DMSO-d_6): δ 7.65 (d, 16H, J = 8.8 Hz), 7.45 (t, 8H, J = 5.1 Hz), 7.33 (t, 4H, J = 7.3 Hz), 7.17 (d, 8H, J = 8.4 Hz), 7.14 (s, 4H). MS (MALDI-TOF): *m/z* 716.21 $[M+H]^+$. Anal. calcd (%) for $C_{54}H_{40}N_2$: C 90.47, H 5.62, N 3.91; found: C 90.47, H 5.62, N 4.00.

Synthesis of T-DDP. 2-Thiophene boronic acid (5.30 g, 41 mmol), compounds **2** (5.00 g, 6.9 mmol), and tetrakis(triphenylphosphine)palladium (0.47 g, 0.4 mmol), and sodium carbonate (2 M, 20 mL) were reacted by using the procedure described for B-DDP. After the reaction, the mixture was cooled to room temperature, filtered, and washed with ethanol. T-DDP was purified by recrystallization from toluene (3.54 g, 69% yield). m.p. 300 °C. ^{1}H NMR (400 MHz, DMSO-d_6): δ 7.61 (d, 8H, J = 8.8 Hz), 7.49 (d, 4H, J = 5.1 Hz), 7.42 (d, 4H, J = 5.1 Hz), 7.12 (t, 4H, J = 5.1 Hz), 7.10 (d, 8H, J = 8.8 Hz), 7.09 (s, 4H). MS (MALDI-TOF): *m/z* 740.03 $[M+H]^+$. Anal. calcd (%) for $C_{46}H_{32}N_2S_4$: C 74.56, H 4.35, N 3.78; found: C 74.64, H 4.37, N 3.84.

Synthesis of BT-DDP. 2-Benzo[*b*]thiophene boronic acid (7.20 g, 41 mmol), compounds **2** (5.00 g, 6.9 mmol), tetrakis(triphenylphosphine)palladium(0.47 g, 0.4 mmol), and sodium carbonate (2 M, 20 mL) were reacted by using the procedure described for B-DDP. After the reaction, the mixture was cooled to room temperature, filtered, and washed with ethanol. BT-DDP was purified by recrystallization from toluene (4.10 g, 63 % yield). m.p. 372 °C. ^{1}H NMR (400 MHz, $CDCl_3$): δ 7.82 (d, 4H, J = 7.7 Hz), 7.76 (d, 4H, J = 7.7 Hz), 7.65 (d, 8H, J = 8.8 Hz), 7.49 (s, 4H), 7.35–7.31 (m, 8H), 7.21 (d, 8H, J = 7.7 Hz), 7.14 (s, 4H). MS (MALDI-TOF): *m/z* 940.11 $[M+H]^+$. Anal. calcd (%) for $C_{62}H_{40}N_2S_4$: C 79.11, H 4.28, N 2.98; found: C 79.15, H 4.23, N 2.93.

2-4. Wide-range variable angle spectroscopic ellipsometry (VASE) analysis

Figure 2-1 shows geometric and electronic structures of DDP derivatives obtained by molecular mechanics (MMFF94s)[19] and quantum chemical calculation (B3LYP/6-31G(d)). The central DDP backbone units, i.e., tetraphenylbenzene-1,4-diamine, have a highly planar structure since the nitrogen atoms are sp^2-hybridized. Table 2-1 shows the transition dipole moments and transition energies for the three lowest excited states of DDP derivatives estimated by a time-dependent density functional theory calculations.[20] Although most of rod-like molecules have one direction of transition dipole moment along the longest molecular axis,[13] two different directions for transition dipole moments in DDP derivatives were found, nearly parallel to the *x* and *y* molecular axes. The two transition dipole moments have similar amplitudes, and the excitation energies attributed to them are also very close. This result indicates that DDP derivatives have two-dimensional planar electronic structures.

Figure 2-2 shows the results of VASE analysis of 100 nm-thick films of DDP derivatives deposited on silicon (100) substrates. The surface morphology of the DDP films was investigated by atomic force microscopy. These surfaces are very smooth with small root-mean-square (RMS) values of the surface roughness: **B-DDP** (0.7 nm), **T-DDP** (0.5 nm), and **BT-DDP** (0.4 nm). To determine the effects of the molecular orientation of these films, we investigated the optical anisotropy of the films by using VASE. When the molecules are anisotropically oriented in their films, the ordinary refractive indices and extinction coefficient are different from the extraordinary ones. It has been found that DDP derivatives clearly show a horizontal orientation based on the VASE measurement (Fig. 2-2).

Table 2-1. Components of the transition dipole moments (μ_x, μ_y, and μ_z) and excitation energies (E_{exc}) and wavelengths (λ_{exc}) for the five lowest energy excited states of BSB-Cz obtained from TD-B3LYP/6-311+G(d,p)//B3LYP/6-31G(d) calculations. The x-axis and z-axis lie along molecular axis of the DDP derivatives.

	B-DDP			**T-DDP**			**BT-DDP**		
Transition state	1st	2nd	3rd	1st	2nd	3rd	1st	2nd	3rd
μ_x [debye]	0	0	-7.62	0	0	8.82	0	-10.73	0
μ_y [debye]	0	0	-0.49	0	0	-0.23	0	0.21	0
μ_z [debye]	7.98	0	0	0	7.96	0	0	0	9.15
E_{exc} [eV]	3.14	3.16	3.20	2.97	3.00	3.01	2.86	2.90	2.93
λ_{exc} [nm]	394	392	387	418	413	412	433	428	423

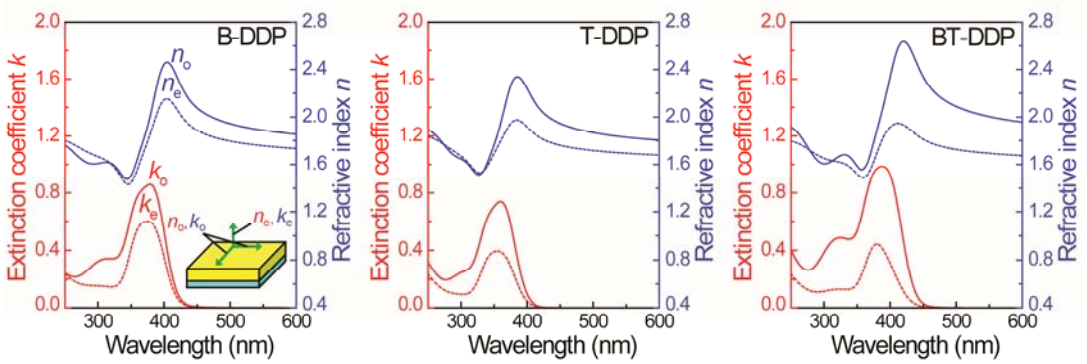

Figure 2-2. Ordinary (solid line) and extraordinary (dashed line) refractive indices (n_o and n_e) and extinction coefficients (k_o and k_e) of DDP derivatives determined by wide-range VASE measurement and analysis using uniaxial anisotropic model. Inset: direction of optical constants.

The orientation order parameter S, which is an index of molecular orientation, has been considered to explain the relationship between molecular orientation and the molecular structure.[10,21] For rod-like molecules such as BSB-Cz, S_{rod} is given by:

$$S_{rod} = \frac{3}{2} < \cos^2\theta > -\frac{1}{2} = \frac{k_e - k_o}{k_e + 2k_o}, \quad (1)$$

where <. . .> indicates an ensemble average, θ is the angle between the long molecular axis and the direction perpendicular to the substrate surface, and k_o and k_e are the ordinary and extraordinary extinction coefficients at the peak wavelength, respectively. For rod-like molecules, the last term in Eq. (1) is calculated using extinction coefficients that are determined

with uniaxial anisotropic models (S_{rod} = −0.5: completely parallel orientation; S_{rod} = 0: random orientation; S_{rod} = 1: completely perpendicular orientation). This is based on the assumption that the transition dipole moments parallel to the long molecular axis. However, for disk-like molecules, the transition dipole moment is extended into a two dimensional π-plane in the molecules.[22, 23] In the case of disk-like molecules with a four-fold rotational symmetry and two equivalent orthogonal transition dipole moments, such as phthalocyanines, the orientation order parameter can be re-defined S_{disk}:

$$S_{\mathrm{disk}} \equiv \frac{k_{\mathrm{e}}-k_{\mathrm{o}}}{k_{\mathrm{e}}+2k_{\mathrm{o}}}, \tag{2}$$

$$k_{\mathrm{e}} = k < \cos^2\theta >, \tag{3}$$

$$k_{\mathrm{o}} = \frac{1}{2}(k + k < \sin^2\theta >) = k(1 - \frac{1}{2} < \cos^2\theta >), \tag{4}$$

Combining Eqs. 2-4 gives:

$$S_{\mathrm{disk}} = \frac{k_{\mathrm{e}}-k_{\mathrm{o}}}{k_{\mathrm{e}}+2k_{\mathrm{o}}} = \frac{3}{4} < \cos^2\theta > -\frac{1}{2}, \tag{5}$$

where k is the hypothetical extinction coefficient in the case where all molecular planes are parallel to the direction of the electric field of incident light, and θ is the angle between the z-axis and the molecular plane (see also the inset in Fig. 2-3). The molecular orientation order parameter for disk-like molecules can then be obtained (S_{disk} = −0.5: completely parallel orientation, S_{disk} = 0: random orientation, S_{disk} = 0.25: completely perpendicular orientation) as shown in Figure 2-3. The values of S_{rod} and S_{disk} are determined from VASE analysis. The θ values for the "magic angle", which give the orientation parameter of zero, are 54.7° (rod-like) and 35.3° (disk-like), as can be calculated using Eqs. (1) and (5), respectively.

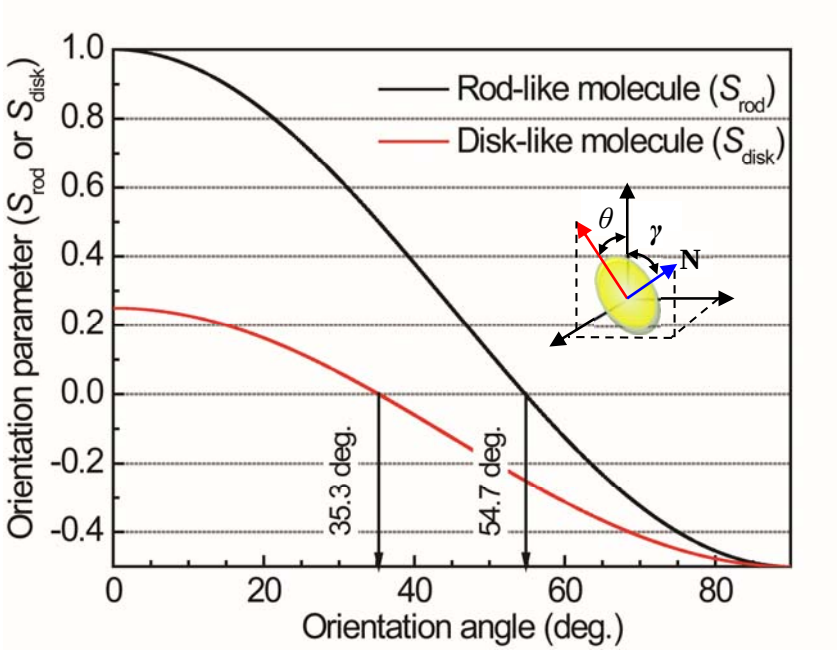

Figure 2-3. Orientation angle dependence of order parameter, when we hypothetically assume no distribution of the orientation angle. Inset: definition of θ for disk-like molecules having a four-fold rotational symmetry.

This orientation parameter for disk-like molecules can be used correctly only for molecules having two equivalent orthogonal transition dipole moments. Since the two transition dipole moments of the DDP derivatives are nearly equivalent and orthogonal, as shown in Table 2-1, this parameter can be approximately used to quantify the molecular orientation of these derivatives well. For the DDP derivatives, the S_{disk} values are **BT-DDP** (−0.23) < **T-DDP** (−0.18) < **B-DDP** (−0.11) < *N*,*N*′-diphenyl-*N*,*N*′-bis(1-naphthyl)-1,1'-biphenyl-4,4'-diamine (α-NPD)[1] (−0.01), indicating that DDP derivatives show a high tendency for horizontal orientation and that this can be enhanced by modifying the substituents of the end groups.

2-5. Effects of molecular orientation on carrier mobility.

Since DDP derivatives provide no clear transient photo-currents in time-of-flight (TOF) measurements, the carrier mobilities based on space-charge-limited currents (SCLCs) were evaluated.[24-26] The SCLC can be described by:

$$J = \frac{9}{8}\varepsilon_0\varepsilon\mu\frac{E^2}{L}, \tag{6}$$

where E is the electric field, ε and ε_0 are the relative dielectric constant and the permittivity of the free space, respectively, and L is the thickness of the organic layer. The relative dielectric constant ε is assumed to be 3.0 and the permittivity of the free space ε_0 is 8.85×10^{-14} C/Vcm. Figure 2-4 compares the *J-V* characteristics of hole only devices comprising indium tin oxide ITO/ MoO_3 (0.8 nm)/ HTL (300 nm)/ MoO_3 (10 nm)/ Al (100 nm) with α-NPD and DDP derivatives as the HTL. Here, the Poole-Frenkel compensation was introduced, since the mobility is dependent on the electric field. The Poole-Frenkel equation is given by

$$\mu(E) = \mu_0\exp(\beta\sqrt{E}), \tag{7}$$

where μ_0 is the zero-field mobility and β is the Poole-Frenkel factor. By combining Eqs.(6) and (7), the field-dependent SCLC can be expressed by[27]

$$J = \frac{9}{8}\varepsilon_0\varepsilon\frac{E^2}{L}\mu_0\exp(\beta\sqrt{E}), \tag{8}$$

Figure 2-4 shows that the fitted lines based on Eq. 8 agree well with the experimental data, and the SCLC mobility value of 6.74×10^{-4}cm^2/Vs was obtained for the 300 nm-thick α-NPD film, which is in good agreement with the previously reported value.[26] it has been found that the DDP derivatives and α-NPD have almost the same carrier mobilities of approximately 1×10^{-3} cm^2/Vs. Thus, the SCLC mobility measurements show that molecular orientation does not provide increased carrier mobilities in the DDP derivatives, although BSB-Cz films having strong horizontal orientation have been reported to have higher TOF mobility, compared with that of the unoriented films.[13]

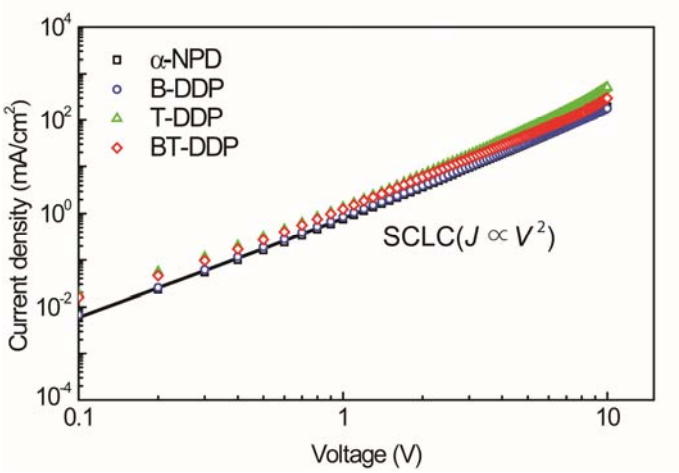

Figure 2-4. Current density (*J*) vs driving voltage (*V*) characteristics of hole-only devices comprising ITO/ MoO_3 (0.8 nm)/ HTL (300 nm)/ MoO_3 (10 nm)/ Al (100 nm) with α-NPD and DDP derivatives. The solid line represents the calculated *J*-*V* curve based on SCLC theory modified by Poole-Frenkel equation.

2-6. OLED characteristics

OLEDs with B-DDP, T-DDP, BT-DDP, and α-NPD as HTL were fabricated. As shown in Figure 2-5a, the devices with B-DDP, T-DDP, and BT-DDP demonstrated lower driving voltages (11.8 V, 10.2 V and 9.4 V, respectively) at 500 mA/cm^2, compared with that of α-NPD (12.4 V). In particular, BT-DDP showed the lowest driving voltage, i.e., a decrease of 3.5 V compared with the α-NPD-based OLED, which is consistent with the orientation result.

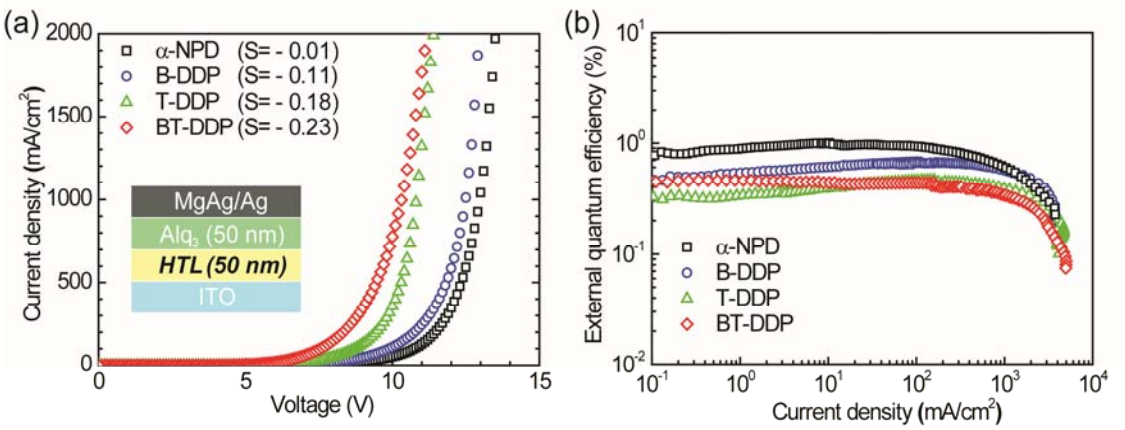

Figure 2-5. (a) Current density (J) vs driving voltage (V) and (b) external EL quantum efficiency (η_{EL}) vs J characteristics of double-layered OLEDs with DDP derivatives as HTL in ITO/ HTL (50 nm)/ Alq_3 (50 nm)/ MgAg (100 nm)/ Ag (10 nm). Symbols indicate the material and order parameters for the HTLs. Inset (a): Electric filed (E) vs J characteristics.

To clarify the mechanism of the low driving voltages, the relationship between the driving voltage at 500 mA/cm^2 and the orientation parameter, S, were plotted in Figure 2-6a. The driving voltage and orientation parameter were closely correlated, indicating that increased horizontal orientation of the HTLs provides lower driving voltage. Since the SCLC mobilities of these layers are almost same, the decrease in driving voltage from α-NPD to B-DDP, T-DDP, and BT-DDP can be attributed to a decrease in the hole injection barrier from the ITO anode. Figure 2-6b compares the HOMO levels of DDP layers and corresponding driving voltages. However, no clear correlation was observed between them.

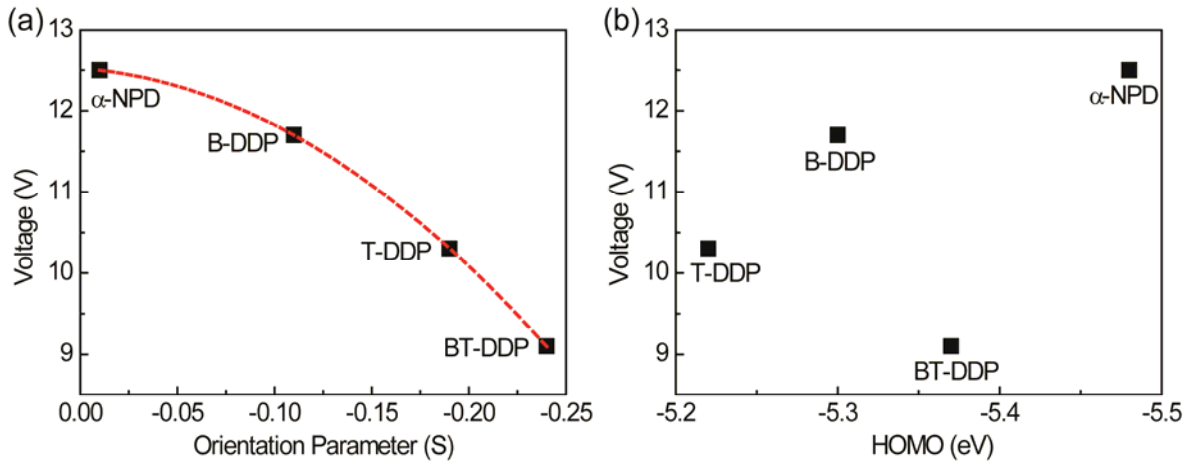

Figure 2-6. (a) Driving voltage of MgAg/Ag electrode at $J = 500$ mA/cm^2 (V) vs orientation parameter (S) and (b) driving voltage at $J = 500$ mA/cm^2 vs HOMO levels of HTLs.

Although lower driving voltage was achieved using the DDP derivatives, an appreciable decrease in the external EL quantum efficiencies was observed with these HTLs as shown in Figure 2-5b. This can be ascribed to a decrease in the charge carrier balance because of the enhancement of the hole current relative to the electron current. Thus, in other to enhance electron injection efficiency, a LiF/Al cathode was used instead of a MgAg/Ag one. The LiF (0.8 nm)/Al layer led to an enhancement of the electron injection, resulting in balanced carrier injection and transport and increased η_{ext} as shown in Figure 2-7 and Table 2-2.[28-30]

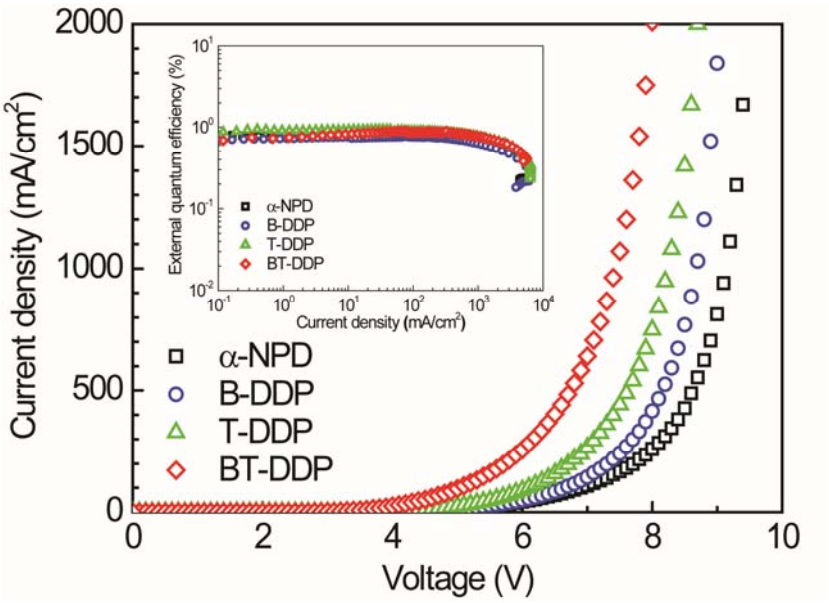

Figure 2-7. J-V characteristics of OLEDs comprising in ITO/ HTL (45 nm)/ α-NPD (5 nm)/ Alq_3 (50 nm)/ LiF (0.8 nm)/ Al (80 nm). Inset: J-η_{ext} characteristics.

TABLE 2-2. Driving voltage (V) at J = 500 mA/cm^2 and maximum EL efficiency (η_{max}) with electrode of MgAg/Ag and LiF/Al in OLEDs, and HOMO, LUMO, and orientation parameter (S) of hole transport layers.

	V (V)	η_{max} (%)	V (V)	η_{max} (%)	HOMO	LUMO	S
	(MgAg/Ag)		(LiF/Al)		(eV)	(eV)	
α-NPD	12.4	1.01	8.65	0.89	5.48	2.41	-0.01
B-DDP	11.8	0.70	8.13	0.78	5.30	2.42	-0.11
T-DDP	10.2	0.46	7.58	0.94	5.22	2.27	-0.18
BT-DDP	9.40	0.47	6.75	0.92	5.37	2.50	-0.23

Next, three OLEDs with different thickness of **BT-DDP** layers, i.e., (50-x)-nm-thick α-NPD (Fig. 2-8) were prepared. By comparing these devices, the contribution of the carrier injection barrier can be separated at the anode and the carrier transport mobility in the bulk of a **BT-DDP** layer. As shown in Figure 2-8, lower driving voltages were observed in all **BT-DDP** devices, almost independent of the **BT-DDP** thickness. Since the 2- and 5-nm-thick **BT-DDP** layers resulted in a significant decrease in driving voltage compared with that of the OLED having a neat α-NPD layer, it can be concluded that the ITO/**BT-DDP** interface provides a smaller barrier for hole injection, which can be ascribed to the planar orientation of the DDP molecules on the ITO surface.

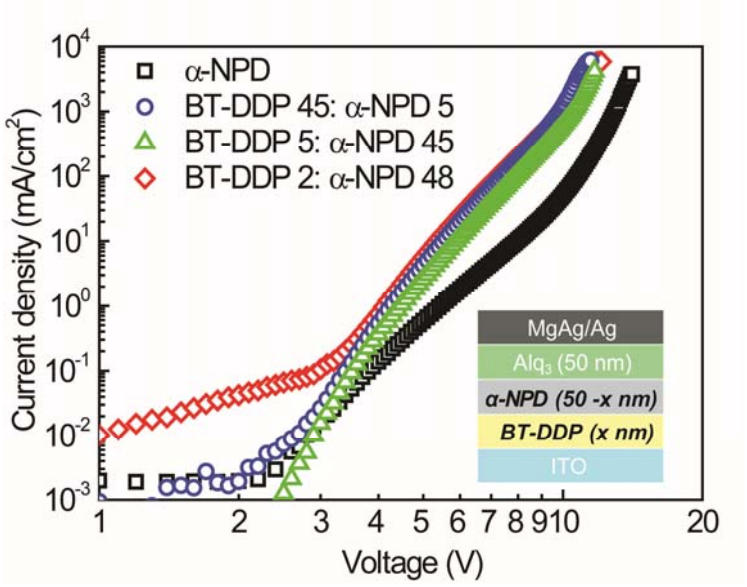

Figure 2-8. Characteristics of OLEDs comprising ITO/ **BT-DDP** (x nm)/ α-NPD (50-x nm) / Alq_3 (50nm)/ Mg:Ag (100 nm)/ Ag (10 nm) for various values of x. Inset: OLED structure.

To obtain clear evidence of molecular orientation affecting the OLED characteristics, we changed the molecular orientation by changing the substrate temperature during deposition of the organic layers. Molecular orientation in organic amorphous films can be systematically changed by controlling the substrate temperature during vacuum deposition.[13,31] The temperature-dependent VASE study revealed that **BT-DDP** showed the largest anisotropy at room temperature and the smallest anisotropy (i.e., complete randomization) at 150 °C on a silicon substrate, as shown in Figure 2-9. Here, it has been noted that the RMS value was slightly increased up to 1.7 nm at 150 °C, though the randomization of orientation and the increase of RMS values tend to depend on the roughness of substrate surface.[13]

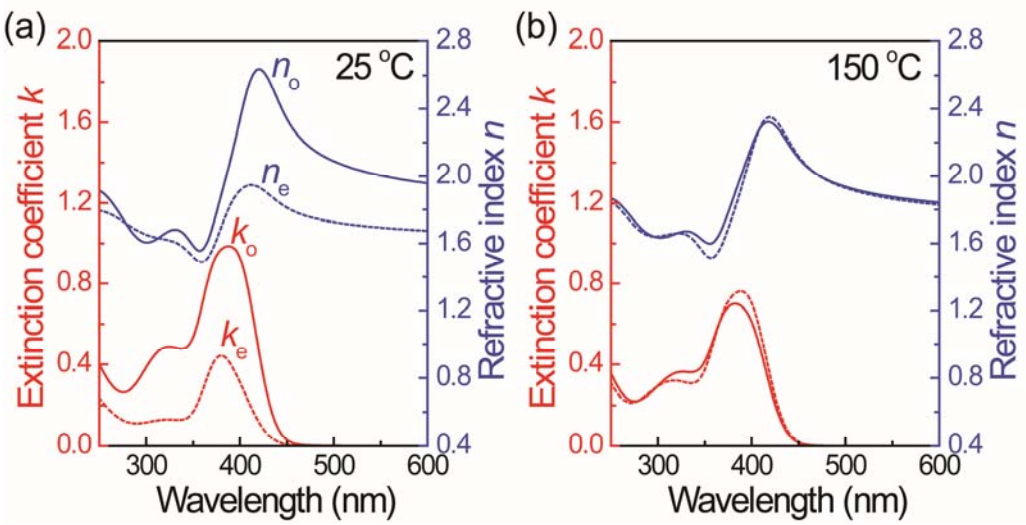

Figure 2-9. Ordinary (solid line) and extraordinary (dashed line) refractive indices (n_o and n_e) and extinction coefficients (k_o and k_e) of BT-DDP films deposited on Si substrate at (a) 25 °C and (b) 150 °C. Insets: schematics of (a) horizontal orientation and (b) random orientation.

Then, the **BT-DDP** layer was deposited at 150 °C during fabrication of an OLED and this OLED was compared to another one fabricated at room temperature. The OLED structure is ITO/ **BT-DDP** (5 nm) /α-NPD (45 nm)/ Alq_3 (50 nm)/MgAg (100 nm)/Ag (10 nm). In device A, all organic layers were deposited at room temperature, while for device B, the deposition of **BT-DDP** was conducted at a substrate temperature of 150 °C and the other organic layers were deposited at room temperature. As shown in Figure 2-10, in device B, the driving voltage was significantly increased, indicating that the randomization of **BT-DDP** molecules in the film resulted in a significant increase of driving voltage.

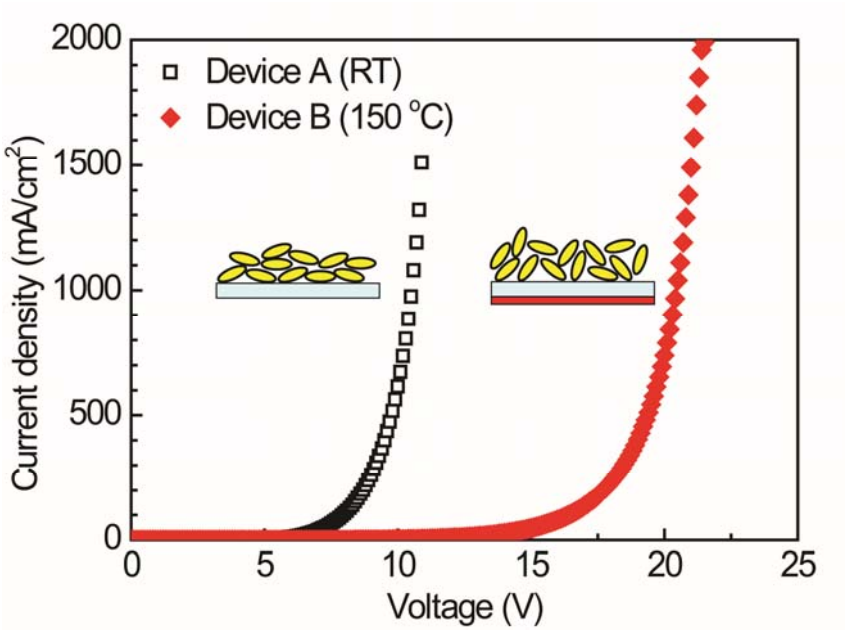

Figure 2-10. *J-V* characteristics of multi-layered OLEDs with different molecular orientation **of BT-DDP** (different annealing temperature). Inset: schematic illustration of molecular orientation.

The HOMO levels of the **BT-DDP** layers formed at room temperature and 150 °C are nearly same: 5.37 and 5.34 eV, respectively. This result clarified that the horizontal molecular orientation of **BT-DDP** molecules reduces the net carrier injection barrier at the anode interface, although the HOMO levels remain the same. When the factors that affect charge injection were thought in OLEDs, the energy levels (e.g. HOMO/LUMO levels vacuum levels) were usually discussed, but an overlap of wave functions between an the electrode and molecules was rarely discussed at the electrode interface, although the overlap of the wave functions certainly affects the injection.[32] Even if the HOMO levels of two films are the same, the overlaps of the wave functions at the interface with an electrode can be different, e.g., because of a difference in their molecular orientation. As shown in Figure 2-1, the HOMOs of DDP derivatives are distributed mainly at the central part of the molecules. A horizontal orientation is thus superior to a random orientation in terms of overlap between the wave function of a cathode and the HOMO of the molecules.

2-7. Conclusion

The DDP derivatives with a planar molecular structure, which showed enhanced horizontal molecular orientation compared with conventional hole transport materials such as α-NPD, were synthesized. Devices based on **B-DDP**, **T-DDP**, and **BT-DDP** demonstrated superior electrical characteristics in OLEDs, which was achieved because of a decrease in the hole injection barriers at the anode interfaces. The lowering of driving voltage even by a very thin layer of 2 nm supported this hypothesis. It has been found that the molecular orientation of **BT-DDP** affects not only carrier mobilities but also carrier injection barriers. Although it can be demonstrated in our previous study that BSB-Cz and Bpy-OXD films having strong horizontal orientation showed higher TOF mobility compared with that of the unoriented films,[12,13] DDP derivatives clearly showed large effect in reducing carrier injection barrier rather than enhancing carrier mobility by molecular orientation. Thus, the resultant physical improvement seems to be strongly dependent on molecular structures. The comprehensive study was further needed to clarify the relationship between carrier injection barrier and carrier mobility on molecular orientation and molecular structures.

2-8. References

[1] S. A. VanSlyke, C. H. Chen, C.W. Tang, *Appl. Phys. Lett*., **1996**, 69, 2160.

[2] C. W. Tang, S. A. VanSlyke, *Appl. Phys. Lett*., **1987**, 51, 913.

[3] Z. Deng, S. T. Lee, D. P. Webb, Y. C. Chan, W. A. Gambling, *Synth. Met*., **1999**, 107, 107.

[4] S. Naka, H. Okada, H. Onnagawa, Y. Yamaguchi, T. Tsutsui, *Synth. Met.*, **2000**, 111-112, 331.

[5] S. C. Tse, K. C. Kwok, S. K. So, *Appl. Phys. Lett.*, **2006**, 89, 262102.

[6] J. A. Woollam, B. Johs, C. M. Herzinger, J. Hilfiker, R. Synowicki, C. L. Bungay, *Proc. SPIE* **1999**, CR72, 3.

[7] T. Aimono, Y. Kawamura, K. Goushi, Yamamoto, H. Sasabe, C. Adachi, *Appl. Phys. Lett.*, **2005**, 86, 071110.

[8] M. Ichikawa, T. Kawaguchi, K. Kobayashi, T. Miki, K. Furukawa, T. Koyama, Y. J. Taniguchi, *Mater. Chem.*, **2006**, 16, 221.

[9] M. Ichikawa, N. Hiramatsu, N. Yokoyama, T. Miki, S. Narita, T. Koyama, and Y. Taniguchi, *Phys. Status Solidi RRL*, **2007**, 1, R37-R39.

[10] D. Yokoyama, A. Sakaguchi, M. Suzuki, C. Adachi, *Org. Electron.*, **2009**, 10, 127.

[11] D. Yokoyama, A. Sakaguchi, M. Suzuki, C. Adachi, *Appl. Phys. Lett.*, **2008**, 93, 173302.

[12] D. Yokoyama, A. Sakaguchi, M. Suzuki, C. Adachi, *Appl. Phys. Lett.*, **2009**, 95, 243303.

[13] D. Yokoyama, Y. Setoguchi, A. Sakaguchi, M. Suzuki, C. Adachi, *Adv. Funct. Mater.*, **2010**, 20, 386.

[14] K. Hisayuki, H. Chishio, K. Tadashi, N. Hiroaki, *PCT Int. Appl*., **1995.**

[15] M. Aonuma, T. Oyamada, H. Sasabe, T. Miki, C.Adachi, *Appl. Phys. Lett.*, **2007**, 90, 183503.

[16] B. C. Lin, C. P. Cheng, Z. P. M. Lao, *J. Phys. Chem. A*, **2003**, 107, 5241.

[17] V. Getautis, O. Paliulis, V. Gaidelis, V. Jankauskas, J. Sidaravicius, *J. Photochem. Photobiol. A: Chem.*, **2002**, 151, 39.

[18] B.C. Wanga, H. R. Liaoa, J. C. Changb, L. Chenb, J. T. Yeh, *J. Lumi.*, **2007**, 124, 333.

[19] T. A. Halgren, *J. Comp. Chem.*, **1996**, 17, 490.

[20] R. E. Stratmann, G. E. Scuseria, M. J. Frisch, *J. Chem. Phys.*, **1998**, 109, 8218.

[21] I. M. Ward, in *Structure and Properties of Oriented Polymers*, Appl. Sci. Publishers,

London, UK, **1975**.

[22] T. Komino, H. Tajima, M. Matsuda, *Chem. Lett.*, **2008**, 37, 690.

[23] T. Komino, H. Tajima, M. Matsuda, *Thin Solid Films*, **2008**, 517, 1358.

[24] P. W. M. Blom, M. J. M. de Jong, J. J. M. Vleggaar, *Appl. Phys. Lett.*, **1996**, 68, 3308.

[25] L. Bozano, S. A. Carter, J. C. Scott, G. G. Malliaras, P. J. Brock, *Appl. Phys. Lett.*, **1999**, 74, 1132.

[26] T. Matsushima, Y. Kinoshita, H. Murata, *Appl. Phys. Lett.*, **2007**, 91, 253504.

[27] T. Y. Chu, O. K. Song, *Appl. Phys. Lett.*, **2007**, 90, 203512.

[28] J. Kido, Y. Iizumi, *Appl. Phys. Lett.*, **1998**, 73, 3853.

[29] V. Choong, S. Shi, J. Curless, C. L. Shieh, H. C. Lee, F. So, J. Shen, J. Yang, *Appl. Phys. Lett.*, **1999**, 75, 172.

[30] V. Choong, S. Shi, J. Curless, F. So, *Appl. Phys. Lett.*, **2000**, 76, 958.

[31] D. Yokoyama, C. Adachi, *J. Appl. Phys.*, **2010**, 107, 123512.

[32] H. Ishii, K. Sugiyama, E. Ito, K. Seki, *Adv. Mater.*, **1999**, 11, 605.

Chapter 3

Bifunctional Star-Burst Amorphous Molecular Materials for OLEDs: Achieving Highly Efficient Solid-State Luminescence and Carrier Transport Induced by Spontaneous Molecular Orientation

3-1. Introduction

The rational design of organic molecular materials displaying efficient luminescence in solid states is a crucial research subject for achieving high-performance optoelectronic devices,[1] such as organic light-emitting diodes (OLEDs),[1a-c] light-emitting transistors,[2] and organic lasers.[3] For organic semiconductors to be used in such devices, it would be ideal to have luminophores with both efficient solid-state emission and high carrier transport capabilities. However, it is well-known that for most of organic semiconductors, the efficient luminescence observed in dilute solutions is generally weakened or quenched when the molecules aggregate in their condensed phase.[4] Such aggregation-caused fluorescence quenching is believed to dominate by the formation of delocalized excitons via strong intermolecular π– π interactions, which result in a long lifetime of excitons, red-shifted emission, and low luminescence quantum efficiency. An intriguing molecular approach to overcoming the concentration quenching was reported by Tang and coworkers in 2001, which they termed aggregation-induced emission (AIE).[5] They and other groups have been reported a series of AIE-active luminescent molecules including siloles,[5,6] cyanostilbenes,[7] and tetraphenylethene derivatives[1d,8] and iridium(III) complexes[9] so far, which are almost non-luminescent in dilute solution but turn into highly luminescent in concentrated (colloidal) solution or in films. Especially, the AIE-active tetraphenylethene derivatives[8] have recently been explored as an emitter for the fabrication of efficient OLEDs. Hence, the exploitation of innovative materials and design principles achieving both efficient luminescence and carrier transport properties in amorphous films remains an important challenge toward the development of further efficient devices.

In this study, two novel AIE-active star-burst molecules, named as **PDA-TPE** and **TPA-TPE** (Fig. 3-1), is designed by combining a hole-transporting *N,N,N′,N′*-tetraphenyl-*p*-phenylenediamine (PDA) or triphenylamine (TPA) core with triphenylethene (TPE) units. The resulting molecules can function as a bright solid-state emitter and an effective hole-transport amorphous material in OLEDs. Furthermore, it can be disclosed herein that spontaneous molecular orientation of the star-burst molecules in their amorphous thin films significantly affects the charge carrier transport properties as well as OLED efficiencies.

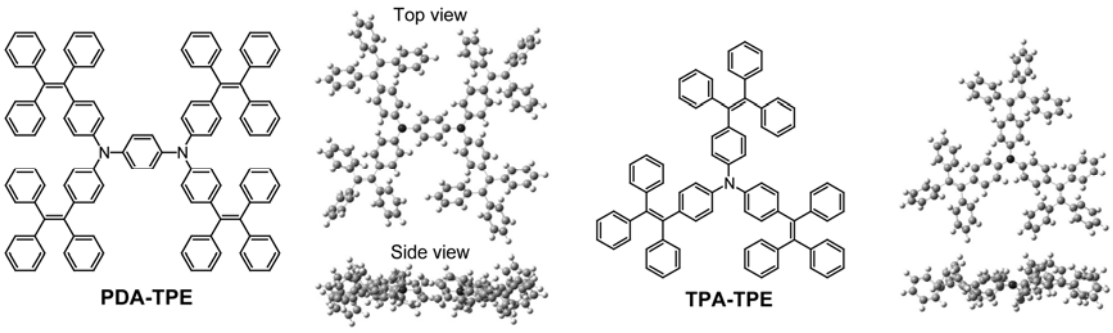

Figure 3-1. Chemical structures (left) and optimized geometries (right) of **PDA-TPE** and **TPA-TPE** determined by molecular mechanics and B3LYP/6-31G(d) calculations.

3-2. Synthesis and characterization

PDA-TPE and **TPA-TPE** were synthesized via Suzuki–Miyaura coupling reactions of 2-bromo-1,1,2-triphenylethylene with the corresponding boronic esters of PDA and TPA, respectively. The optimized molecular geometries of **PDA-TPE** and **TPA-TPE** have been determined using molecular mechanics (MMFF94s)[10] and density functional theory (DFT) B3LYP/6-31G(d) calculations. As illustrated in Figure 3-1, the multiple phenyl rings in the peripheral TPE units adopt a nonplanar, propeller-shaped conformation, which prevent the central PDA or TPA cores from the detrimental excimer formation in condensed solid states. To analyze the thermal properties of these materials, thermogravimetric analysis (TGA) and differential scanning calorimetry (DSC) have been carried out. **PDA-TPE** and **TPA-TPE** are thermally stable materials with 5% weight-loss temperature (T_d) over 490 °C. These star-burst molecules also possess good morphological stability, as confirmed by their high glass-transition temperature (T_g) of 151 °C (**PDA-TPE)** and 127 °C (**TPA-TPE**), respectively, which should arise from the rigid aromatic scaffolds of the TPE units. These Tg values are substantially higher than those of the commonly used triphenylamine-based hole-transporting materials, such as 4,4'-bis[*N*-(1-naphthyl)-*N*-phenyl]biphenyl diamine (α-NPD; T_g ~ 95 °C) and *N,N'*-bis(3-methylphenyl)-*N,N'*-diphenyl-1,1'-biphenyl-4,4'-diamine (TPD; T_g ~ 65 °C).[11] The high thermal and morphological stabilities of **PDA-TPE** and **TPA-TPE** as hole-transporting and emitting materials are advantageous for the fabrication of stable and durable OLED devices.

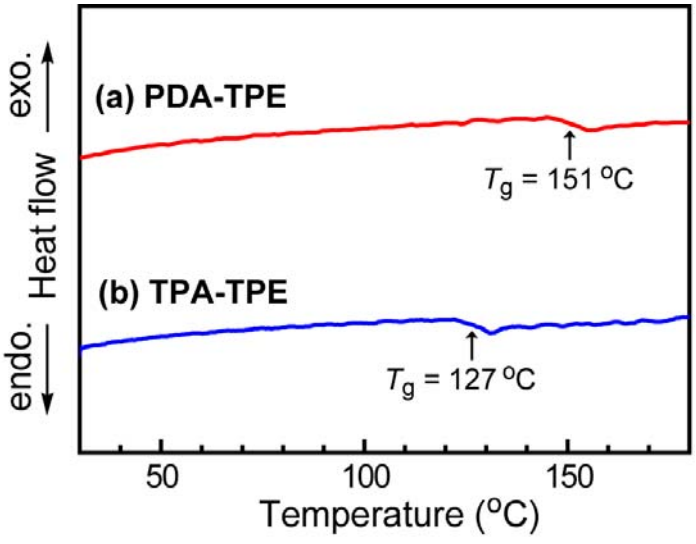

Figure 3-2. DSC thrmograms of **PDA-TPE** and **TPA-TPE** at 5 °C min^{-1}.

3-3. Experimental

3-3-1. General

^{1}H and ^{13}C NMR spectra were recorded on a Bruker Avance III 500 spectrometer. Chemical shifts of ^{1}H and ^{13}C NMR signals were quoted to tetramethylsilane (δ = 0.00) and $CDCl_3$ (δ = 77.0) as internal standards. Matrix-assisted laser desorption ionization time-of-flight (MALDI-TOF) mass spectra were collected on a Bruker Daltonics Autoflex III spectrometer using dithranol as the matrix. Elemental analyses were carried out with a Yanaco MT-5 CHN corder. UV/Vis absorption and photoluminescence (PL) spectra were measured with a Shimadzu UV-2550 spectrometer and a Horiba Fluoromax-4 spectrophotometer, respectively. PL quantum yields were measured using an integration sphere system coupled with a photonic multichannel analyzer (Hamamatsu Photonics C9920-02, PMA-11). The HOMO energy levels of thin films were determined using a Riken-Keiki AC-3 ultraviolet photoelectron spectrometer. The LUMO energy levels were estimated by subtracting the optical energy gap (E_g) from the measured HOMO energy levels; the E_g values were determined from the onset position of absorption spectra of the thin films. The density-functional theory (DFT) calculations were performed on the Gaussian 03 program package, using the B3LYP functional with the 6-31G(d) basis set. X-ray diffraction (XRD) patterns were obtained using a Rigaku Ultima IV diffractometer with Cu$K\alpha$ radiation. Thermogravimetric analysis (TGA) and differential scanning calorimetry (DSC) measurements were performed on a Shimadzu DTG-60AH at a scanning rate of 10 °C min^{-1} and a Netzsch DSC204 Phoenix calorimeter at a scanning rate of 5 °C min^{-1}, respectively

3-3-2. OLED device fabrication and measurements

ITO-coated glass substrates were cleansed with detergent, deionized water, acetone, and isopropanol, followed by UV-ozone treatment. Organic layers and metal electrodes were deposited by high-vacuum thermal evaporation onto the ITO substrates. The layer thickness and the deposition rate were monitored in situ during the deposition by an oscillating quartz thickness monitor. The current density–voltage–luminance characteristics of the devices were measured using a semiconductor parameter analyzer (Agilent E5273A) and an optical powermeter (Newport 1930-C).

3-3-3. Variable-angle spectroscopic ellipsometry (VASE)

Thin films for the ellipsometry measurements were deposited onto Si (100) substrates, which were precleaned by detergent and organic solvents. VASE was performed using a fast spectroscopic ellipsometer (M-2000U, J. A. Woollam Co. Inc.). Seven different angles of the incident light from 45° to 75° with steps of 5° were used. At each angle, the experimental ellipsometric parameters Ψ and Δ were obtained simultaneously in 1.6-nm steps from 245 to 1000 nm. The VASE data were analyzed using WVASE32 software.

3-3-4. Materials and syntheses

Commercially available reagents and solvents were used without further purification unless otherwise noted. All of the reactions were performed under an N_2 atmosphere in dry solvents. The synthetic routes for **PDA-TPE** and **TPA-TPE** are outlined in Scheme 3-1. Tris(4-bromophenyl)amine (**3**) and 2-bromo-1,1,2-triphenylethylene were purchased from Tokyo Chemical Industry (TCI). *N*,*N*,*N*',*N*'-Tetrakis(4-bromophenyl)benzene-1,4-diamine (**1**) and tris[4-(4,4,5,5-tetramethyl-1,3,2-dioxaborolan-2-yl)phenyl]amine (**4**) were prepared according to the literature. All of reactions were performed under an Ar atmosphere in dry solvents unless otherwise noted.

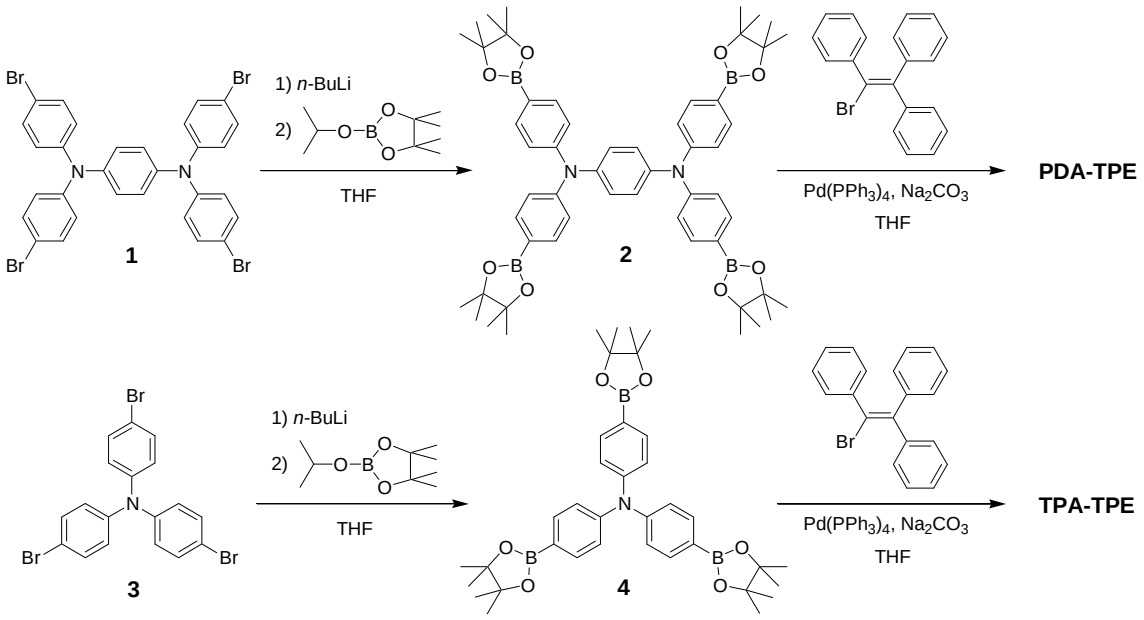

Scheme 3-1. Synthesis of **PDA-TPE** and **TPA-TPE**.

Synthesis of compound 2. To a stirred solution of **1** (1.00 g, 1.37 mmol) in dry THF (100

mL) was added dropwise *n*-butyllithium (1.62 M in hexane, 3.6 mL, 5.8 mmol) at −78 °C, and the mixture was allowed to react for 1 h at that temperature. 2-Isopropoxy-4,4,5,5-tetramethyl-1,3,2-dioxaborolane (1.12 g, 6.0 mmol) was then added, and the mixture was stirred overnight at room temperature. The reaction mixture was poured into a large amount of water, and extracted with chloroform. The combined organic layers were washed with water, and dried over anhydrous Na_2SO_4. After filtration and evaporation, the product was recrystallized from chloroform/ethanol, and dried under vacuum to afford **2** as a white solid (yield = 1.19 g, 95%). ^{1}H NMR (500 MHz, $CDCl_3$): δ 7.69 (d, J = 8.5 Hz, 8H), 7.08 (d, J = 8.5 Hz, 8H), 6.99 (s, 4H), 1.33 (s, 48H). ^{13}C NMR (125 MHz, $CDCl_3$): δ 150.01, 142.79, 135.94, 126.32, 122.65, 83.61, 24.88. MS (MALDI-TOF): m/z 916.74 $[M]^{+\cdot}$.

Synthesis of PDA-TPE. To a mixture of **2** (1.00 g, 1.1 mmol) and 2-bromo-1,1,2-triphenylethylene (2.04 g, 6.1 mmol) in dry THF (40 mL) were added $Pd(PPh_3)_4$ (0.13 g, 0.11 mmol) and aqueous Na_2CO_3 (2.0 M, 15 mL; Ar bubbled before use). The mixture was vigorously stirred under reflux for 48 h. After cooling to room temperature, the formed precipitate was collected by filtration and then washed with water and ethanol. The product was recrystallized from THF/methanol, and dried under vacuum to afford **PDA-TPE** as a yellow solid (yield = 1.12 g, 71%). This compound was further purified by repetitive temperature-gradient sublimation before use. ^{1}H NMR (500 MHz, $CDCl_3$): δ 7.11-7.00 (m, 60H), 6.83 (d, J = 9.0 Hz, 8H), 6.83 (s, 4H), 6.72 (d, J = 9.0 Hz, 8H). ^{13}C NMR (125 MHz, $CDCl_3$): δ 145.69, 144.06, 143.84, 143.66, 140.73, 140.41, 137.67, 132.05, 131.40, 131.37, 131.34, 127.62, 127.59, 127.57, 126.40, 126.33, 126.27, 125.34, 122.45. MS (MALDI-TOF): m/z 1429.93 $[M+H]^+$. Anal. calcd (%) for $C_{110}H_{80}N_2$: C 92.40, H 5.64, N 1.96; found: C 92.14, H 5.57, N 1.92.

Synthesis of compound 4. To a stirred solution of **3** (3.30 g, 6.84 mmol) in dry THF (120 mL) was added dropwise *n*-butyllithium (1.62 M in hexane, 13.0 mL, 21.1 mmol) at −78 °C, and the mixture was allowed to react for 1 h at that temperature. 2-Isopropoxy-4,4,5,5-tetramethyl-1,3,2-dioxaborolane (4.20 g, 22.6 mmol) was then added, and the mixture was stirred overnight at room temperature. The reaction mixture was poured into a large amount of water, and extracted with chloroform. The combined organic layers were washed with water, and dried over anhydrous Na_2SO_4. After filtration and evaporation, the product was

recrystallized from chloroform/ethanol and dried under vacuum to give **4** as a white solid (yield = 3.80 g, 89%). ^{1}H NMR (500 MHz, $CDCl_3$): δ 7.67 (d, J = 8.5 Hz, 6H), 7.07 (d, J = 8.5 Hz, 6H), 1.33 (s, 36H).

Synthesis of TPA-TPE. This compound was synthesized in a fashion similar to that above, using **4** (1.00 g, 1.6 mmol), 2-bromo-1,1,2-triphenylethylene (2.25 g, 6.7 mmol), and $Pd(PPh_3)_4$ (0.18 g, 0.16 mmol). The product was obtained as a yellow solid (yield = 0.94 g, 58%), and further purified by repetitive temperature-gradient sublimation. ^{1}H NMR (500 MHz, $CDCl_3$): δ 7.11-7.00 (m, 45H), 6.82 (d, J = 9.0 Hz, 6H), 6.69 (d, J = 9.0 Hz, 6H). ^{13}C NMR (125 MHz, $CDCl_3$): δ 157.48, 144.00, 143.82, 143.62, 140.69, 140.48, 137.99, 132.01, 131.40, 131.37, 131.34, 127.62, 127.60, 127.56, 126.40, 126.36, 126.29, 122.95. MS (MALDI-TOF): m/z 1007.70 $[M]^{+\cdot}$. Anal. calcd (%) for $C_{78}H_{57}N$: C 92.91, H 5.70, N 1.39; found: C 93.01, H 5.71, N 1.38 .

3-4. Optical properties

PDA-TPE and **TPA-TPE** show the lowest-energy absorption peak (λ_{abs}) at about 375 nm in tetrahydrofuran (THF) solution, which is 65 nm red-shifted compared to the π–π* absorption maximum of tetraphenylethene (λ_{abs} = 310 nm). The red-shifted absorption of **PDA-TPE** and **TPA-TPE** implies that the π -conjugation system should be elongated from the peripheral TPE units to the central PDA or TPA core through sp^2-hybridized nitrogen atoms. The absorption spectra for vacuum-deposited thin films are similar to those in solution (Fig. 3-3).

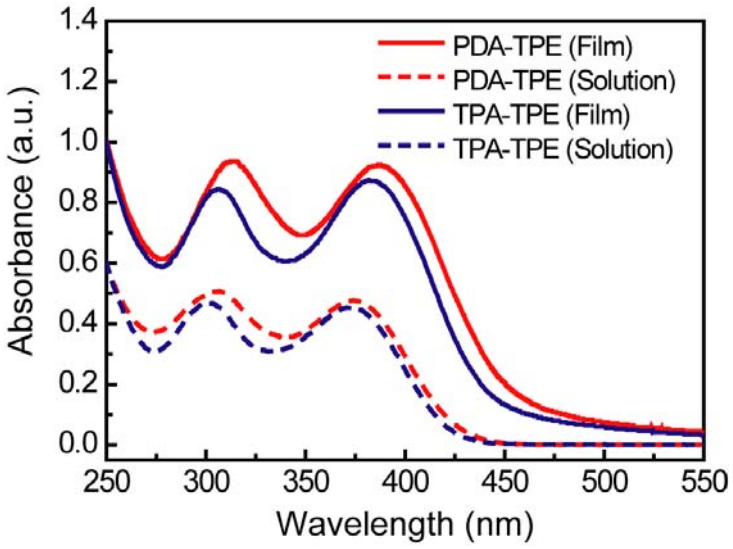

Figure 3-3. UV/vis absorption spectra of **PDA-TPE** (red) and **TPA-TPE** (blue) in THF solution (solid lines) and thin films (dashed lines).

Whilst both **PDA-TPE** and **TPA-TPE** are almost non-fluorescent in molecularly-dissolved solutions,[12] they emit green light intensely when irradiated with UV light in their both powdery aggregates and solid thin films (Fig. 3-4). The photoluminescence (PL) spectra of the **PDA-TPE** and **TPA-TPE** thin films exhibit the emission peak (λ_{PL}) at 520 and 510 nm, and indeed the PL quantum yields (Φ_{PL}) of those films measured using integrating sphere reach 73 ± 2% and 56 ± 2%, respectively, which values are higher than that of unsubstituted tetraphenylethene (Φ_{PL} = 27 ± 2%). Such remarkable PL enhancement in the solid states should be attributed to the AIE effect[1c,5] caused by the formation of molecular assemblies. It is noteworthy that the restriction of the intramolecular fragmental rotations in the propeller-shaped TPE moieties can suppress the non-radiative decay process and allow the star-burst molecules to emit light strongly even in the molecularly-condensed solid state.

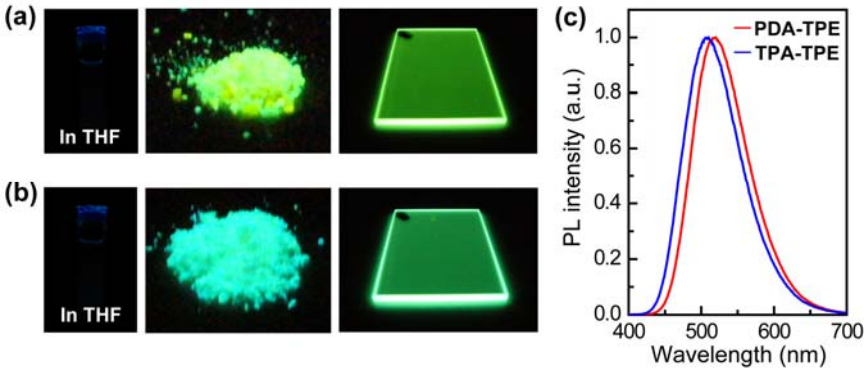

Figure 3-4. Photographs of (a) **PDA-TPE** and (b) **TPA-TPE** in 10^{-4} M THF solution (left), as powdery solids (center), and in vacuum-deposited thin films (right) under 365-nm UV light irradiation. (c) PL spectra of the thin films of **PDA-TPE** and **TPA-TPE**.

3-5. Charge carrier mobilities

Hole mobility, μ, is another important parameter for hole-transporting amorphous materials. The carrier transport properties of the **PDA-TPE** and **TPA-TPE** thin films were investigated by means of the space-charge-limited current (SCLC) tequnique.[13,14] Figure 3-4 shows the current density–voltage (*J–V*) characteristics of the hole-only devices based on **PDA-TPE**, **TPA-TPE**, as well as α-NPD, with the device configuration of ITO/MoO_3 (0.8 nm)/hole-transporting layer (HTL; 330–370 nm)/MoO_3 (10 nm)/Al (70 nm). As the voltage is increased, the current becomes space-charge limited with a nearly quadratic dependence on voltage, and the electrical characteristics can be expresses by the Mott–Gurney equation[13] (Eq. 1):

$$J = \frac{9}{8}\varepsilon_0\varepsilon\mu\frac{E^2}{L}$$

where E is the electric field, ε_0 is the free-space permittivity ($\varepsilon_0 = 8.85 \times 10^{-14}$ C/V cm), ε is the relative dielectric constant (assumed to be 3.0), L is the thickness of the HTL. Generally, the carrier mobility of the organic semiconductors is dependent on the electric field, and is thus described by the Poole–Frenkel formalism (Eq. 2):

$$\mu = \mu_0 exp\left(\beta\sqrt{E}\right)$$

where μ_0 is the zero-field mobility and β is the Pool–Frenkel factor. Based on equations 1 and 2, it has been revealed that the hole mobilities of the **PDA-TPE** and **TPA-TPE** thin films exceed 10^{-2} cm^2/Vs (Fig. 3-5). Obviously, the mobility values of **PDA-TPE** and **TPA-TPE** are of the highest level among those reported for hole-transporting amorphous molecular materials,[15] and the values are about one order of magnitude higher than that of α-NPD.

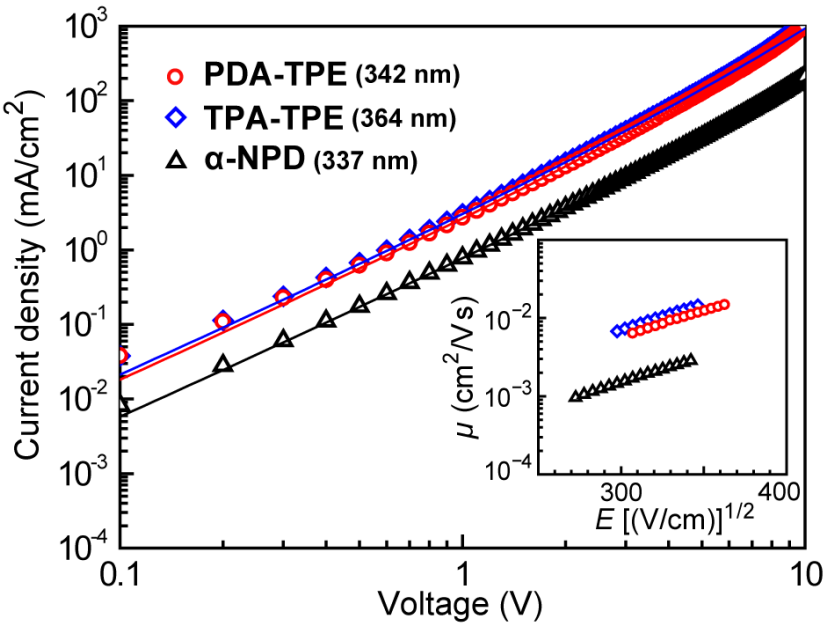

Figure 3-5. Double logarithmic plots of current density (J) versus applied voltage (V) characteristics of hole-only devices comprising ITO/MoO_3 (0.8 nm)/HTL (330–370 nm)/MoO_3 (10 nm)/Al (70 nm). The solid lines represent the best fits to the SCLC model. The inset shows the electric field dependence of hole mobility (μ) for the thin films of **PDA-TPE** (red), **TPA-TPE** (blue), and α-NPD (black) measured at room temperature.

3-6. Wide-range variable angle spectroscopic ellipsometry (VASE) analysis

To obtain deeper insights into the origin of such high carrier transport capability, the molecular orientation and optical anisotropy for the **PDA-TPE** and **TPA-TPE** thin films were analyzed using variable-angle spectroscopic ellipsometry (VASE).[16,17] As depicted in Figure 3-6, significantly large differences between the ordinary (i.e. in-plane) and extraordinary (i.e. out-of-plane) components of the extinction coefficients (k_o and k_e) and refractive indices (n_o and n_e) can be observed for both **PDA-TPE** and **TPA-TPE** amorphous thin films. The pronounced anisotropy in k_o and k_e at the peak of the π–π* absorption (388 and 384 nm, respectively) should be regarded as an implication of preferential orientation of the transition dipole moments parallel to the surface plane even in the amorphous thin films. The anisotropies in the molecular orientation can be rationalized by the orientation order parameter S, as given by the equation (Eq. 3):

$$S = \frac{k_e - k_o}{k_e + 2k_o}$$

Here, S = 0 when the molecules are randomly oriented, and S = −0.5 when they are completely oriented horizontally onto the substrate. The order parameters of the **PDA-TPE** and **TPA-TPE** thin films are calculated to be −0.28 and −0.27, respectively (Fig. 3-6), which suggests that the molecules involving two-dimensional prolonged π-systems have a strong tendency toward the parallel alignment onto the substrate, in spite of their bulky propeller-shaped TPE units. In contrast, it was previously reported that a vacuum-deposited thin film of α-NPD exhibited negligible anisotropy with respect to molecular orientation (S = −0.01).[17a] Therefore, the spontaneous horizontal molecular orientation would dominantly contribute to the enhancement of the hole mobility in the **PDA-TPE** and **TPA-TPE** thin films, because of a decrease in the positional and energetic disorders in the molecular-oriented states. The PDA and TPA cores retain their intrinsic hole-transporting functionality even after being substituted with the TPE peripheries. It should be noted here that for **PDA-TPE** and **TPA-TPE**, the molecular orientation was almost completely randomized after annealing the thin films for 5 min at elevated temperatures above T_g (e.g., 150–170 °C), which resulted in a decrease of the hole mobilities by an order of magnitude, compared to those with the horizontal molecular orientation (Fig. 3-7 and Fig. 3-8).

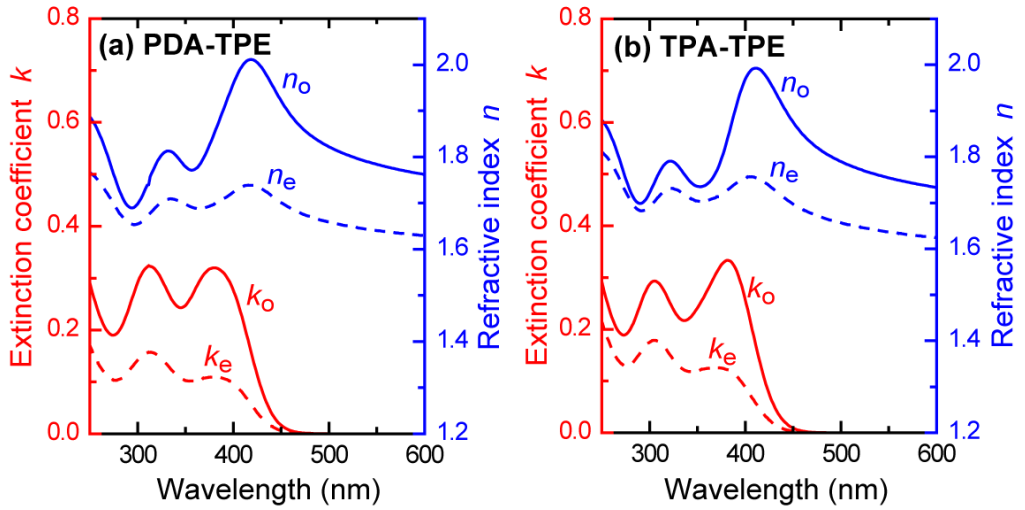

Figure 3-6. Ordinary (solid lines) and extraordinary (dashed lines) extinction coefficients (k_o and k_e) and refractive indices (n_o and n_e) determined by VASE measurements for the thin films of (a) **PDA-TPE** and (b) **TPA-TPE**.

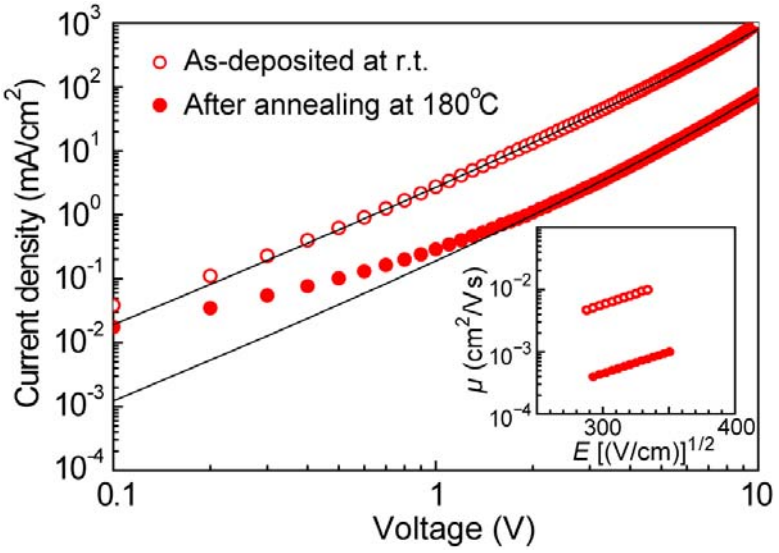

Figure 3-7. Double logarithmic plots of J–V characteristics (left panel) of hole-only devices based on **PDA-TPE** before and after thermal annealing for 5 min at 170 °C. The solid lines represent the best fits to the SCLC model. The inset shows the electric field dependence of hole mobility (μ) of the **PDA-TPE** thin film.

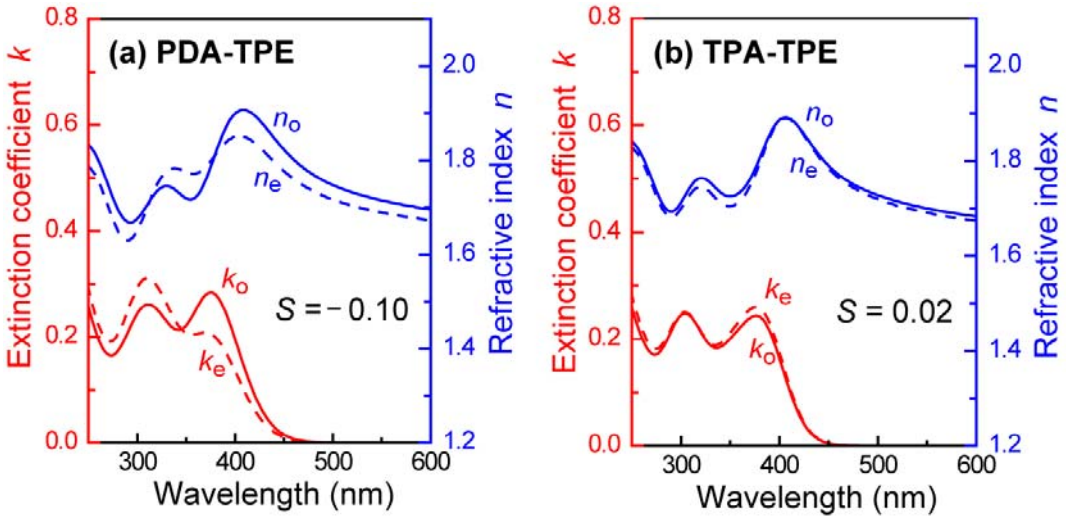

Figure 3-8. VASE measurements for thin films of (a) **PDA-TPE** and (b) **TPA-TPE** after thermal annealing for 5 min at 170 and 150 °C, respectively (right panel). No noticeable change in the orientation order parameter (*S*) has been observed even if varying the annealing time from 5 to 30 min.

3-7. OLED characteristics

Given the foregoing efficient solid-state emission and high carrier transport properties, **PDA-TPE** and **TPA-TPE** have been utilized as bifunctional materials, namely light-emitting and hole-transporting layers (LEL and HTL) in OLEDs. Simple bilayer OLEDs (Devices I and II) were fabricated with the device configuration of ITO/**PDA-TPE** or **TPA-TPE** (65 nm)/BPhen (35 nm)/LiF (0.8 nm)/Al (70 nm) (Fig. 3-9a), where 4,7-diphenyl-1,10-phenanthroline (BPhen) is chosen for an electron-transporting and hole-blocking layer, and LiF on the Al cathode is used as an electron-injection material. The current density–voltage–luminance (*J*–*V*–*L*) characteristics and the external electroluminescence (EL) quantum efficiencies (η_{ext}) of Devices I and II are shown in Figure 3-9b and c, and the OLED performances are also summarized in Table 3-1. It can be seen that the devices employing **PDA-TPE** and **TPA-TPE** as both HTL and LEL possess extremely low turn-on voltages (V_{on}) in the range of 2.4–2.6 V, and emit green light with EL maxima (λ_{EL}) at 523 and 510 nm, respectively. A match between the EL and PL spectra (Fig. 3-4c) manifests that the observed EL emission originates solely from the **PDA-TPE** and **TPA-TPE** luminophores in the devices; no emission at a longer wavelength due to exciplex species could be detected. These data attest that **PDA-TPE** and **TPA-TPE** work well as excellent bifunctional materials in the bilayer OLEDs. In comparison with Device II, Device I based on **PDA-TPE** shows better performances with higher maximum η_{ext} up to 4.5% on account of its higher Φ_{PL} in the thin film.

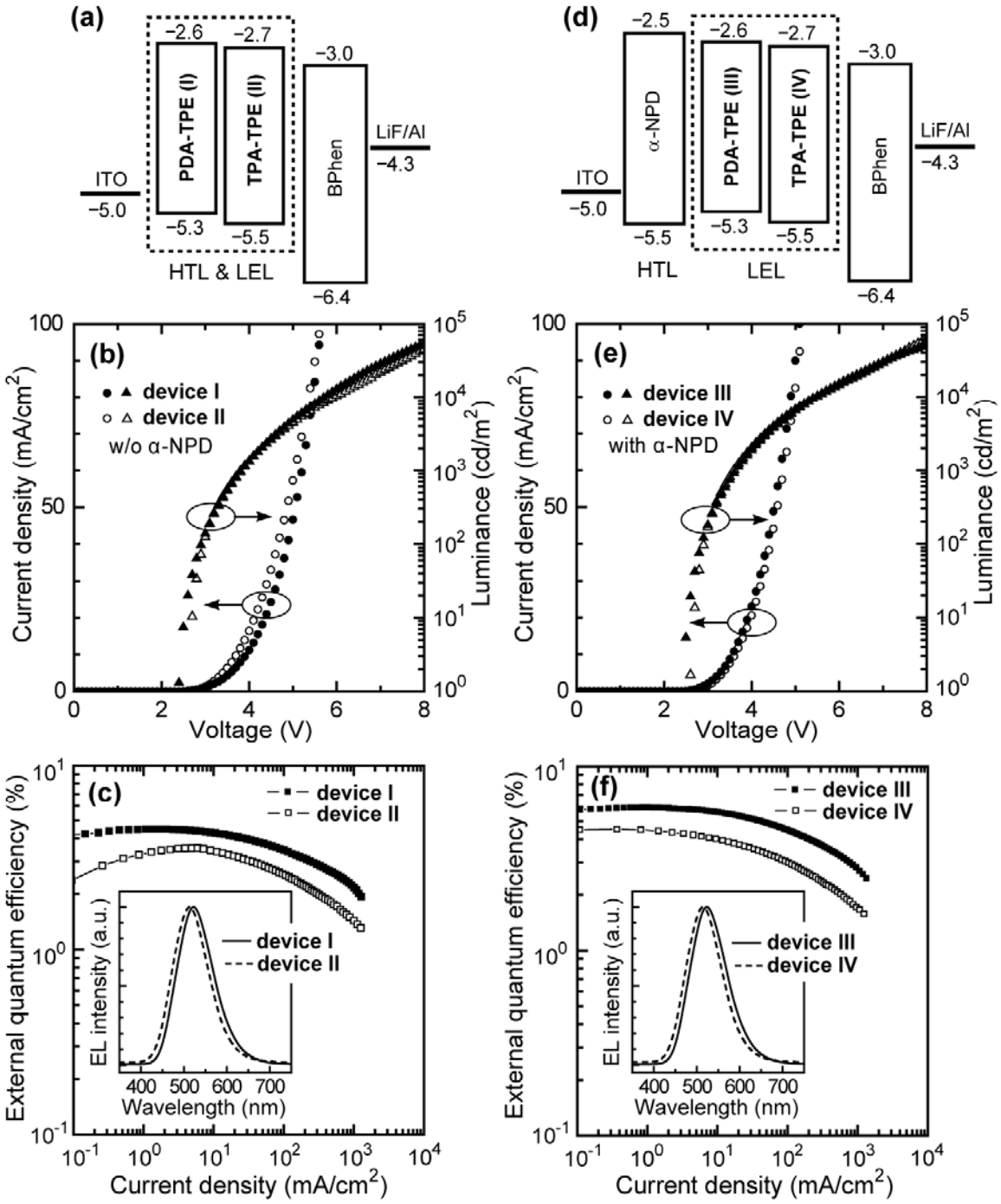

Figure 3-9. Energy-level diagrams (top panels; a, d), current density–voltage–luminance (*J–V–L*) plots (middle panels; b, e), and external EL quantum efficiency versus current density plots (bottom panels; c, f) of OLEDs incorporating **PDA-TPE** and **TPA-TPE** as light-emitting layer (LEL), with device configurations of ITO/LEL/BPhen/LiF/Al (Devices I and II; a–c) and ITO/α-NPD/LEL/BPhen/LiF/Al (Devices III and IV; d–f). The insets of the bottom panels represent EL spectra of each device taken at 10 mA/cm^2.

Table 3-1. OLED performances of **PDA-TPE** and **TPA-TPE**[a]

Device	LEL	HTL	λ_{EL} [nm]	V_{on} [V]	L_{max} [cd m^{-2}]	η_c [cd A^{-1}]	η_p [lm W^{-1}]	η_{ext} [%]
I	**PDA-TPE**	–	523	2.4	54200	14.4	14.1	4.5
II	**TPA-TPE**	–	510	2.6	48300	8.3	8.7	3.6
III	**PDA-TPE**	α-NPD	523	2.4	53600	15.9	16.2	5.9
IV	**TPA-TPE**	α-NPD	515	2.6	58300	14.3	15.0	4.5

[a] Device configuration: for Devices I and II, ITO/LEL (65 nm)/BPhen (35 nm)/LiF (0.8 nm)/Al (70 nm); for Devices III and IV, ITO/HTL (40 nm)/LEL (25 nm)/BPhen (35 nm)/LiF (0.8 nm)/Al (70 nm). Abbreviations: LEL = light-emitting layer; HTL = hole-transporting layer; λ_{EL} = EL emission maximum; V_{on} = turn-on voltage at 1 cd m^{-2}; L_{max} = maximum luminance; η_c = current efficiency at 100 cd m^{-2}; η_p = power efficiency at 100 cd m^{-2}; η_{ext} = maximum external EL quantum efficiency.

To further enhance the device performances, multilayer OLEDs (Devices III and IV) with the configuration of ITO/α-NPD (40 nm)/**PDA-TPE** or **TPA-TPE** (25 nm)/BPhen (35 nm)/LiF (0.8 nm)/Al (70 nm) have also been constructed and tested (Fig. 3-9d), in which **PDA-TPE** and **TPA-TPE** function as LEL and α-NPD serves as HTL. Both Devices III and IV with an additional α-NPD layer exhibit superior OLED performances in terms of the device efficiencies (Fig. 3-9e and f) compared to Devices I and II, while they give the same V_{on} and comparable luminance characteristics. Among the devices fabricated, Device III employing **PDA-TPE** as the LEL shows the best performance with a current efficiency (η_c) of 15.9 cd/A, power efficiency (η_p) of 16.2 lm/W, and η_{ext} of 5.9% (Table 3-1), presumably due to an optimal charge balance in the multilayer devices. Besides, the η_{ext} remains nearly 5% when the luminance is increased to ca. 10000 cd/m^2. According to the energy-level diagram of Devices III and IV (Fig. 3-9d), the additional α-NPD layer should also act as an electron blocker, and electron migration to the anode might be diminished, leading to efficient charge recombination within the LEL.

3-8. Effect of light out-coupling efficiency

The η_{ext}, that corresponds to the number of photons emitted from the OLED per charge carriers injected into the device, is generally given by the following equation[18] (Eq. 4):

$$\eta_{ext} = \gamma \times \eta_{st} \times \Phi_{PL} \times \eta_{out}$$

where, γ is the charge balance factor (ideally, $\gamma = 1$ if holes and electrons are fully balanced and recombined to form excitons), η_{st} is the singlet/triplet ratio (fluorescent emitters were assumed η_{st} = 25% because of the spin statistical limit of 1:3 for singlet-to-triplet excitons), Φ_{PL} is the quantum efficiency of the emitting material (Φ_{PL} = 73% for **PDA-TPE** and 56% for **TPA-TPE**), and η_{out} represents the light out-coupling factor. Typically, η_{out} is around 20%, which is derived from $\eta_{out} = 1 - (1 - 1/n^2)^{1/2}$, where n is the refractive index of the organic layers (normally about 1.7).[19] Taking those parameters into account, the theoretical values of η_{ext} for Devices III and IV can be estimated to be 3.6% and 2.8%, respectively. Apparently, the experimentally obtained η_{ext} of 5.9% (for Device III) and 4.5% (for Device IV) are approximately 1.6 times higher than the theoretical limits. It has been envisaged that the origin accounting for higher EL efficiencies should be attributed to the enhancement of η_{out} by horizontal orientation of the **PDA-TPE** and **TPA-TPE** molecules within the LEL. Recently, it has been reported that the transition dipoles of some linearly π-extended luminophores are not isotropic, but preferentially aligned horizontally in the OLED devices,[20] which should give rise to an increase of η_{out} by a factor of up to 1.6.[21]

In order to clarify the relationship between the molecular orientation and the OLED performances, the **PDA-TPE** and **TPA-TPE** layers featuring random molecular orientation, instead of the horizontally oriented LEL in Devices I and II, were adopted for the bilayer devices. For these devices, the deposition of only **PDA-TPE** or **TPA-TPE** layer was performed at substrate temperatures in the range of 150–170 °C, and the other layers were afterward deposited at room temperature, so that the orientation of **PDA-TPE** and **TPA-TPE** molecules was randomized in the LEL, as confirmed by the VASE measurements. It has been observed that the devices employing the randomly molecular-oriented **PDA-TPE** or **TPA-TPE** layer exhibit much lower maximum η_{ext} (3.2% and 1.7%, respectively) and maximum luminance (L_{max} = 21200 and 12900 cd/m^2, respectively) than those of Devices I and II (Fig. 3-10). These results indicate that the randomization of the luminescent molecules in LEL leads to

deterioration of the external EL efficiency as a consequence of lowering the hole mobility, i.e., unbalanced carrier recombination, and η_{out}.

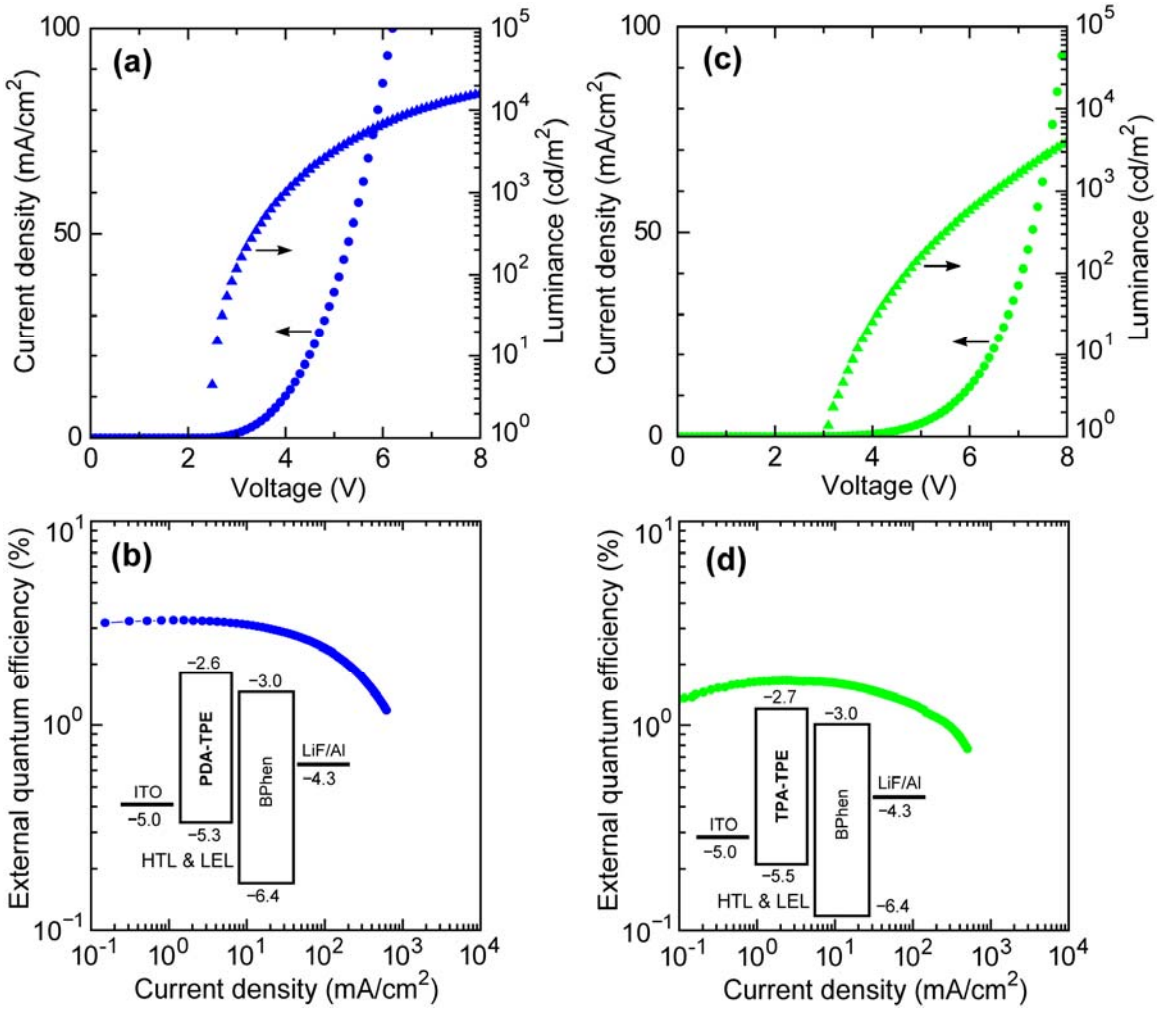

Figure 3-10. *J–V–L* plots (a,c) and external quantum efficiencies (b,d) of OLEDs incorporating randomly molecular-oriented **PDA-TPE** or **TPA-TPE** emitting layer, with device configuration of ITO/**PDA-TPE** or **TPA-TPE** (65 nm)/BPhen (35 nm)/LiF (0.8 nm)/Al (70 nm). The insets show energy-level diagrams of the OLEDs.

3-9. Conclusion

A versatile design strategy for achieving both efficient solid-state luminescence and high carrier transport properties has been exploited in this study. By introducing the multiple TPE peripheries onto the **PDA-TPE** and **TPA-TPE** cores, the resulting star-burst **PDA-TPE** and **TPA-TPE** molecules are endowed with strong AIE and horizontal orientation characteristics, and have indeed served as efficiently light-emitting and hole-transporting bifunctional amorphous materials in OLEDs. When utilized as the LEL in OLEDs, these materials display bright green EL emission at 510–530 nm with significantly high external quantum efficiencies up to 5.9%. It has been demonstrated that the spontaneous horizontal molecular orientation of the **PDA-TPE** and **TPA-TPE** luminophores in their thin films contributes to high external EL efficiencies of the devices by virtue of the enhancement of the hole mobility and the light out-coupling efficiency.

3-10. Reference

[1] a) *Organic Light-Emitting Devices: Synthesis, Properties and Applications* (Eds.: K. Müllen, U. Scherf), Wiley, Weinheim, Germany, **2006**; b) Special issue on High Efficiency Light Emitters, *Org. Electronics*, **2003**, 4, 45-198; c) Special issue on π-Functional Materials, *Chem. Mater.*, **2011**, 23, 309-922; d) Y. Hong, J. W. Y. Lam, B. Z. Tang, *Chem. Commun.*, **2009**, 4332; e) M. Shimizu, T. Hiyama, *Chem. Asian J.*, **2010**, 5, 1516; f) Y. Sagara, T. Kato, *Nat. Chem.*, **2009**, 1, 605.

[2] a) J. Zaumseil, H. Sirringhaus, *Chem. Rev.*, **2007**, 107, 1296; b) C. Santato, F. Cicoira, R. Martel, *Nat. Photon.*, **2011**, 5, 392.

[3] a) I. D. W. Samuel, G. A. Turnbull, *Chem. Rev.*, **2007**, 107, 1272; b) M. D. McGehee, A. J. Heeger, *Adv. Mater.*, **2000**, 12, 1655.

[4] a) J. B. Birks, *Photophysics of Aromatic Molecules*, Wiley, London, **1970**; b) A. C. Grimsdale, K. L. Chan, R. E. Martin, P. G. Jokisz, A. B. Holmes, *Chem. Rev.*, **2009**, 109, 897; c) S. W. Thomas III, G. D. Joly, T. M. Swager, *Chem. Rev.*, **2007**, 107, 1339.

[5] a) J. Luo, Z. Xie, J. W. Y. Lam, L. Cheng, H. Chen, C. Qiu, H. S. Kwok, X. Zhan, Y. Liu, D. Zhu, B. Z. Tang, *Chem. Commun.*, **2001**, 1740; b) B. Z. Tang, X. Zhan, G. Yu, P. P. S. Lee, Y. Liu, D. Zhu, *J. Mater. Chem.*, **2001**, 11, 2974.

[6] a) Y. Hong, J. W. Y. Lam, B. Z. Tang, *Chem. Commun.*, **2009**, 4332; b) Z. Zhao, Z. Wang, P. Lu, C. Y. K. Chan, D. Liu, J. W. Y. Lam, H. H. Y. Sung, I. D. Williams, Y. Ma, B. Z. Tang, *Angew. Chem. Int. Ed.*, **2009**, 48, 7608.

[7] a) B.-K. An, S.-K. Kwon, S.-D. Jung, S. Y. Park, *J. Am. Chem. Soc.*, **2002**, 124, 14410; b) B.-K. An, J. Gierschner, S. Y. Park, *Acc. Chem. Res.*, **2012**, 45, 544, and references cited therein.

[8] For recent examples: a) Z. Zhao, S. Chen, J. W. Y. Lam, P. Lu, Y. Zhong, K. S. Wong, H. S. Kwok, B. Z. Tang, *Chem. Commun.*, **2010**, 46, 2221; b) W. Z. Yuan, S. Chen, J. W. Y. Lam, C. Deng, P. Lu, H. H.-Y. Sung, I. D. William, H. S. Kwok, Y. Zhang, B. Z. Tang, *Chem. Commun.*, **2011**, 47, 11216; c) Y. Liu, S. Chen, J. W. Y. Lam, P. Lu, R. T. K. Kwok, F. Mahtab, H. S. Kwok, B. Z. Tang, *Chem. Mater.*, **2011**, 23, 2536; d) W. Z. Yuan, P. Lu, S. Chen, J. W. Y. Lam, Z. Wang, Y. Liu, H. S. Kwok, Y. Ma, B. Z. Tang, *Adv. Mater.*, **2010**, 22, 2159; e) C. Y. K. Chan, Z. Zhoo, J. W. Y. Lam, J. Liu, S. Chen, P. Lu, F. Mahtab, X.

Chen, H. H. Y. Sung, H. S. Kwok, Y. Ma, I. D. Williams, K. S. Wong, B. Z. Tang, *Adv. Funct. Mater.*, **2012**, 22, 378; f) J. Huang, X. Yang, X. Li, P. Chen, R. Tang, F. Li, P. Lu, Y. Ma, L. Wang, J. Qin, Q. Li, Z. Li, *Chem. Commun.*, **2012**, 48, 9586.

[9] a) Q. Zhao, L. Li, F. Li, M. Yu, Z. Liu, T. Yi, C. Huang, *Chem. Commun.*, **2008**, 685; b) Y. You, H. S. Huh, K. S. Kim, S. W. Lee, D. Kim, S. Y. Park, *Chem. Commun.*, **2008**, 3998.

[10] T. A. Halgren, *J. Comput. Chem.*, **1996**, 17, 490.

[11] D. F. O'Brien, P. E. Burrows, S. R. Forrest, B. E. Koene, D. E. Loy, M. E. Thompson, *Adv. Mater.*, **1998**, 10, 1108.

[12] The Φ_{PL} of **PDA-TPE** and **TPA-TPE** in THF solutions were determined to be 0.4–0.8%.

[13] a) M. A. Lampert, P. Mark, *Current Injection in Solids*, Academic Press, New York, **1970**; b) N. F. Mott, D. Gurney, *Electronic Processes in Ionic Crystals*, Academic Press, New York, **1970**.

[14] a) P. W. M. Blom, M. J. M. de Jong, J. J. M. Vleggaar, *Appl. Phys. Lett.*, **1996**, 68, 3308; b) L. Bozano, S. A. Carter, J. C. Scott, G. G. Malliaras, P. J. Brock, *Appl. Phys. Lett.*, **1999**, 74, 1132; c) Z. An, J. Yu, S. C. Jones, S. Barlow, S. Yoo, B. Domercq, P. Prins, L. D. A. Siebbeles, B. Kippelen, S. R. Marder, *Adv. Mater.*, **2005**, 17, 2580.

[15] For representative examples: a) H. Ohishi, M. Tanaka, H. Kageyama, Y. Shirota, *Chem. Lett.*, **2004**, 33, 1266; b) K. Okumoto, Y. Shirota, *Chem. Lett.*, **2000**, 29, 1034; c) T. Malinauskas, D. Tomkute-Luksiene, M. Daskeviciene, V. Jankauskas, G. Juska, V. Gaidelis, K. Arlauskas, V. Getautis, *Chem. Commun.*, **2011**, 47, 7770; d) J. Y. Kim, D. Yokoyama, C. Adachi, *J. Phys. Chem. C*, **2012**, 116, 8699.

[16] H. Fujiwara, *Spectroscopic Ellipsometry: Principles and Applications*, Wiley, New York, **2007**.

[17] a) D. Yokoyama, A. Sakaguchi, M. Suzuki, C. Adachi, *Appl. Phys. Lett.*, **2008**, 93, 173302; b) T. Komino, H. Nomura, M. Yahiro, C. Adachi, *J. Phys. Chem. C*, **2012**, 116, 11584; c) H.-W. Lin, C.-L. Lin, H.-H. Chang, Y.-T. Lin, C.-C. Wu, Y.-M. Chen, R.-T. Chen, Y.-Y. Chien, K.-T. Wong, *J. Appl. Phys.*, **2004**, 95, 881.

[18] a) T. Tsutsui, E. Aminaka, C. P. Lin, D.-U. Kim, Philos. *Trans. R. Soc. London, Ser. A*, **1997**, 355, 801; b) T. Tsutsui, *MRS Bull.*, **1997**, 22, 39.

[19] a) B. E. A. Saleh, M. C. Teich, *Fundamentals of Photonics*, Wiley, New York **1991**; b) S.

Nowy, B. C. Krummacher, J. Frischeisen, N. A. Reinke, W. Brütting, *J. Appl. Phys.*, **2008**, 104, 123109.

[20] a) J. Frischeisen, D. Yokoyama, A. Endo, C. Adachi, W. Brütting, *Org. Electron.*, **2011**, 12, 809; b) D. Yokoyama, A. Sakaguchi, M. Suzuki, C. Adachi*, Org. Electron.*, **2009**, 10, 127; c) D. Yokoyama, Y. Park, B. Kim, S. Kim, Y.-J. Pu, J. Kido, J. Park, *Appl. Phys. Lett.*, **2011**, 99, 123303; d) M. Taneda, T. Yasuda, C. Adachi, *Appl. Phys. Exp.*, **2011**, 4, 071602; e) R. Kondo, T. Yasuda, Y. S. Yang, J. Y. Kim, C. Adachi, *J. Mater. Chem.*, **2012**, 22, 16810.

[21] J. S. Kim, P. K. H. Ho, N. C. Greenham, R. H. Friend, *J. Appl. Phys.*, **2000**, 88, 1073.

Chapter 4

Polymorphism in 9,9-Diarylfluorene-Based Organic Semiconductors: Influence on Optoelectronic Functions

4-1. Introduction

Polymorphism is the ability of a single molecular species to self-organize in at least two different solid-state packing structures that display different physical and chemical properties.[1] Controlling polymorphism has been a subject of intense scrutiny in solid-state chemistry.[2] Recently, polymorphic behavior in π-conjugated molecules has attracted great deal of attention as a route to develop high-performance electro- and photofunctional organic materials.[3–6] Different polymorphs have been found in some organic semiconductor systems, such as pentacene,[3] oligothiophenes,[4] tetrathiafulvalenes,[5] and tris(8-hydroxyquinoline)aluminum (Alq_3),[6] which provide evidence for the large influence of solid structure on electronic properties. It is inferred that high charge carrier mobility can be attained when semiconducting molecules have strong interactions with neighboring ones to maximize intermolecular π-orbital overlap. However, the relationship between specific polymorphic solid structures and their (opto)electronic functions has not been thoroughly clarified. Hence, it will be extremely useful if there is a rational way for engineering polymorphism in organic semiconductors.

In this study, a new platform to control solid structure in organic semiconductors while enabling electronic functionality to be tailored without sacrificing phase purity is proposed. Two fluorene-based π-conjugated compounds (Fig. 4-1), 2,7-bis(5-phenylthiophen-2-yl)-9,9'-spirobifluorene (**SFPT**) and 2,7-bis(5-phenylthiophen-2-yl)-9,9-bis(1,1'-biphenyl-4-yl)-fluorene (**BFPT**), were focused because 9,9-diarylfluorene derivatives are promising candidates as efficient blue emitters and charge transport materials.[7] Herein, how variation of the C9 substituents and thermal treatment of these novel 9,9-diarylfluorene-based semiconducting materials can affect their polymorphic behavior and, as a consequence, their charge transport and luminescent properties is demonstrated.

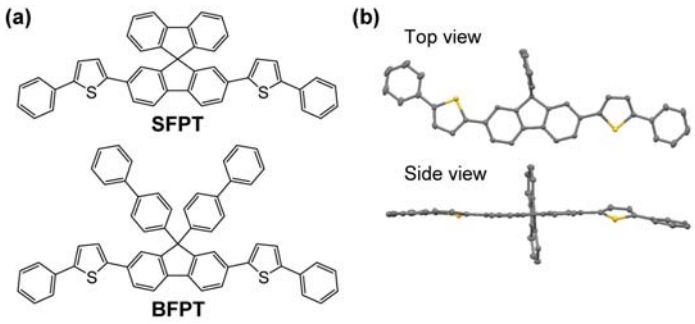

Figure 4-1. (a) Chemical structures of SFPT and BFPT. (b) ORTEP diagrams of the X-ray crystal structure of SFPT. Hydrogen atoms are omitted for clarity.

4-2. Experimental

4-2-1. General

^{1}H and ^{13}C NMR spectra were recorded on a Bruker Avance III 500 spectrometer. Chemical shifts of ^{1}H and ^{13}C NMR signals were quoted to tetramethylsilane (δ = 0.00) and $CDCl_3$ (δ = 77.0) as internal standards. Matrix-assisted laser desorption ionization time-of-flight (MALDI-TOF) mass spectra were collected on a Bruker Daltonics Autoflex III spectrometer using dithranol as the matrix. Elemental analyses were carried out with a Yanaco MT-5 CHN corder. UV/Vis absorption spectra were measured with a Shimadzu UV-2550 spectrometer. The HOMO energy levels were determined using a Riken-Keiki AC-3 ultraviolet photoelectron spectrometer. X-ray diffraction (XRD) patterns were obtained using a Rigaku Ultima IV diffractometer with Cu*K*α radiation. Thermogravimetric analysis (TGA) and differential scanning calorimetry (DSC) measurements were performed on a Shimadzu DTG-60AH at a scanning rate of 10 °C min^{-1} and a Netzsch DSC204 Phoenix calorimeter at a scanning rate of 5 °C min^{-1}, respectively, under N_2 atmosphere. AFM was performed using a JEOL JSPM-5400 scanning probe microscope with tapping-mode in air. X-ray crystallographic analysis was made on a Rigaku VariMax with a Saturn 724+ system with graphite monochromated Mo*K*α radiation. The structures were solved by direct methods (SIR2008)[8] and refined by full-matrix least-square techniques based on F^2 (SHELXL-97).[9]

4-2-1. Variable-angle spectroscopic ellipsometry (VASE)

Thin films for the ellipsometry measurements were deposited onto Si (100) substrates, which were precleaned by detergent and organic solvents. VASE was performed using a fast spectroscopic ellipsometer (M-2000U, J. A. Woollam Co. Inc.). Seven different angles of the incident light from 45° to 75° with steps of 5° were used. At each angle, the experimental ellipsometric parameters Ψ and Δ were obtained simultaneously in 1.6-nm steps from 245 to 1000 nm. The VASE data were analyzed using WVASE32 software.

4-2-2. Amplified spontaneous emission (ASE) measurements

Thin films of **SFPT** and **BFPT** (thickness = 100 nm) were deposited on glass substrates. The films were optically pumped using a N_2 gas laser (MNL200, Laser Technik) at a

wavelength of 337 nm with a pulse width of 500 ps and a repetition rate of 20 Hz. The ASE measurements were conducted by focusing the excitation light with an irradiation area of 400 μm × 10 mm. A detector (PMA-11, Hamamatsu Photonics) to observe the photoluminescence spectra was located on the edge of the films.

4-2-3. OFET device fabrication and measurements

SFPT and **BFPT** were incorporated into OFETs with a bottom-gate and top-contact geometry. For all of the OFET devices, heavily doped *n*-type Si wafers with a thermally grown 300-nm-thick SiO_2 layer were used as substrates. The SiO_2/Si substrates were pretreated with a piranha solution at 90 °C for 0.5 h, and then copiously cleaned by sonication in deionized water, acetone, and isopropanol in that order. The SiO_2/Si surface was treated with a self-assembled monolayer of hexamethyldisilazane (HMDS) by thermal evaporation for 1 h in air. The organic semiconductor layer of **SFPT** and **BFPT** was thermally evaporated on the substrates under high vacuum conditions. The devices were completed by evaporating gold (thickness = 50 nm) through a shadow mask to define the source and drain electrodes with a channel length of 20–100 μm on top of the organic layer. The output and transfer characteristics of the OFETs were measured using an Agilent B1500A semiconductor parameter analyzer under ambient conditions at room temperature. Field-effect mobilities (μ_{FET}) of the OFET devices were calculated in the saturation regime using the following equation: $I_D = (W/2L)\,\mu_{FET}\,C_i(V_G - V_{th})^2$, where I_D is the source–drain current, W and L are channel width and length, respectively, C_i is the capacitance per unit area of the gate dielectric (11 nF/cm^2), V_G is the gate voltage, and V_{th} is the threshold voltage.

4-2-4. Materials and syntheses

Commercially available reagents and solvents were used without further purification unless otherwise noted. All of the reactions were performed under an N_2 atmosphere in dry solvents. The synthetic routes for **SFPT** and **BFPT** are outlined in Scheme 4-1. 2,7-Dibromo-9,9'-spirobifluorene (**1**) and 2,7-dibromofluorenone (**2**) were purchased from TCI.

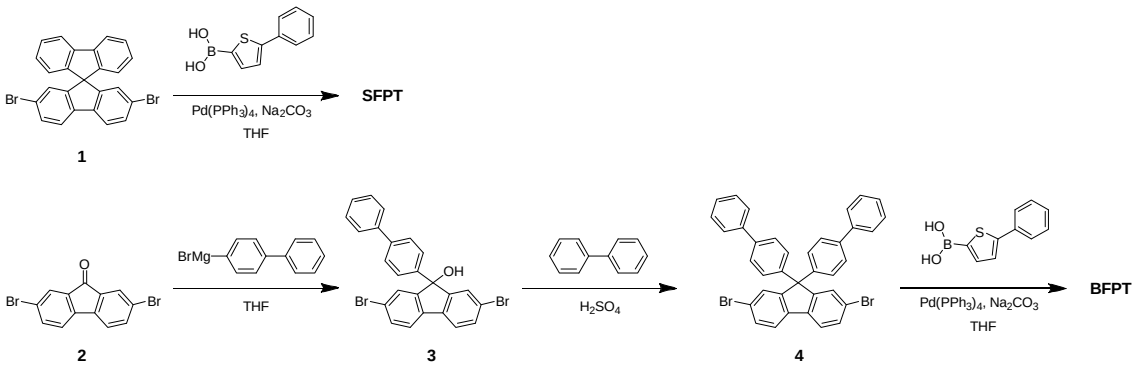

Scheme 4-1. Synthesis of **SFPT** and **BFPT**.

Synthesis of SFPT. To a mixture of **1** (2.00 g, 4.2 mmol) and 2-phenylthiophen-5-yl-boronic acid (1.82 g, 11.2 mmol) in dry THF (40 mL) were added $Pd(PPh_3)_4$ (0.30 g, 0.26 mmol) and aqueous Na_2CO_3 (2.0 M, 15 mL; Ar bubbled before use). The mixture was vigorously stirred under reflux for 48 h. After cooling to room temperature, the formed precipitate was collected by filtration and then washed with water and ethanol. The product was recrystallized from THF/methanol, and dried under vacuum to afford **SFPT** as a yellow solid (yield = 1.50 g, 56%). This compound was further purified by repetitive temperature-gradient sublimation before use. ^{1}H NMR (500 MHz, $CDCl_3$): δ 7.90 (d, J = 8.0 Hz, 2H), 7.84 (d, J = 8.0 Hz, 2H), 7.65 (dd, J = 7.5 Hz, 1.5 Hz, 2H), 7.54 (dd, J = 7.5 Hz, 1.0 Hz, 4H), 7.41 (d, J = 7.5 Hz, 2H), 7.33 (t, J = 7.5 Hz, 4H), 7.24 (t, J = 7.0 Hz, 2H), 7.16 (d, J = 4.0 Hz, 2H), 7.14 (t, J = 7.0 Hz, 2H), 7.11 (d, J = 4.0 Hz, 2H), 6.94 (d, J = 1.5 Hz, 2H), 6.82 (d, J = 7.5 Hz, 2H). ^{13}C NMR (125 MHz, $CDCl_3$): δ 149.97, 148.30, 143.50, 143.46, 141.82, 140.72, 134.22, 134.05, 128.85, 128.04, 127.93, 127.44, 125.61, 125.54, 124.26, 124.14, 123.85, 120.94, 120.44, 120.14, 65.99. MS (MALDI-TOF): m/z 633.37 $[M+H]^+$. Anal. calcd (%) for $C_{45}H_{28}S_2$: C 85.41, H 4.46; found: C 85.51, H 4.34.

Synthesis of 2,7-dibromo-9-biphenyl-9-hydroxyfluorene (3). 4-Biphenyl magnesium bromide was prepared from magnesium powders (694 mg, 28.6 mmol) and 4-bromobiphenyl (6.15 g, 26.4 mmol) in dry THF (40 mL). The obtained Grignard solution was diluted with dry THF (50 mL), and **2** (7.51 g, 22.0 mmol) was then added into the solution. The mixture was refluxed for 5 h. After cooling to room temperature, the reaction mixture was quenched with an aqueous NH_4Cl solution (10%). The organic layer was washed with brine and dried over anhydrous $MgSO_4$. After filtration and evaporation, the crude product was recrystallized from

toluene to give **3** as pale yellow crystals (yield = 7.60 g, 70%). ^{1}H NMR (500 MHz, $CDCl_3$): δ 7.32-7.57 (m, 15H), 2.49 (s, 1H). ^{13}C NMR (125 MHz, $CDCl_3$): δ 151.82, 140.64, 140.51, 137.48, 132.45, 128.72, 128.39, 127.31, 127.26, 127.04, 125.66, 122.52, 121.53, 83.21.

Synthesis of 2,7-dibromo-9,9-bis(biphenyl)fluorene (4). To a mixture of **3** (1.60 g, 3.2 mmol), biphenyl (4.92 g, 32 mmol), and acetic acid (15 g) were added dropwise H_2SO_4 (0.94 g, 9.6 mmol) at room temperature. The mixture was stirred for 3 h at 80 °C. After cooling to room temperature, the reaction mixture was poured into a large amount of water. The formed precipitate was collected by filtration, washed with water and ethanol, and recrystallized from ethanol/THF to yield **4** as colorless crystals (1.20 g, 62%). ^{1}H NMR (500 MHz, $CDCl_3$): δ 7.23-7.63 (m, 24H). ^{13}C NMR (125 MHz, $CDCl_3$): δ 152.84, 143.22, 140.41, 140.05, 138.03, 131.08, 129.45, 128.77, 128.31, 127.35, 127.24, 126.90, 121.92, 121.67, 65.25.

Synthesis of BFPT. This compound was prepared in a fashion similar to **SFPT**, using **4** (2.00 g, 3.2 mmol), 2-phenylthiophen-5-yl-boronic acid (1.82 g, 8.9 mmol), and $Pd(PPh_3)_4$ (0.25 g, 0.22 mmol). The product was obtained as a yellow solid (yield = 1.60 g, 64%). This compound was further purified by repetitive temperature-gradient sublimation before use. ^{1}H NMR (500 MHz, $CDCl_3$): δ 7.79 (d, J = 8.0 Hz, 2H), 7.72 (d, J = 1.5 Hz, 2H), 7.68 (dd, J = 8.0 Hz, 1.5 Hz, 2H), 7.61 (dd, J = 8.0 Hz, 2.0 Hz, 4H), 7.56 (dd, J = 8.0 Hz, 2.0 Hz, 4H), 7.52 (dd, J = 8.0 Hz, 1.5 Hz, 4H), 7.25-7.42 (m, 26H). ^{13}C NMR (125 MHz, $CDCl_3$): δ 145.69, 144.06, 143.84, 143.66, 140.73, 140.41, 137.67, 132.05, 131.40, 131.37, 131.34, 127.62, 127.59, 127.57, 126.40, 126.33, 126.27, 125.34, 122.45, 65.19. MS (MALDI-TOF): m/z 787.75 $[M+H]^+$. Anal. calcd (%) for $C_{57}H_{38}S_2$: C 86.99, H 4.87; found: C 87.02, H 4.73.

4-3. Optical properties

The thermal behavior of **SFPT** and **BFPT** was examined using differential scanning calorimetry (DSC) and variable-temperature polarizing optical microscopy (POM), as depicted in Figure 4-2. **SFPT** showed a glass transition at T_g = 128 ºC and a cold-crystallization transition at T_c = 175 ºC (enthalpy change, ΔH_c = 10.8 kJ mol^{-1}) prior to melting at T_m = 278 ºC (ΔH_m = 18.5 kJ mol^{-1}). In contrast, **BFPT** exhibited only a glass transition at T_g= 135 ºC. POM observation of **SFPT** revealed a marked change in microstructure at the first endothermic transition (175 ºC) from a pseudoisotropic texture to a highly birefringent dendritic crystalline architecture containing domains that were about 100 μm wide and several hundred micrometers long. At temperatures above T_m, birefringence of **SFPT** was completely lost under crossed polarizers, implying the material had melted. These initial experiments suggest that **SFPT** exhibits polymorphism with three different condensed phases, i.e., two amorphous states denoted as *a*- and *b*-phases, and a more thermodynamically stable crystalline state denoted as *c*-phase (Fig. 2). The spiro-type scaffold in **SFPT** with covalently bridged orthogonal configuration (Fig. 4-1) is robust and sterically less hindered than the two biphenyl substituents in **BFPT**, which allows such morphological bistability.

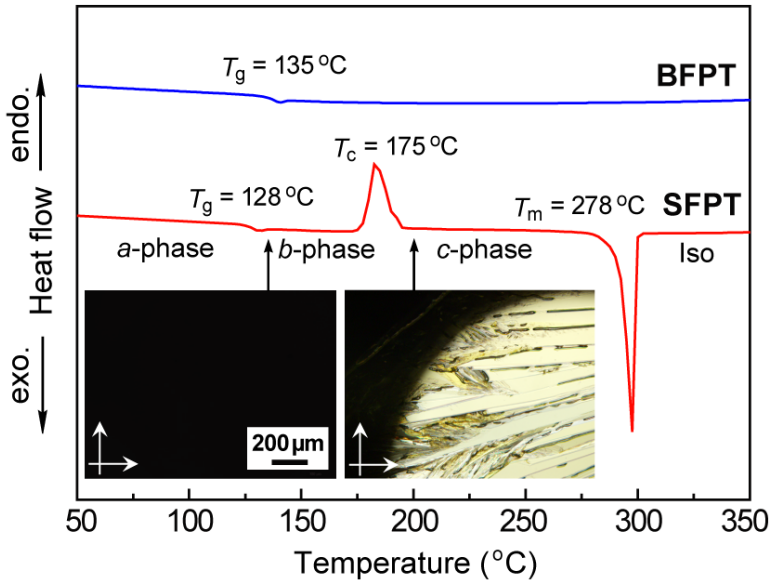

Figure 4-2. DSC traces obtained for SFPT and BFPT (2nd heating at 5 °C min^{-1}) and POM images of SFPT heated at 140 and 180 °C (left and right, respectively). SFPT shows polymorphism with two amorphous (*a*- and *b*-phases) and one crystalline (*c*-phase) states prior to isotropization (Iso). The arrows in the micrographs indicate the directions of polarizer axes.

The amorphous-to-crystalline transformation of **SFPT** was verified by out-of-plane X-ray diffraction (XRD) measurements (Fig. 4-3). No detectable reflections were observed for as-deposited films of **SFPT**, consistent with the POM observations. Upon heating the **SFPT** films at ~180 °C, an intense peak at 1.84 nm with a set of (00*l*) reflections appeared in the XRD patterns, implying that a crystalline polymorph with layered nanostructures was formed in the *c*-phase. Given that the molecular length of **SFPT** is 2.42 nm, this indicates that the **SFPT** molecules within the layers have an average tilt angle of 40° with respect to the normal direction. Inspection of the molecular structure indicates the two outside phenyl-thiophene units of the conjugated chromophore backbone are completely planar, which enhances π-conjugation, resulting in additional intermolecular interaction.

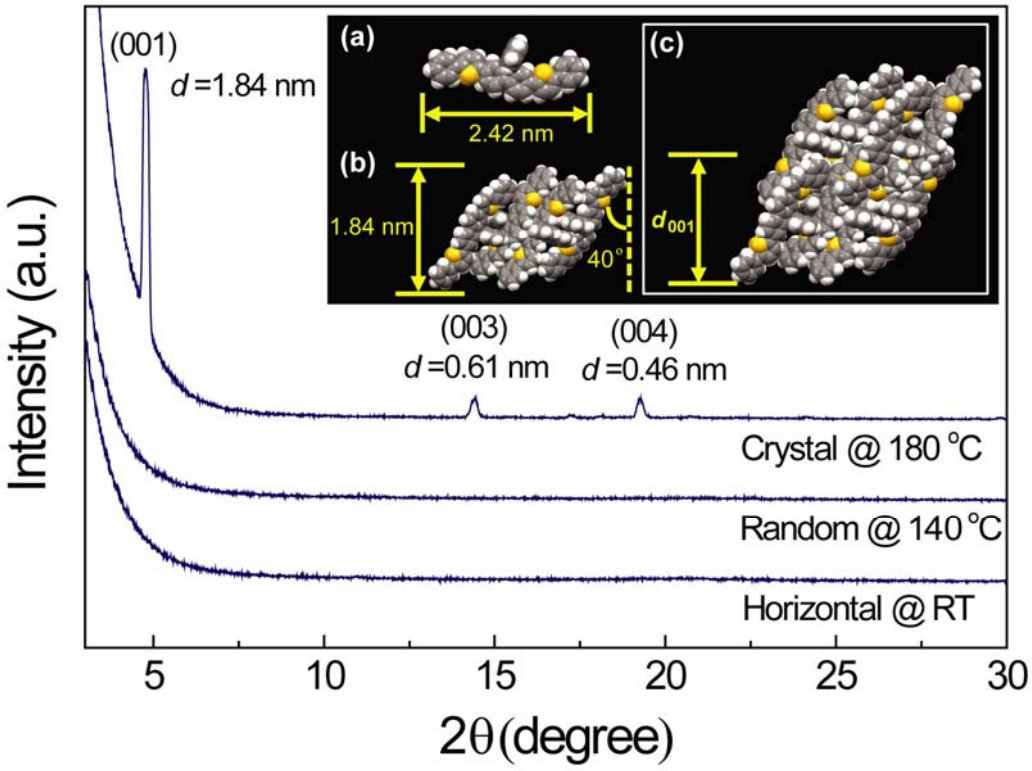

Figure 4-3. XRD patterns of **SFPT** films in *a*-phase (bottom), *b*-phase (middle), and *c*-phase (top). Insets show (a) molecular length, (b) interlayer distance (1.84 nm) and tilted molecular orientation with respect to the substrate normal, calculated from XRD and X-ray crystallography data, and (c) crystal packing structure of **SFPT**.

4-4. Charge carrier mobilities (μ_{SCLC})

To clarify the relationships between polymorphism and charge transport properties, the carrier mobilities (μ_{SCLC}) of **SFPT** and **BFPT** were evaluated by the steady-state space-charge-limited current (SCLC) technique.[10] Figure 4-4 displays the current density–voltage (*J*–*V*) characteristics of hole-only devices with a structure of indium-tin-oxide (ITO)/MoO_3 (0.8 nm)/**SFPT** and **BFPT** (300 nm)/MoO_3 (10 nm)/Al (70 nm). To fabricate these devices, **SFPT** films with *b*- and *c*-phase morphologies were prepared first by inducing formation of the respective polymorph at an elevated temperature (typically 140 and 180 °C, respectively) and subsequently quenching each structure by cooling to room temperature; the *a*-phase was readily obtained by vacuum deposition at room temperature. The SCLC characteristics for a single carrier are described by

$$J = \frac{9}{8}\varepsilon_0\varepsilon\mu\frac{E^2}{L}$$

$$\mu = \mu_0 exp\left(\beta\sqrt{E}\right)$$

where ε_0 is the free-space permittivity ($\varepsilon_0 = 8.85 \times 10^{-14}$ C V^{-1} cm^{-1}), ε is the relative dielectric constant (assumed to be 3.0), E is the electric field, L is the film thickness, μ_0 is the zero-field mobility, and β is the Poole–Frenkel factor.

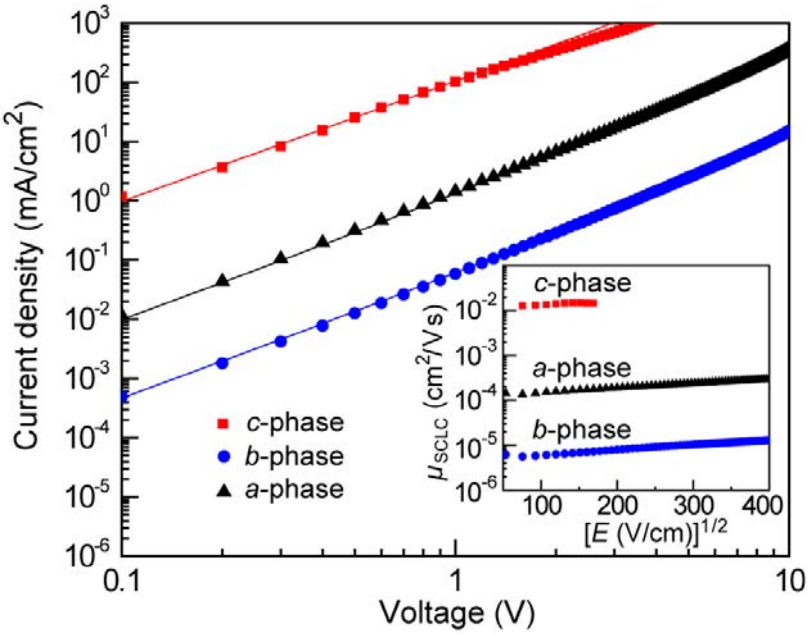

Figure 4-4. Double logarithmic plots of *J*–*V* characteristics of hole-only devices with the structure ITO/MoO_3 (0.8 nm)/**SFPT** (300 nm)/MoO_3 (10 nm)/Al (70 nm). The inset shows the electric-field dependence of hole mobility (μ_{SCLC}) for the **SFPT** films with *a*-, *b*-, and *c*-polymorphs.

As presented in Fig. 4-4, clear steps of the hole mobility values were observed in **SFPT** at each phase transition. The solid lines represent the best fits to the SCLC model. Pure *a*-phase was formed by deposition of **SFPT** at room temperature, and the *b*- and *c*-polymorphs were realized by heating the samples at 140 and 180 °C, respectively, and then cooling to room temperature. Note that the crystalline *c*-phase is more thermodynamically stable than the *a*-phase. The highest hole mobility of over 10^{-2} cm^2 V^{-1} s^{-1} was attained for the crystalline *c*-phase, and is about 2–3 orders of magnitude higher than those obtained for the amorphous morphologies. It is also noted that for **SFPT**, the hole mobilities in both amorphous states are different (μ_{SCLC} = ~10^{-4} and 10^{-5} cm^2 V^{-1} s^{-1} for *a*- and *b*-phases, respectively). These results unambiguously demonstrate that charge transport properties can be controlled by using the rich polymorphism of **SFPT**. In contrast, the observed mobilities for biphenyl-substituted **BFPT** in both pristine and annealed films were within the same order of magnitude (10^{-5} cm^2 V^{-1} s^{-1}, Fig. 4-5) and considerably lower than that of **SFPT** in the *a*-phase. Despite its orthogonal molecular configuration (Fig. 1b), the smaller lateral substituents of **SFPT** possibly allow effective intermolecular interactions and molecular orientation ordering, resulting in enhanced carrier mobility.

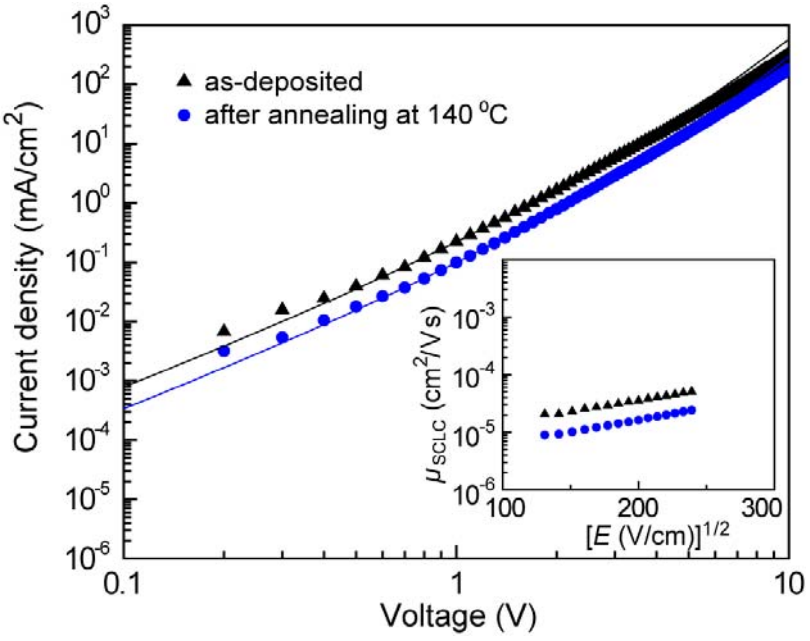

Figure 4-5. Double logarithmic plots of *J*–*V* characteristics of hole-only devices comprising ITO/MoO_3 (0.8 nm)/**BFPT** (300 nm)/MoO_3 (10 nm)/Al (70 nm). The solid lines represent the best fits to the SCLC model. The inset shows the electric-field dependence of hole mobility (μ_{SCLC}) for the **BFPT** films before and after thermal treatment at 140 °C for 10 min.

4-5. Wide-range variable angle spectroscopic ellipsometry (VASE) analysis

To gain further insight into the origin of such polymorphism-dependent carrier mobilities, molecular orientation and optical anisotropy of **SFPT** films comprising different polymorphs were investigated by variable-angle spectroscopic ellipsometry (VASE).[11] Figure 4-6a indicates that the ordinary (i.e., in-plane) extinction coefficient (k_o) and refractive index (n_o) are much larger than the extraordinary (i.e., out-of-plane) ones (k_e, n_e). This noticeable anisotropy at the peak of the π– π* absorption (390 nm) suggests that the transition dipole moments along the longest axis of the **SFPT** molecules are aligned horizontally in the as-deposited amorphous film. However, the optical anisotropy of the **SFPT** film almost disappeared in the *b*-phase after thermal treatment at an elevated temperature above T_g but below T_c (Fig. 4b). From these VASE results, anisotropies in molecular orientation can be quantified by the orientation order parameter (S), given by

$$S = \frac{k_e - k_o}{k_e + 2k_o}$$

where S = −0.5 when all of the molecules are horizontally oriented, S = 0 when they are randomly oriented, and S = 1 when they are all oriented perpendicularly to the substrate. VASE analysis revealed that S of the **SFPT** films was −0.34 for the *a*-phase and −0.09 for the *b*-phase. With increasing annealing temperature above T_c, a recrystallization transition occurred in the **SFPT** film, forming a continuous crystalline terrace-like texture with pronounced surface roughness (Fig. 4-7).

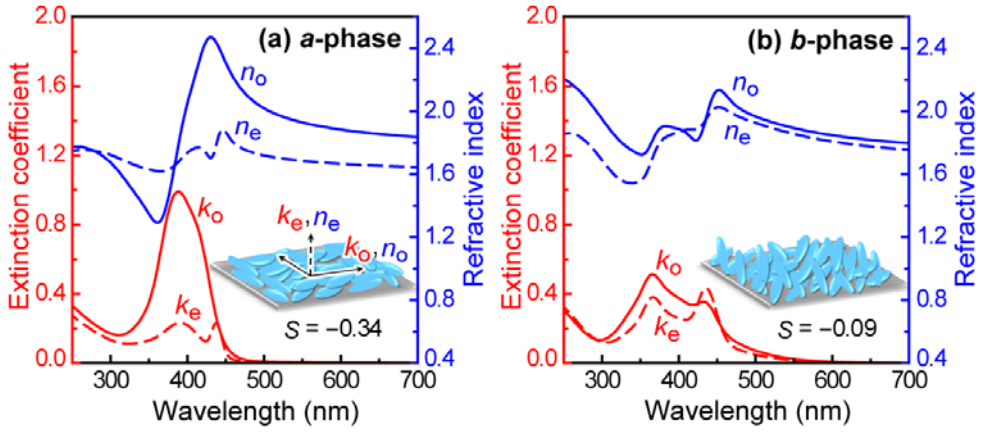

Figure 4-6. Ordinary (solid lines) and extraordinary (dashed lines) extinction coefficients (k_o and k_e) and refractive indices (n_o and n_e) of **SFPT** films determined by VASE: (a) *a*-phase (as-deposited) and (b) *b*-phase formed after thermal treatment at 140 °C for 10 min.

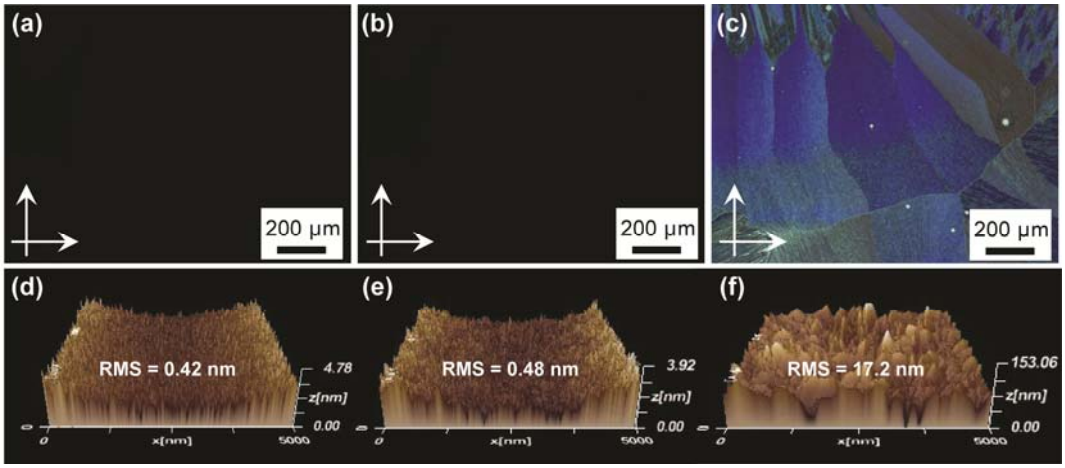

Figure 4-7. POM (top panels) and AFM images (bottom panels) of **SFPT** films on Si/SiO_2 substrates: (a,d) at room temperature (*a*-phase) and after thermal treatment at (b,e) 140 °C (*b*-phase) and (c,f) 180 °C for 10 min (*c*-phase).

Meanwhile, for **BFPT**, both the untreated and annealed films showed small optical anisotropy ($S = -0.13$ and -0.03, respectively; Fig. 4-8). This suggests that the **BFPT** molecules with bulky biphenyl substituents have a weak tendency to adopt horizontal orientation within thin films, presumably because of large steric hindrance between neighboring molecules.

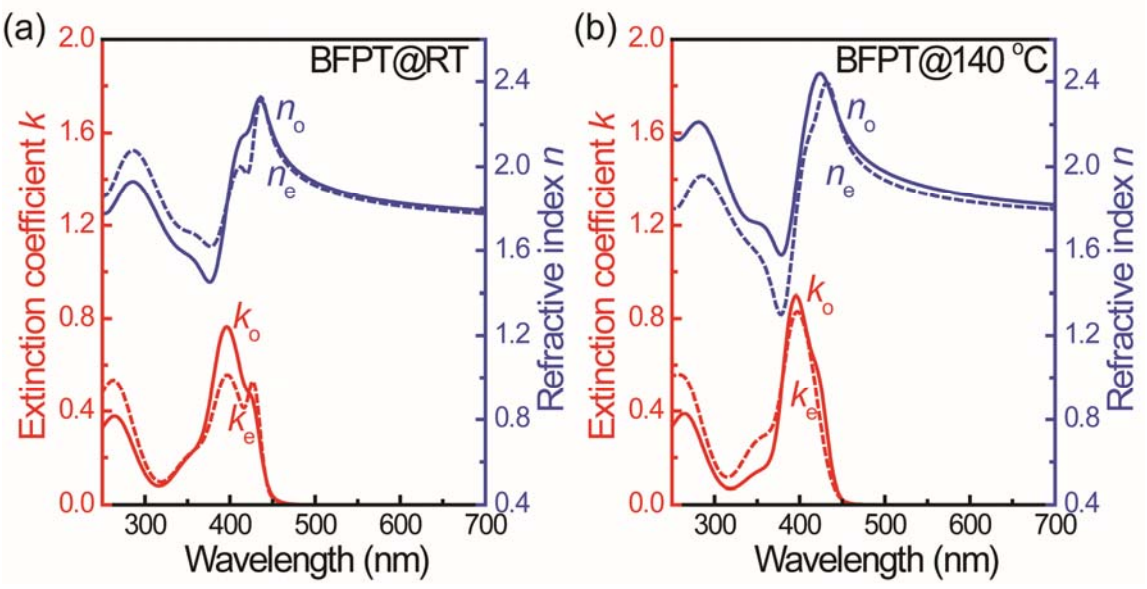

Figure 4-8. Ordinary (solid lines) and extraordinary (dashed lines) extinction coefficients (k_o and k_e) and refractive indices (n_o and n_e) determined by VASE measurements for an as-deposited **BFPT** film at (a) RT and (b) after thermal treatment at 140 °C for 10 min.

4-6. Amplified spontaneous emission (ASE) properties

SFPT and **BFPT** emit bright sky-blue photoluminescence (PL) and show relatively high PL quantum yields of 46±2% and 43±2%, respectively, in neat films. It has been envisaged that the observed preferable molecular orientation will be suitable for self-waveguiding amplification of light emission from these thin films. Waveguided propagation of emission is generally thought to be a prerequisite for lasing.[12] To this end, the **SFPT** and **BFPT** films were optically pumped using a pulsed N_2 gas laser (λ_{ex} = 337 nm, pulse width = 500 ps, and repetition rate = 20 Hz), and the light emitted from the edge of the films was collected. Figure 4-9a shows the absorption and PL spectra of an as-deposited **SFPT** film (*a*-phase). The PL spectrum exhibited broad vibronic peaks with shoulders at 442, 475, and 510 nm, which are assigned to the (0–0, 0–1, 0–2) transition bands, respectively. As plotted in Figure 4-9b, upon increasing the pumping energy, the emission intensity centered at 484 nm increased nonlinearly, accompanied by narrowing of the emission spectra, whose full width at half-maximum (FWHM) abruptly decreased to 4 nm. This spectral narrowing phenomenon is characterized as amplified spontaneous emission (ASE) caused by stimulated emission. The ASE with the highest gain occurred at the emission of the (0–1) transition, and was slightly red-shifted with respect to the PL peak because of self-absorption.

The ASE threshold (E_{th}) for the **SFPT** film (*a*-phase) was determined to be 0.7±0.1 μJ cm^{-2},[13] which is extremely low and comparable to values reported for 4,4'-bis[(*N*-carbazole)styryl]biphenyl (BSB-Cz, E_{th} = 0.6 μJ cm^{-2})[14a] and 2,7-bis[4-(*N*-carbazole)phenylvinyl]-9,9'-spirobifluorene (spiro-SBCz, E_{th} = 0.43 μJ cm^{-2})[14b] in neat films. By comparison, for the annealed **SFPT** film (*b*-phase) with random molecular orientation, a higher energy density (E_{th} = 1.1±0.1 μJ cm^{-2}) was required to induce ASE (Fig. 4-10). Therefore, the ASE property with a low threshold can be associated with preferential horizontal molecular orientation in thin films.[15] Indeed, the *a*-phase of the **SFPT** film has a larger in-plane refractive index than the *b*-phase at the ASE wavelength (484 nm), which would facilitate emission confinement in the waveguide mode.

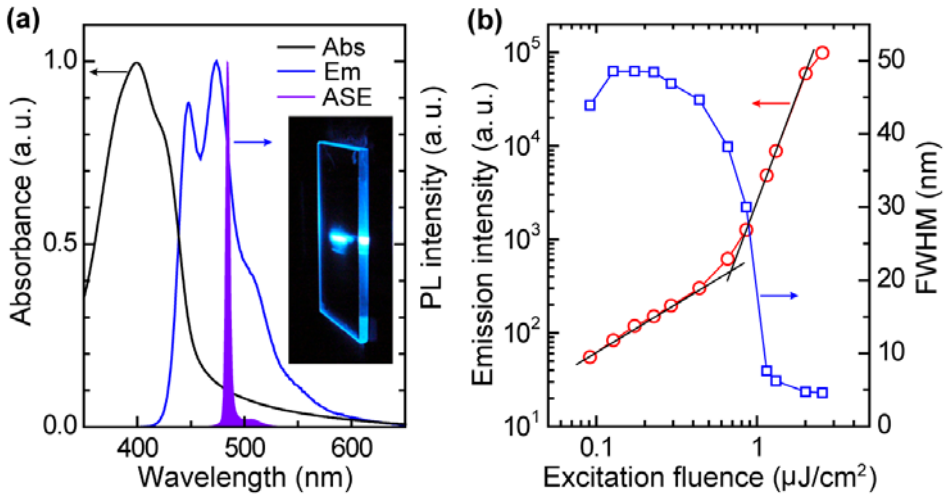

Figure 4-9. (a) Absorption, PL emission, and ASE spectra of a 100-nm-thick SFPT film in the a-phase. Inset: photograph of sky-blue ASE from the film edge taken under laser pulse. (b) Emission intensity and full width at half-maximum (FWHM) of PL as a function of excitation fluence.

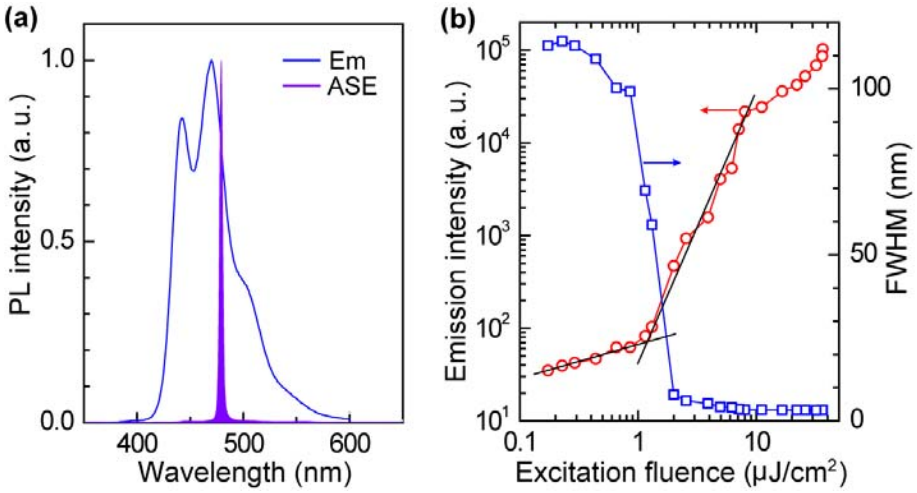

Figure 4-10. (a) PL emission and ASE spectra of a 100-nm-thick **SFPT** film in the *b*-phase after thermal annealing at 140 °C for 10 min. (b) Emission intensity and full width at half-maximum (FWHM) of PL as a function of excitation fluence.

4-7. Organic field-effect transistor properties

Representative output and transfer characteristics for OFETs employing as-deposited **SFPT** films (*a*-phase), films annealed at 140 ºC (*b*-phase) and 180 ºC (*c*-phase) are plotted in Figure 5. All of the devices are well-behaved p-type transistors under ambient conditions. For the transfer characteristics, the field-effect mobilities (μ) of the devices were extracted in the saturation regime ($V_D = -100$) using the following equation: $I_D = (W/2L)\mu C_i(V_G-V_{th})^2$, where I_D is the source-drain current, W and L are the channel width and length, respectively, C_i is the capacitance per unit area of the SiO_2 gate dielectric (11 nF/cm^2), V_G is the gate voltage, and V_{th} is the threshold voltage. The field-effect mobilities calculated from the transfer curves were 1.2 $\times$ 10^{-3} cm^2 V^{-1} s^{-1} for RT and 1.1 $\times$ 10^{-4} cm^2 V^{-1} s^{-1} for 140 ºC annealing (Fig. 4-11b and 4-11d). Decrease of the mobilities may result from the generation of deep trap levels and change of the interfacial contact between the organic layer surface and the dielectric layer caused by difference molecular orientation ($S_{RT} = -0.34$ and $S_{140\,°C} = -0.09$).[16] In addition, the field-effect mobility observed in the **SFPT**-based OFETs at RT is one of the highest values among those for vacuum-deposited amorphous OFETs.[17] Among the SFPT devices, the **SFPT**-based device annealed at 180 ºC shows the best electrical performance due to the stacking arrangement of the layer-by-layer crystalline structure with more effective intermolecular interaction, which can be seen from the XRD data (Fig. 4-3). The hole mobility of the **SFPT**-based OFETs at 180 ºC reaches 3.7 $\times$ 10^{-3} cm^2 V^{-1} s^{-1} with a high on/off current ratio on 10^5 and the output characteristics show low contact resistance and good saturation behavior (Figs. 4-11e and 4-11f). In addition, note that the V_{th} drastically decreases in the order of *b*-phase $\approx$ *a*-phase ›› *c*-phase. This is because the HOMO level after crystallization is well-matched with the work function of the gold electrodes (Fig. 4-12). Compared with the OFETs based on **SFPT** films, the OFETs based on **BFPT** films exhibit much lower mobilites ($\mu_{FET} = 2.1 \times 10^{-4}$ cm^2 V^{-1} s^{-1}, Fig. 4-13). Although **BFPT** molecules have π-conjugated chromophore backbones nearly identical to those of **SFPT** molecules, their loose horizontal orientation ($S = -0.13$) results in a decrease of the hole mobilities by an order of magnitude compared to OFETs utilizing the horizontal orientation of **SFPT**.

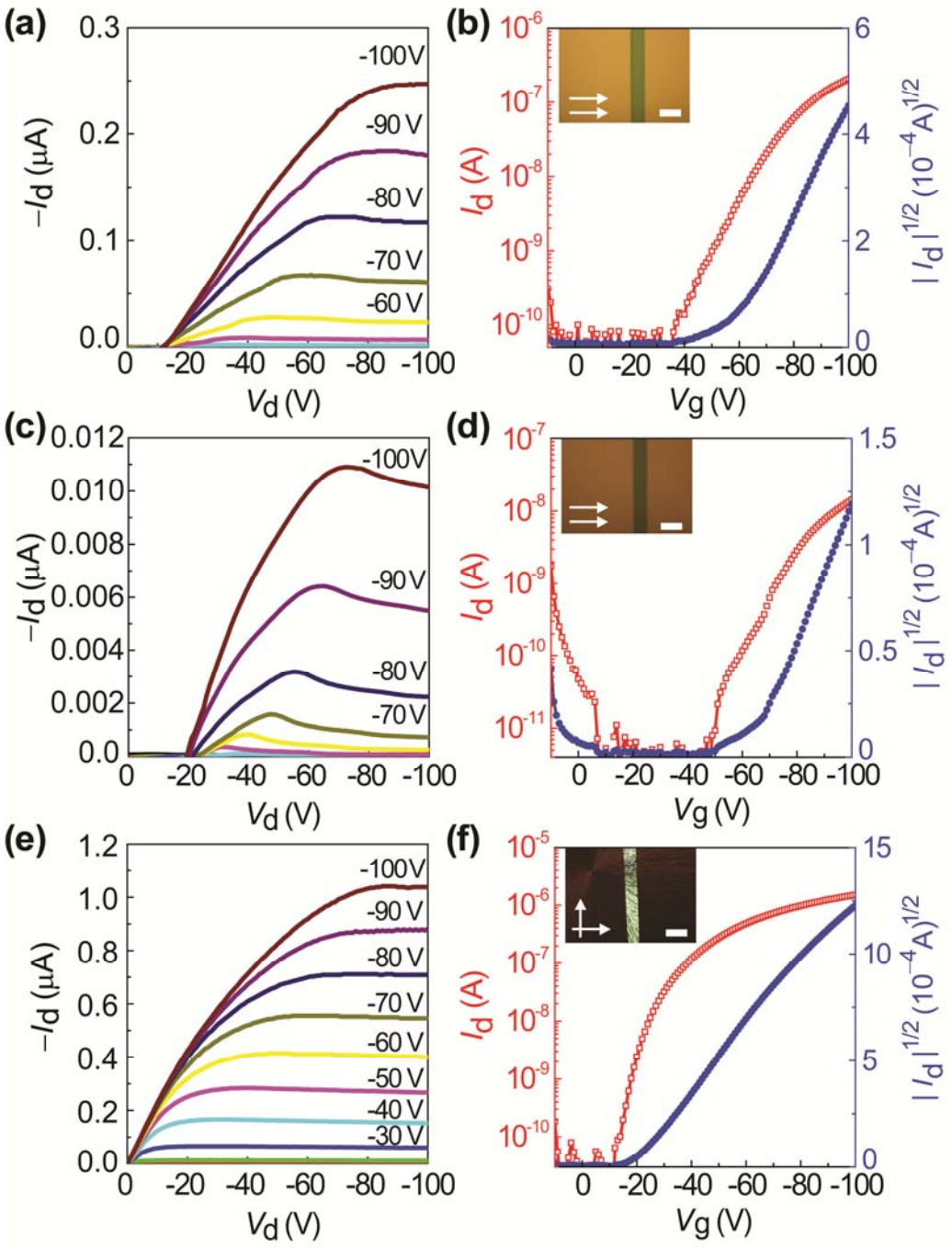

Figure 4-11. Output (left panels) and transfer characteristics (right panels) of OFETs based on **SFPT** films in (a,b) *a*-phase, (c,d) *b*-phase, and (e,f) *c*-phase. The insets show the optical microscopic images of the devices (scale bar = 100 μm).

Table 4-1. Summary of OFET properties of **SFPT**

polymorph	orientation	μ_{FET} (cm^2/Vs)	V_{th}[a] (V)	I_{on}/I_{off} [b]
a-phase	horizontal	1.2×10^{-3}	−57	10^4
b-phase	random	1.1×10^{-4}	−64	10^4
c-phase	crystalline	3.7×10^{-3}	−20	10^5

[a] Threshold voltage was determined by extrapolating the $|I_D|^{1/2}$ vs V_G plot to $I_D = 0$

[b] On/off ratio was determined from the I_D at $V_G = 0$ V (I_{off}) and $V_G = -100$ V (I_{on}).

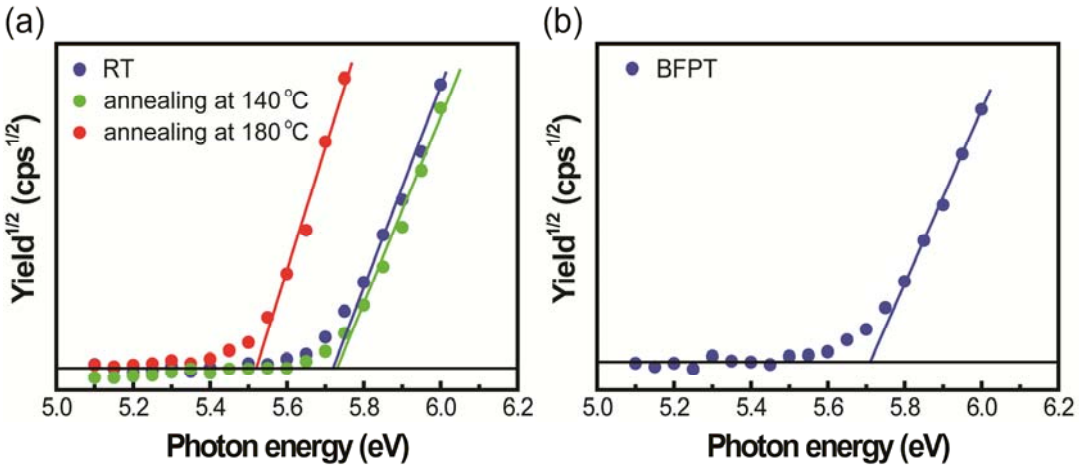

Figure 4-12. Photoelectron yield spectra of (a) **SFPT** and (b) **BFPT**.

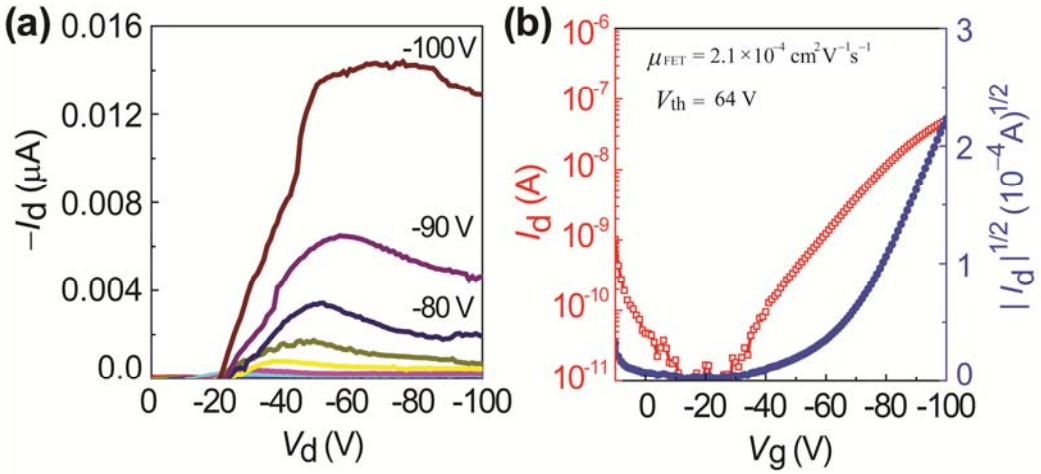

Figure 4-13. Output (a) and transfer characteristics (b) of OFETs based on **BFPT**.

4-8. Conclusion

In summary, the 9,9-diarylfluorene-based organic semiconductors **SFPT** and **BFPT** were fabricated, and their polymorphic solid-state structures were studied. **SFPT** molecules tend to align horizontally along the substrate surface even in the amorphous state. It has been demonstrated that such anisotropic molecular orientation and rich polymorphic behavior have significant impacts on charge transport and ASE properties. Significant differences in p-type OFETs and SCLC properties between **SFPT** and **BFPT** are observed in VASE results, in which the molecular orientation is strongly affected by the core of the central fluorene unit. Spirobifluorene-based **SFPT** has an unique polymorphic behavior by using thermal annealing, including both efficient horizontal orientation and an improved crystallization that lead to excellent carrier transport abilities. It is thus imperative to control polymorphism in organic semiconductors. Further experiments to achieve efficient carrier injection in these materials and realize electrically driven organic lasers are under way.

4-9. Reference

[1] W. C. McCrone, *Physics and Chemistry of the Organic Solid State*, eds. D. Fox, M. M. Labes, A. Weissberger, Wiley, New York, **1965**, vol. 2, pp. 725–767.

[2] T. L. Threlfall, *Analyst*, **1995**, 120, 2435.

[3] (*a*) A. Troisi, G. Orlandi, *J. Phys. Chem. B*, **2005**, 109, 1849; (*b*) I. P. M. Bouchoms, W. A. Schoonveld, J. Vrijmoeth, T. M. Klapwijk, *Appl. Phys. Lett.*, **1999**, 74, 3302.

[4] (*a*) T. Siegrist, C. Kloc, R. A. Laudise, H. E. Katz, R. C. Haddon, *Adv. Mater.*, **1998**, 10, 379; (*b*) G. Horowitz, B. Bachet, A. Yassar, P. Lang, F. Demanze, J. L. Fave and F. Garnier, *Chem. Mater.*, **1995**, 7, 1337.

[5] (*a*) H. Jiang, X. Yang, Z. Cui, Y. Liu, H. Li, W. Hu, Y. Liu, D. Zhu, *Appl. Phys. Lett.*, **2007**, 91, 123505; (*b*) R. Pfattner, M. Mas-Torrent, I. Bilotti, A. Brillante, S. Milita, F. Liscio, F. Biscarini, T. Marszalek, J. Ulanski, A. Nosal, M. Gazicki-Lipman, M. Leufgen, G. Schmidt, L. W. Molenkamp, V. Laukhin, J. Veciana, C. Rovira, *Adv. Mater.*, **2010**, 22, 4198.

[6] (*a*) M. Brinkmann, G. Gadret, M. Muccini, C. Taliani, N. Masciocchi, A. Sironi, *J. Am. Chem. Soc.*, 2000, **122**, 5147; (*b*) M. Cölle, R. E. Dinnebier, W. Brütting, *Chem. Commun.*, **2002**, 2908.

[7] (*a*) C.-C. Wu, Y.-T. Lin, K.-T. Wong, R.-T. Chen, Y.-Y. Chien, *Adv. Mater.*, **2004**, 16, 61; (*b*) K.-T. Wong, Y.-Y. Chien, R.-T. Chen, C.-F. Wang, Y.-T. Lin, H.-H. Chiang, P.-Y. Hsieh, C.-C. Wu, C. H. Chou, Y. O. Su, G.-H. Lee, S.-M. Peng, *J. Am. Chem. Soc.*, **2002**, 124, 11576.

[8] M. C. Burla, R. Caliandro, M. Camalli, B. Carrozzini, G. L. Cascarano, L. De Caro, C. Giacovazzo, G. Polidori, D. Siliqi, R. Spagna, *J. Appl. Cryst.*, **2007**, 40, 609.

[9] G. M. Sheldrick, *Programs for Crystal Structure Analyses (Release 97-2)*, University of Göttingen, Germany, **1997**.

[10] (*a*) M. A. Lampert, P. Mark, *Current Injection in Solids*, Academic Press, New York, **1970**; (*b*) T. Matsushima, G.-H. Jin, H. Murata, *J. Appl. Phys.*, **2008**, 104, 054501; (*c*) J. Y. Kim, T. Yasuda, Y. S. Yang, C. Adachi, *Adv. Mater.*, **2013**, 25, 2666.

[11] (*a*) H. Fujiwara, *Spectroscopic Ellipsometry: Principles and Applications*, John Wiley & Sons, West Sussex, **2007**; (*b*) H.-W. Lin, C.-L. Lin, H.-H. Chang, Y.-T. Lin, C.-C. Wu, Y.-

M. Chen, R.-T. Chen, Y.-Y. Chien, K.-T. Wong, *J. Appl. Phys*., **2004**, 95, 881; (*c*) D. Yokoyama, *J. Mater. Chem.*, **2011**, 21, 19187.

[12] I. D. W. Samuel, G. A. Turnbull, *Chem. Rev.*, **2007**, 107, 1272.

[13] **SFPT** showed a much lower ASE threshold of 0.08 μJ cm^{-2} (160 W cm^{-2}), when doped into a 4,4'-bis(9-carbazole)-2,2'-biphenyl (CBP) host at a concentration of 5 wt%.

[14] (*a*) D. Yokoyama, H. Nakanotani, Y. Setoguchi, M. Moriwake, D. Ohnishi, M. Yahiro, C. Adachi, *Jpn. J. Appl. Phys.*, **2007**, 46, L826; (*b*) H. Nakanotani, S. Akiyama, D. Ohnishi, M. Moriwake, M. Yahiro, T. Yoshihara, S. Tobita, C. Adachi, *Adv. Funct. Mater.*, **2007**, 17, 2328.

[15] (*a*) H.-W. Lin, C.-L. Lin, C.-C. Wu, T.-C. Chao, K.-T. Wong, *Org. Electron.*, **2007**, 8, 189; (*b*) T. Komino, H. Nomura, M. Yahiro, K. Endo, C. Adachi, *J. Phys. Chem. C*, **2011**, 115, 19890.

[16] T. Komino, H. Nomura, M. Yahiro, C. Adachi, *Chem. Phys. Lett.*, **2013**, 563, 70.

[17] Z. Zhao, Z. Li, J. W. Y. Lam, J.-L. Maldonado, G. Ramos-Ortiz, Y. Liu, W. Yuanm, J. Xu, Q. Miao, B. Z. Tang, *Chem. Commun.*, **2011**, 47, 6924.

Chapter 5

Summary

In this thesis, the molecular orientation in vacuum-deposited organic amorphous films and their effect on optical and electrical characteristics of organic devices have been investigated.

In Chapter 2, novel starburst-type amorphous materials: N^1,N^1,N^4,N^4-tetra(biphenyl-4-yl)benzene-1,4-diamine (B-DDP); N^1,N^1,N^4,N^4-tetrakis(4-(thiophen-2-yl)phenyl)benzene-1,4-diamine (T-DDP); and N^1,N^1,N^4,N^4-tetrakis(4-(benzo[*b*]thiophen-2-yl)phenyl)benzene-1,4-diamine (BT-DDP) are synthesized and applied as hole injection layers (HIL) in organic light-emitting diodes (OLEDs). OLEDs containing these materials as a HIL demonstrated a significant reduction in the required driving voltage. It has been found these molecules form a horizontally oriented amorphous thin film upon vacuum deposition. A close correlation between the reduction of driving voltage in OLEDs and the orientation parameter of the organic thin films was observed. The enhanced horizontal molecular orientation resulted in the lower driving voltage because of a decrease in the hole injection barrier at the anode/HIL interface.

Horizontal orientation can be utilized to enhance both light outcoupling efficiency and carrier transport properties in OLEDs. In Chapter 3, bifunctional star-burst amorphous molecular materials, *N,N,N′,N′*-tetraphenyl-*p*-phenylenediamine (PDA) or triphenylamine (TPA) core with triphenylethene (TPE) units, displaying both efficient solid-state luminescence and high hole transport properties have been developed. A high external electroluminescence quantum efficiencies up to 5.9% has been attained in OLEDs employing the developed amorphous materials. It has been revealed that the spontaneous horizontal orientation of these light-emitting molecules in their molecular-condensed states leads to a remarkable enhancement of the electroluminescence efficiencies and carrier transport properties.

In Chapter 4, two fluorene derivatives, 2,7-bis(5-phenylthiophen-2-yl)-9,9'-spirobifluorene (SFPT) and 2,7-bis(5-phenylthiophen-2-yl)-9,9-bis(1,1'-biphenyl-4-yl)-fluorene (BFPT) were compared, and reported on the influence of substituents on the molecular orientation. Furthermore, it has been demonstrated here that vacuum-deposited films of SFPT exhibit varying carrier transport abilities and amplified spontaneous emission (ASE) due to polymorphic behavior and control the morphological structure from an amorphous state to a crystalline state by using thermal annealing treatment.

Starting with the first detection of the amorphous molecular orientation of linear-shaped fluorene derivatives estimated by VASE, the molecular orientation of various kinds of organic

materials have been investigated systematically. An enhancement of optical and electrical properties of the horizontal orientation in organic amorphous films explored through this thesis are all based on new organic materials. This thesis will be helpful in designing new materials and understanding device physics and for further improving the performance of organic devices.

In future, the development of this study for further understanding and improvement of device performance will be conducted. The study can be divided into three main themes, that is, (1) control of molecular orientation, (2) effect on orientation at interfaces, and (3) application to devices.

First, the molecular orientation can be controlled by chemical and physical technique. The relation between the amorphous molecular orientation and crystallinity caused by change of substituent and/or thermal treatment should be completely understood. The dynamic changes in molecular interactions of organic molecules are induced by internal and external stimuli such as steric hindrance and heat that can affect the intermolecular interaction. The molecular orientation on the extended interface between organic layers allows the tuning of the optical and electrical properties of the organic devices. It is because the molecular migration, alignment, and electronic structure can be largely influenced by the molecular interaction.

Second, it is reasonable to believe that the horizontal molecular orientation affects not only the charge transport in the bulk of films but also the charge injection at an electrode/organic or organic/organic interface, because the orientation affects the overlap of the wave functions at the interface. However, the ellipsometry cannot directly detect the orientation at the interface, such as in a monolayer. To explain and clarify the effect at the interfaces, detailed analysis by other methods is needed.

Third, the molecular orientation is commonly one of the critical viewpoints in research on organic devices other than OLEDs, such as OSCs or OFETs. From the electrical viewpoint, the horizontal orientation is preferable in OLEDs and OPVs for charge transport in the direction of thickness, and the vertical orientation is preferable in OFETs for lateral charge transport. If it becomes possible to control the polymorphic behavior which has both amorphous and crystalline phase in organic films in microscale to nanoscale, the optical and electrical advantage can be utilized not only for OLEDs and OSCs but also organic laser and OFET.

By solving the above issues, the performance of organic devices will be further improved,

and the fundamentals of organic devices will be much more sophisticated from the viewpoint of both chemistry and physics.

List of Publications

Original papers

[1] Jun Yun Kim, Daisuke Yokoyama, and Chihaya Adachi, *J. Phys. Chem. C*, **2012**, 116, 8699−8706.

[2] Jun Yun Kim, Takuma Yasuda, Yu Seok Yang, and Chihaya Adachi, *Adv. Mater.,* **2013**, 25, 2666−2671.

[3] Jun Yun Kim, Takuma Yasuda, Yu Seok Yang, Naoki Matsumoto, and Chihaya Adachi, *Chem. Commun.*, **2013**, in press.

Joint papers

[1] Ryosuke Kondo, Takuma Yasuda, Yu Seok Yang, Jun Yun Kim, and Chihaya Adachi, *J. Mater. Chem.*, **2012**, 22, 16816−16840.

Symposium

[1] Jun Yun Kim, Takuma Yasuda, and Chihaya Adachi, *Korea-Japan Forum*, Gyeongju, Korea (September 15, 2011)

[2] Jun Yun Kim and Chihaya Adachi, *SPIE Optics + Photonics*, San Diego, USA (August 23, 2011)

[3] Jun Yun Kim, Takuma Yasuda, Takeshi Komino, and Chihaya Adachi, *International Conference on Electroluminescence & Organic Optoelectronics*, Fukuoka, Japan (September 4, 2012)

[4] Jun Yun Kim, Takuma Yasuda, Yu Seok Yang, and Chihaya Adachi, *Materials Research Society Spring*, San Francisco, USA (April 3, 2013)

Acknowledgements

First of all, the author would like to dedicate his deepest gratitude to Professor Chihaya Adachi at the University of Kyushu for simulative guidance and continuous encouragement throughout the present work. His supervision kindly led the author to fascinating field of organic electronics. His constant support, encouragement and timely working under his guidance. Also, he provided a lot of opportunity to collaborate with scientists and company of various research fields and present our results in many symposiums, through which the author gained invaluable experience in research life. The author feel honored to acknowledge his seminal role behind this thesis.

The author is grateful to thank Prof. Hiroyuki Furuta and Prof. Toshihiko Imato for helpful discussions and advice regarding this thesis.

The author is grateful to Associate Prof. Takuma Yasuda for encouraging, reviewing, criticizing, and helping with experiments and fruit discussions about almost all of the research presented in this thesis.

The author would like to deeply appreciate Prof. Daisuke Yokoyama at the University of Yamagata for meaningful discussion and improving this work.

The author would like to thank to Yasuda group members, namely Yang Yu seok, Sae Youn Lee, Woong Shin, In Seob Park, Takehiro Takahashi, Masaki Numata, Ryosuke Kondo, Issei Ohtani, Hiroyuki Mieno, Takuro Nishimoto, Keisuke Asahi, Yuta Fukutomi, and Yu Hidaka, who have been very helpful, collaborative, and friendly inside and outside the lab during these past few years.

The author express his gratitude to all his colleagues in Adachi laboratory. Especially, the author would like to thank Assistant Prof. Kenichi Goushi, Adjunct Assistant Prof. Takeshi Komino, Adjunct Assistant Prof. Masatsugu Taneda, Dr. William Potscavage, Jr, Dr. Masaya Hirade, Hiroko Nomura, Bo Li, Gabor Mehes, Jie Li, Munetomo Inoue, Kou Yoshida, Yuta Sagara, Ryosuke Nakamichi, Sun Bin Hwang, Norihiro Komori, Ji Young Lee, Takahiro Higuchi, Yuta Hirayama, and others, for being part of all of my joys and sorrows.

The author is deeply indebted to Prof. Jae Hong Kim for several discussions and advice as well as the great opportunity to study in Kyushu University, Japan.

Financial support from the Global Centers of Excellence (G-COE) Program, Organic Photonics and Electronics Research (OPERA), and Precursory Research for Embryonic Science and Technology (PRESTO) are greatly acknowledged for providing me this research fellowship.

Finally, I would like to give my deepest appreciation to my family members: my parents, my parents-in-law, my sister, my brother-in-law, my sister-in-law, and my relatives. Their emotional support, love, and encouragement have inspired me to complete this thesis.